Colloidal Robotics: Programming Structure and Function in Colloidal-Scale Material Through Emergence, Design and Logic

by

Mayank Agrawal

A dissertation submitted in partial fulfillment
of the requirements for the degree of
Doctor of Philosophy
(Chemical Engineering)
in The University of Michigan
2020

Doctoral Committee:

Professor Sharon C. Glotzer, Chair
Assistant Professor Jordan M. Horowitz
Professor Michael J. Solomon
Professor Robert M. Ziff

Mayank Agrawal

amayank@umich.edu

ORCID iD: 0000-0001-9563-9736

DEDICATION

This work is dedicated to my mother *Jyoti*, the lady who had the audacity to dream

possibilities for her kid and the bravery to persevere.

ACKNOWLEDGEMENTS

TABLE OF CONTENTS

LIST OF FIGURES

ABSTRACT

Advancements in self-assembly and top-down fabrication approaches have enabled tailoring of colloidal materials, macromolecules and polymers, and both organic and inorganic nanoparticles to build advanced functional materials. Miniature sized robots made using such materials can have huge impacts in biomedical applications such as minimally invasive surgery, tissue engineering, targeted therapy, diagnostics and single-cell manipulation. This dissertation addresses building such robotic systems that are programmable at the elemental level and are tunable at the macroscopic level. Using coarse-grained particle simulations, analytical modeling, and mechanical design, I have developed three systems to this end that correspond to programming approaches for swarm intelligence, morphological control and mechanical computing respectively. The first two systems use colloids possessing propulsion, a.k.a. active particles, that harness environmental energy into a propulsion force and can be developed using a wide variety of materials. The first system consists of particles that trigger propulsion only when in contact with other particles. An ensemble of such particles can be tuned externally to form and switch among crystals, gels and clusters as emergent behavior. Further, these systems possess enhanced transport dynamics, which is also tunable. In the second system, the active particles are connected end-to-end in a loop. When actuated, the loops fold into programmed shapes while the internal space is available to accommodate additional components such as sensors, controller, chemicals, and communication devices. The shape and motion information is encoded in the arrangement of ac-

tive particles along the loop. Besides relevance of these systems in understanding the fundamental physics of non-equilibrium systems, they can be used to develop smart materials that can sense, actuate, compute and communicate. Physical experiments using kilobots—centimeter sized robots—are performed to demonstrate the scale invariance and feasibility of the design. The third system is inspired from the development of materials that respond to external stimuli by expanding or contracting, thereby providing a transduction route that integrates sensing and actuation powered directly by the stimuli. Our work motivates building colloidal scale robots using these stimuli-responsive materials. For maximum control using global triggers, computation ability needs to be incorporated within such robots. The challenge is to design an architecture that is compact, material agnostic, stable under stochastic forces, and employs stimuli-responsive materials. The third system resolves these challenges through an architecture that computes combinatorial logic using mechanical gates. It uses linear actuation—-expansion and contraction—-as input-output signals with the additional benefits of logic circuitry being physically flexible.

CHAPTER I

Introduction

The conventional electromechanical components of a robot such as actuator, sensor, and processor are already being rapidly developed in the robotics community due to advancements in semiconductor, software and battery technologies. Recently, physicists and material scientists have started envisioning incorporating robotic behavior in materials owing to following three reasons:

1) *Need for smart materials:* Applications for autonomous robotic machines operating on submicron scales are foreseen in healthcare [1], defense[2], manufacturing[3] and energy[4]. For example, micron scale robots that can move inside the body, diagnose, deliver targeted drugs and provide surgical treatments if necessary; textile embedded with or composed of tiny particles that can change their structure for the given external stimuli such as heat and light to change the macro property of the fabric; robotic particles can be dispersed in the oceans to cleanup oil spills, then collected and stripped of their oil for reuse; military carrying bandages that have embedded colloidal machinery to autonomously clean up wounds of their shrapnel and apply medicine with minimal supervision. These applications pose inherent constraints like the type of material to be used, functional response at micron and

nano length scales, and ability to directly sense and exploit external stimuli. There-fore, physicists and material scientists have started thinking of ways to incorporate robotic functionality into materials circumventing usage of electromechanical com-ponents and pushing the boundaries of material properties using non-equilibrium physics.

2) *Development of actuating materials:* The two classes of materials heavily studied in relavance to programmable materials are active particles and stimuli-responsive polymers (SRPs). Active particles are colloids on the order of hundreds of nanometers to several microns that convert energy in their environment, such as light, chemical fuel, heat, sound, and electric and magnetic fields[5, 6, 7, 8, 9, 10] into a propulsion force[5, 6, 7, 11]. Active particles can be made from a variety of materials, including metals, polystyrene, silica, PMMA, PDMS, and hydrogels[5, 6, 7, 11] and in many different shapes, such as spheres[12], rods[6, 7] and gears[8]. Examples of active particles include molecular motors[13, 14], micro-organisms[6], self-propelling[12], self-rotating colloids[8] and particles propelled via symmetry-breaking[15, 16]. Propulsion speeds ranging from microns to tens of millimeters per second have been demonstrated[6]. Unlike active particles, SRPs expand and contract in response to external stimuli acting like artificial muscles[17, 18, 19]. The advantage is that SRPs act both as the sensor and the actuator for stimuli that them-selves act as the power source and the communication agent, thus integrating the electronic counterparts. There are plethora of different varieties and designs devel-oped for SRPs motivating their application[17, 18, 20, 19].

3) *Advancements in fabrication methods:* Developments in techniques in self-assembly[21, 22], DNA binding[23, 22], 3D printing[24, 19], and lithography[25, 26]
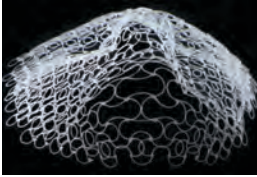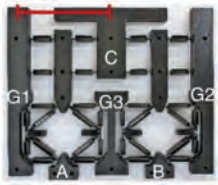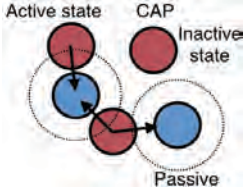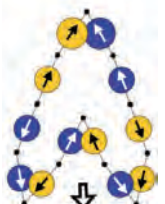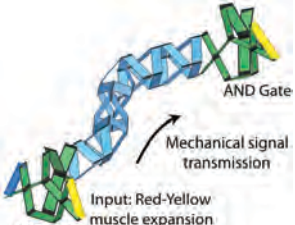
Programming approach	**Swarm intelligence**	**Morphological control**	**Mechanical computation**
Robotic behavior	Tunable mechanical and transport properties of the swarm	Morphable geometrical structure	Manipulation of end-effectors
Conventional macro-scale systems	Kilobot swarm	4D printed structure	NAND Gate
Biological system	Bird flock	Kinesin protein CGI	Neural activity
Colloidal scale systems developed in this work	Contact-triggered active particles	Chain loops of active particles	Mechanical logic architecture

Fig. 1.1: Programming approaches and corresponding systems. The three programming approaches (column-wise) are shown with illustrations of conventional macro-scale systems, biological systems, and the three systems (bottommost row) developed in this work. Image credits are: Kilobot swarm[29]; 4D printed structure[30]; NAND Gate[24]; Bird flock-Unsplash,James Wainscoat; Kinesin protein-John Lieber; Neural activity[31]

allow building complex structures at colloidal scale. Self-assembly techniques uses shape and sticky coatings on colloids to allow them to assemble thermodynamically[27]. DNA binding[22] uses complementary strands of DNA to bond selective particles allowing for programmable assembly. Non-contact 3D printing techniques[28] can print structures with micron scale resolution.

A robot, by definition, is a machine carrying out a series of tasks autonomously. For a robotic colloidal system, this implies that its behavior space is complex enough to switch between multiple structures and functions and that this switch can be con-

trolled by the environment or the user. The requirement of complexity and control call for colloidal systems that are programmable. Further, using active particles and SRPs to transduce these colloidal systems demand unconventional ways of achieving this programmability. This thesis provides three such unconventional ways, each corresponding to a conventional programming approach (illustrated in Fig. 1.1). These three approaches of programming information into materials that depend on the overall objective and context are: swarm intelligence, morphological control, and mechanical computation. Currently, the colloidal actuator materials–active particles and SRPs–are not as complex as biological cells or integrated circuits. Additional difficulty in controlling these systems arises due to the their small scale. The work in this thesis bridges these three programming approaches to colloidal actuator materials using the following three systems respectively,

System 1: Contact-triggered active particles (CAPs)

System 2: Chain loops of active particles

System 3: Mechanical logic architecture.

1.1 Swarm intelligence

A swarm is a collection of independent agents that are interacting with each other. Each agent holds a similar set of instructions through which it interacts with other agents. These local interactions lead to an emergent behavior. The study of such emergent behavior was motivated by natural swarms like flocks of birds and schools of fishes[32]. It is shown that these can be generated using simple interactions between the organisms. At the miniature scale, cells interacts among themselves using elaborate reaction pathways and chemical signaling to carry out bodily func-

4

tions and form tissues and organs. The information for these interaction mechanisms is stored in the genetic code carried by them. In robotics, robots carry and process the interaction protocol via integrated circuits. Rubenstein's *kilobots*[29, 33] are popular swarm bots that communicate through infrared and move using vibratory motors. Currently, the active colloids are not as complex as biological cells and do not possess microcontrollers. Hence, for now, the colloidal swarms may not perform complex functions as compared to cells but they can still make up practically useful materials. For these materials, two factors are to be considered:

a) Application context- Local interactions between colloids can be used to tune macroscale material properties as a result of their emergent behavior. For example, external stimuli can trigger a interaction policy between colloids that changes the material's mechanical and transport coefficients.

b) Colloidal properties- Colloids interact through their shapes, attraction or repulsion patches, propulsion force, bonding. Simple forms of chemical signaling between these colloids can also be incorporated[34]. While effects of these properties can been studied in isolation, a robotic system would be required where colloids change these properties depending on the neighboring colloids. In fact, an independent unit does not need to a single colloid, it can be a connected bunch of colloids referred to as a colloidal agent. Each agent will have a set of properties–shape, attraction, propulsion, bonds–that will define its state. Depending of the physico-chemical science of the colloids of these agents, agents with different states will interact differently forming their interaction policy. This will allow for a more complex forms of emergent behaviour than possible by using simple agents without the ability to change their state based of a local event–contact with an agent of a different

state. For such a system, conventional algorithms developed for swarm robotics like policy optimization of Markov decision processes can be directly applied[35].

System 1: Contact-triggered active particles (CAPs)

Whether the event-driven state change is useful in tuning macroscale material property is still not studied for synthetic colloidal systems. The contribution of the first project (chapter 2) is to prove this idea using a simple example, where a set of particles switch on their propulsion force only when and as long as in-contact with another set of particles. This phenomenon is inspired from few experimental systems[36, 37, 38, 39] and is referred as contact-triggered activity in this work. In this binary system, the set of particles that switch their propulsion based on the contact event are called CAPs. The global parameters of this system is system composition and strength of the propulsion force. By tuning only these two parameters, the material phase can be switched between crystals, gels, and cluster phase. These parameters also govern the traveling density waves in the system which can potentially vary material's transport coefficients. To put a perspective on applications of such a system, consider using different species of particles that behave as CAPs when incident by different frequencies of light. By switching off and on these frequencies, the fraction of CAPs in the system is varied. The intensity of these frequencies will determine the propulsion strength of the CAPs. Thereby controlling the macroscale material properties using external stimuli.

1.2 Morphological control

In context of robotics, morphological control typically occurs in a system of connected objects with each object having its own transduction property. Communi-

cation occurs directly between connected neighbors. Since the system as a whole forms a connected structure, the information of the function is stored in design of the structure. This presence of structure is absent in the swarm systems which allows morphological systems to encode relatively more information. Additionally, morphological systems make finite heterogeneous system unlike swarm systems that make emergent patterns. For instance, proteins, the workhorses of living organisms, are chains of amino acids, which have 20 different varieties. Different amino acids in a protein interact among themselves in a unique fashion due to their particular sequence, thereby, storing information about their function in their sequence. Li and coworkers[40] have achieved complex dynamic behavior by arranging simple actuators–that expand and contract with different frequencies–in a grid fashion. 4D printing is another rising field in this context, where structures are printed with different inks each with a different response to, for instance temperature. The pattern of different inks decide the system's morphological response to the stimuli temperature[30].

System 2: Chain loops of active particles

This work bring the idea of morphological control to colloidal scale and uses active particles, which are mostly studied as swarm systems, to build finite robotic machines. Our strategy is to connect motors end-to-end in a loop such that each motor's propulsion is tangential to the loop. Driven by the propulsion forces, this loop folds into a unique configuration. The programmability of its shape and motion is achieved by the sequencing of motors along the loop. Several applications of our system as reconfigurable material and metamaterial are present in chapter 3.

1.3   Mechanical computation

Although morphological control allows to encode function directly into system's morphology, processing of information is lacking in these systems demanding computation ability. To put this in perspective for the colloidal robots, we need a computation architecture that can process the input signals–external stimuli like heat, light and chemicals–and convey the processed information to robot's end-effectors. Since we need a material agnostic computing architecture for this purpose, mechanical computation can be used. Mechanical computing architectures use physical interactions between components to perform logic operations and store information. Several systems including using DNA[41], active colloids in microfluidics[42], and mechanical structures[24, 18] are being used for such computation. Though such systems are great proof-of-concepts for the purpose of computation, their relevance in robotics is unclear let alone colloidal robotics. Particularly, the architecture we are looking for has the following constraints:

a) Usage of SRPs in the architecture because a variety of SRPs are available that respond to a variety of stimuli by actuating. Hence, SRPs response can provide input signal for computation and actuation for robot's end-effectors.

b) Since SRPs actuate by expansion and contraction, the input-output signal should also be expansion-contraction.

c) For stability at colloidal scale, the architecture should be free from gears, colliding and sliding components.

System 3: Mechanical logic architecture

This system is a mechanical architecture (chapter 3) that satisfies the above con-

straints. It performs logic operations using only rigid bars and hinges, and muscle-like actuation as input and output. Additional advantage of this architecture is that it is physically flexible which increases the robustness of its computer. Direct applicability to robotics is demonstrated by folding a chain skeleton into Tetris blocks. Future applications of this design include:

1) Smart pills/liquid medicine: Nanoscale robotic carriers morph in response to chemical signatures of damaged tissues to release drugs and repair the site.

(2) Smart textile: This composes metamaterials where the macro scale properties are determined by the micro scale structure. Fabric embedding network of tiny mechanical actuators and computers that change the microstructure of the fabric to tune its optical, electronic, and mechanical properties in response to its environment.

3) Space rovers: Robots containing computers and actuators that can survive under extreme conditions and can directly be powered by its environment during planetary exploration.

4) Medical robots: Mechanical circuit mounted on tentacles in the order of 100 microns can be injected in human body. Magnetic field can navigate and orient the tentacle, whereas lasers can be used to activate specific input muscles. This in-turn will actuate the specific configuration of the tentacle to perform surgical operations.

5) Energy: Swarm of sub-micron scale robots can detect contaminants with certain chemical signatures and then morph in response to contain and remove those. Such mechanism can be used in chemical plants, preventive drugs, oil spills, and pipelines.

CHAPTER II

Tunable Emergent Structures and Traveling Waves in Mixtures of Passive and Contact-Triggered-Active Particles

This chapter is adopted from Ref [16], a publication in *Soft Matter* authored in 2017 by M. Agrawal, I.R. Bruss, and S.C. Glotzer.

2.1 Introduction

Active matter systems harvest energy from their surroundings in the form of chemical fuel or external fields, and in doing so are driven away from thermodynamic equilibrium [43, 44, 7]. One class of active matter in which the constituent particles that are *active* convert external energy into motion are widely studied to understand the fundamental physics of non-equilibrium systems [45], and to develop smart materials that can sense, actuate, compute and communicate [12, 5, 46]. Our work is motivated by several biological and synthetic systems within this class where the conversion of energy into motion is triggered by particle-particle contact. Examples include: neural crest cells propelling towards placode cells due to interdependent chemical signaling [36]; droplet pairs driven by the surface tension gradient between droplets [37]; pairs of physically or chemically dissimilar colloids under an external electric field exhibiting a propulsion force due to asymmetric electro-hydrodynamic
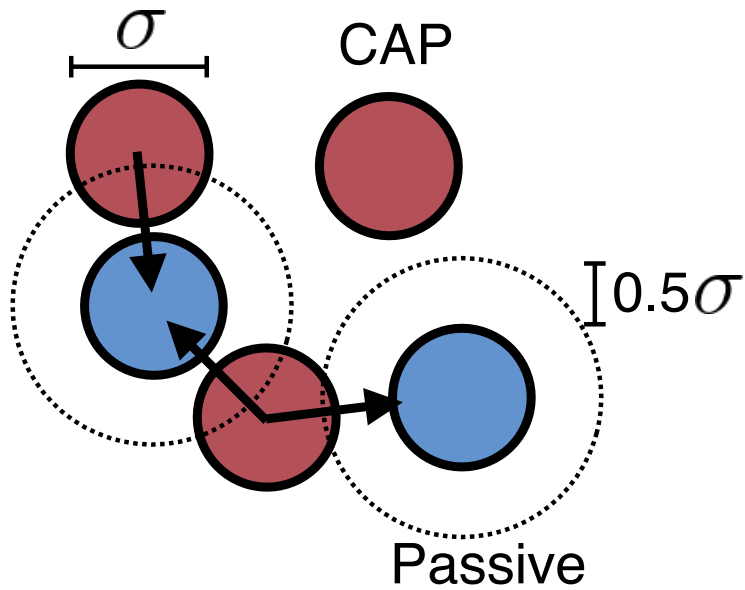
Fig. 2.1: Model of contact-triggered active particles (CAPs). CAPs are displayed in red and passive particles in blue. The solid arrows indicate the direction of the active force originating at the CAP's center. The dotted lines mark the region only within which a CAP is activated.

flows around them [38, 39]; and pairs of microcapsules exhibiting self-propulsion due to inter-capsule nanoparticle signaling [47]. These studies focus on understanding the mechanism of how contact-triggered activity arises, or on how particles move in a dilute limit. Here, we focus instead on the implications of contact-triggered activity in producing emergent behavior in a simple model 2D system.

We study binary mixtures of spherical passive particles (regular Brownian particles) and *contact-triggered active particles (CAPs)*, such that at any instance, a CAP experiences a propulsion force towards each passive particle with which it is in contact. (see Fig. 2.1). We show that these mixtures phase separate into dense and dilute phases of both types of particles, even for as few as 10% CAPs at a system packing fraction of 0.6. Within the dense phase, particles arrange into seven different patterns that balance the forces acting on them. The patterns are determined

by the fraction of CAPs in the dense phase and the strength of the active force. Furthermore, for mixtures with at most 30% CAPs, we observe spontaneous symmetry breaking of particle flux at the dense-dilute interface, such that one end of the dense phase recedes while the other propagates, producing traveling density fronts. We show that the strength of this symmetry breaking is proportional to the gradient of the ratio of CAPs to passive particles in the dilute phase.

2.2 Emergent behavior

We observe that mixtures of CAPs and passive particles phase separate into distinct dense and dilute phases (Fig. 2.2A). As expected for systems undergoing spinodal decomposition, the distribution of local densities changes from unimodal to bimodal (see Fig. 2.S1). This phase separation is a known property of other active matter systems such as ABPs [48, 49, 6] and ABP+passive particle mixtures [50]. However, we observe phase separation with only 10% CAPs, which is lower than the reported 15% ABPs for the ABP+passive particle mixtures [50]. To quantify the degree of phase separation (Fig. 2.2B,C), we calculate the fraction of particles in the largest cluster, c_{max}, since the largest cluster of a phase-separated system is the dense phase. Particles are clustered such that particle pairs with $\beta U_{WCA}(r) \geq 0.01$ belong to the same cluster, where r is the separation between the pair of particles. The equilibration time for the simulations is estimated by monitoring the time evolution of c_{max}. c_{max} increases monotonically with both F_{active} and ϕ, which is a similar behavior to that reported for ABPs by Redner *et al.* [48]. This result suggests that the phenomenon of phase separation is not restricted to systems where activity is a property of the particle, as in self-propelled or self-rotating[51, 52] particles. With
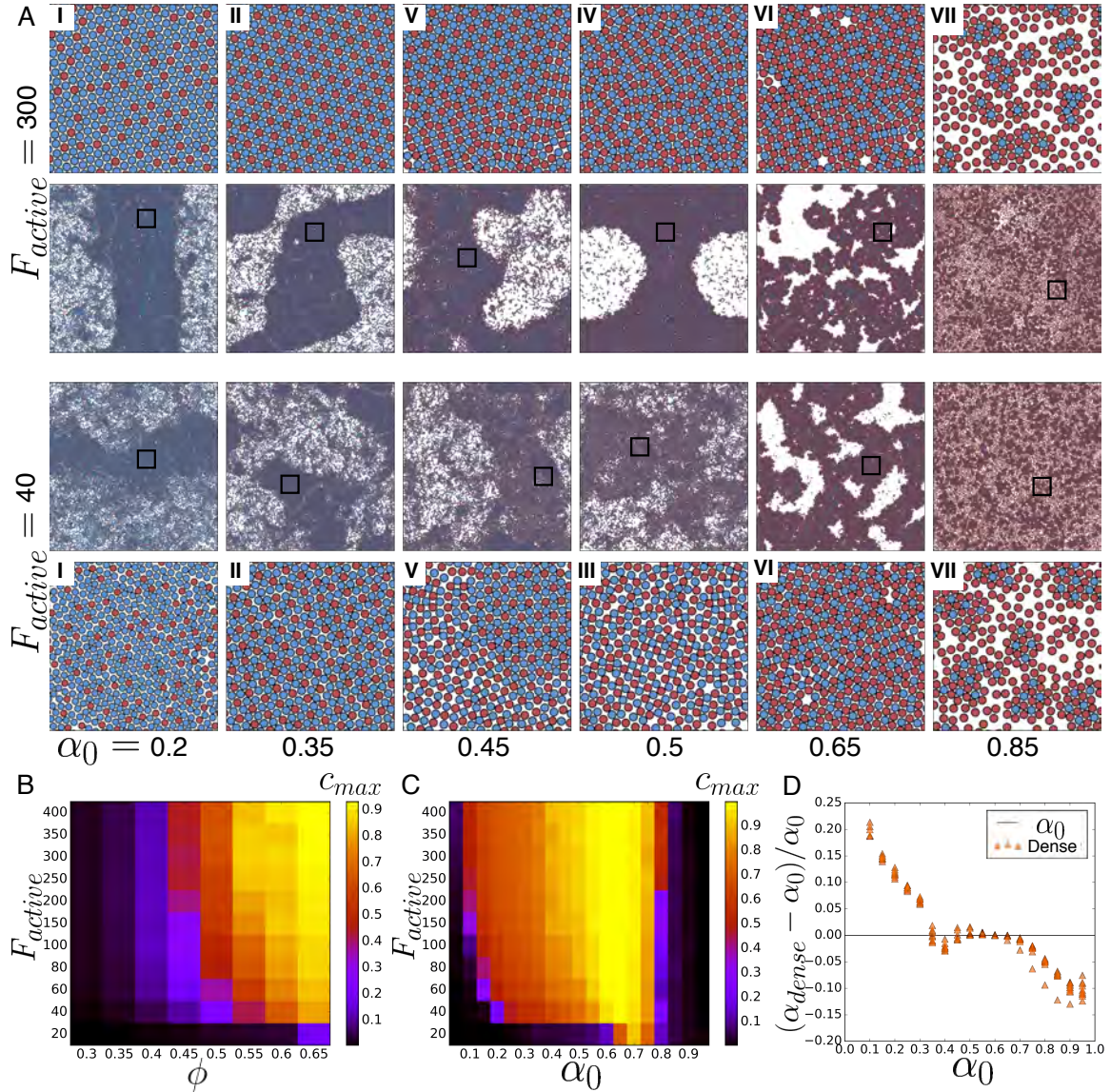
Fig. 2.2: Phase diagram of the CAPs system. (A) Steady-state snapshots of phase separated system at $\phi = 0.6$. First and fourth rows are zoomed-in snapshots of the squares marked in second and third rows respectively showing particle arrangement within the dense phase. The numerals represent different types of dense phase: I) 6-fold order, where CAPs are randomly distributed and they are each surrounded by six passive particles. II) Similar to phase I, but with CAPs and passive particles periodically distributed at 1:2 ratio. III) 4-fold order with CAPs and passive particles periodically distributed at 1:1 ratio. IV) 6-fold order with less order in the periodic distribution of CAPs and passive particles. V) Coexisting domains of either phase II and phase III or phase II and phase IV. VI) Kinetically arrested gel. VII) Clusters of CAPs and passive particles mixed together within clusters. (B,C) Heat map of fraction of particles in the largest cluster (c_{max}) for fixed (B) $\alpha_0 = 0.4$ (C) $\phi = 0.6$. (D) Fraction of CAPs in the dense phase, α_{dense}, relative to α_0 for all the state points (varying F_{active} and α_0) at $\phi = 0.6$ that phase separate and reach steady state. All quantities plotted are averaged over 200 frames in the time window $1000\tau < t < 5000\tau$.

respect to α_0, we find that c_{max} is zero at $\alpha_0 = 0$ and $\alpha_0 = 1$ with a maximum at $\alpha_0 \approx 0.65$. We attribute this behavior to the following. First, the number of activated CAPs depends on the probability of contact between CAPs and passive particles, which is zero at $\alpha_0 = 0$ and $\alpha_0 = 1$ and maximum at $\alpha_0 = 0.5$. Second, particle configurations where one or more passive particles are entirely surrounded by CAPs are mechanically stable because the active forces all push inward. Such configurations are more probable for higher α_0, resulting in the deviation of the c_{max} maximum to $\alpha_0 \approx 0.65$.

2.3   Structure of the dense phase

The structure of the dense phase is governed by the particles within the dense phase arranging themselves into a structure of mechanical equilibrium, i.e. where the net force on each particle is minimized. This arrangement is further influenced by F_{active} and the fraction of CAPs in the dense phase, α_{dense}. We show in Fig. 2.2D that α_{dense} is roughly proportional to α_0. Deviations at lower and higher α_0 occur because at lower values more than α_0 CAPs are required in the dense phase for it to stabilize, whereas at higher values fewer than α_0 CAPs are sufficient. Thus, the structural properties of the dense phase can be tuned using α_0 and F_{active}. We report and discuss seven types of dense phases shown in Fig. 2.2A. The corresponding phase diagram with approximate boundaries with respect to α_0 and F_{active} is presented in Fig. 2.3A (see 2.S2 for snapshots of all the statepoints).

To characterize the seven phases, we calculate the following quantities for the particles in the dense phase (shown in Fig. 2.3B-F: N_{CAP}, the average number of CAPs within 1.2σ of each CAP; $N_{passive}$, the average number of CAPs within 1.2σ

14
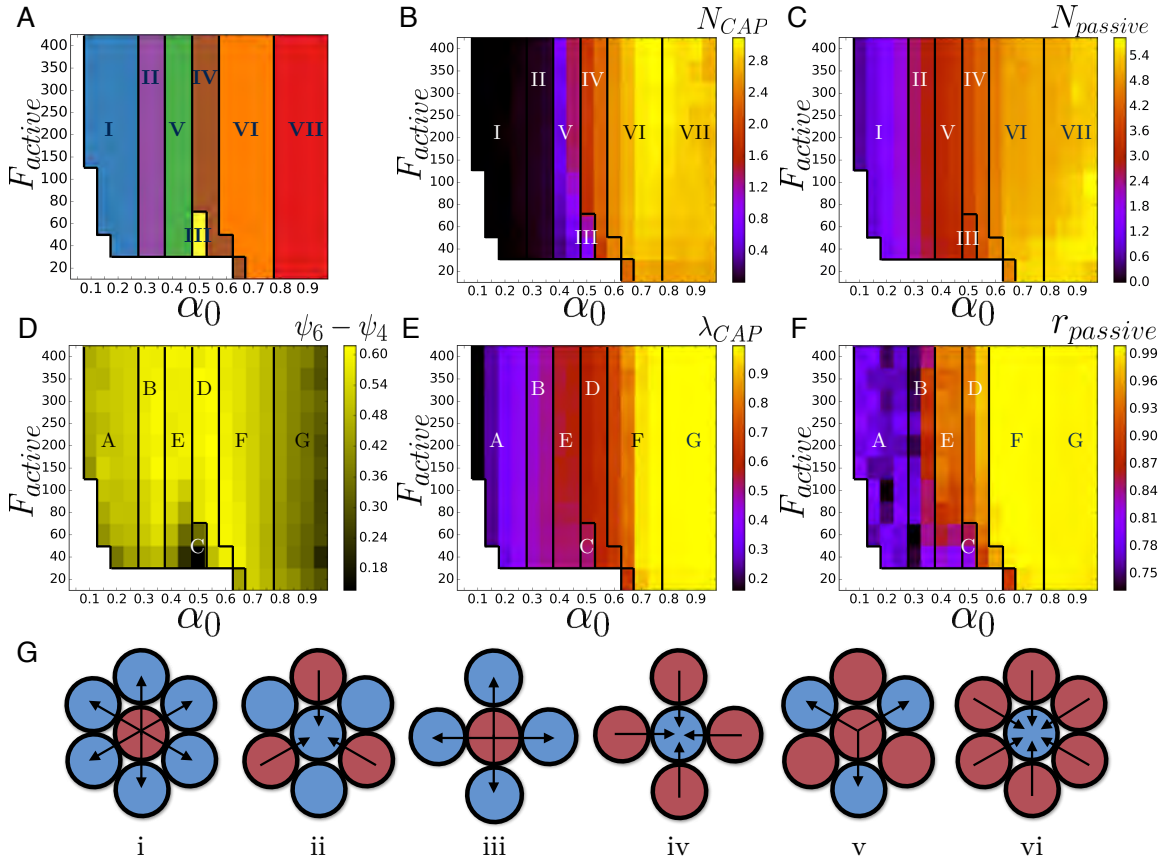
Fig. 2.3: Characterization of different phases. (A) Phase diagram at $\phi = 0.6$, labeling phases illustrated in Fig. 2.2A. The phase boundaries are estimated using quantities plotted in (B-E). (B) Heatmap of average number of CAPs, N_{CAP}, within 1.2σ of each CAP in the dense phase. (C) Heatmap of average number of CAPs, $N_{passive}$, within 1.2σ of each passive particle in the dense phase. (D) Heatmap of difference between hexatic and tetratic order parameter, $\psi_6 - \psi_4$, averaged over the particles in the dense phase at $\phi = 0.6$. (E) Heatmap of fraction of passive particles, $r_{passive}$ retained in the dense phase after 1000τ. (F) Heatmap of fraction of CAPs, λ_{CAP}, at the dense-dilute interface. All quantities plotted are averaged over 20 frames in the time window $1000\tau < t < 5000\tau$. (G) Schematic of force balancing particle configurations around a CAP/passive particle, where the arrows represent active force direction. Schematic *i* is observed in phase I, II, and V. Schematic *ii* is observed in phase II and V. Schematic *iii* and *iv* are observed in phase III and in phase V for low F_{active}. Schematic *v* and *vi* are observed in phase VI and VII.

of each passive particle; λ_{CAP}, the fraction of CAPs at the dense-dilute interface; $r_{passive}$, the fraction of passive particles that are retained in the dense phase after 1000τ; and $\psi_6 - \psi_4$, the difference between the hexatic and tetratic order parameters calculated for each particle and then their magnitude averaged over all the particles in the dense phase. $\psi_n = \langle |\boldsymbol{\psi_n}| \rangle_j$, where for each particle j, $\boldsymbol{\psi_n} = 1/n \sum_{k=1:n} e^{in\theta_{kj}}$, $n = \{4, 6\}$, and θ_{kj} is the bond angle between particles j and k [53]. These quantities are only measured for the state points where phase separation is observed, i.e. for $c_{max} \geq 0.2$ and also for $\alpha_0 > 0.8$, which is not captured by c_{max} since the dense phase is scattered as clusters. Each phase is described as follows:

Phase I and II:

For $\alpha_0 \lesssim 0.35$, particles in the dense phase are arranged such that all six neighbor particles of each CAP are passive particles (particle configuration in schematic *i* in Fig. 2.3G. This symmetry minimizes the net force. Although the configuration in schematic *i* is unstable to small perturbations, there exists an effective pressure pushing inwards on the boundary of the dense phase due to the active forces, thereby stabilizing the dense phase. Consequently, in these phases $N_{CAP} \approx 0$ (Fig. 2.3B). Phase II occurs in the range $0.3 \lesssim \alpha_0 \lesssim 0.35$, where CAPs and passive particles are distributed periodically in a 1:2 ratio featuring particle configuration in schematic *i* and *ii* (Fig. 2.3G). This ratio is because $\alpha_{dense} = 1/3$ is an ideal value for the system to form a crystal with a hexagonal unit cell containing 1:2 CAPs to passive particles while also balancing the active forces on the structure. In this case, symmetry in schematic *ii* is stable to small perturbations further stabilizing the structure. Phase II is characterized by $N_{CAP} \approx 0$ (Fig. 2.3B) and $N_{passive} \approx 3$ (Fig. 2.3C).

Phase III and IV:

For $\alpha_{dense} > 1/3$, there are fewer passive particles than required for forming phase II. Hence, at $\alpha_0 \approx 0.5$ and $F_{active} \lesssim 60$, the system forms phase III, where the dense phase is primarily composed of 4-fold crystal domains, with a ratio of 1:1 CAPs to passive particles in the unit cell featuring particle configurations in schematic *iii* and *iv* (Fig. 2.3G). This configuration has fewer passive particles around CAPs to balance the active forces as compared to the 6-fold ordered solid. This phase is characterized by low $\psi_6 - \psi_4$ at $\alpha_0 \approx 0.5$ (Fig. 2.3D). However, phase III is not perfectly uniform because pressure due to the active forces destabilizes the 4-fold order into a denser packing. Thus, $N_{CAP} \approx 0.8$ (Fig. 2.3B), which deviates from the expected value of $N_{CAP} = 0$ for the ideal phase III. For $F_{active} \gtrsim 80$, this effect results in the formation of phase IV, which is indicated by jumps in both $\psi_6 - \psi_4$ (Fig. 2.3D) and N_{CAP} (Fig. 2.3B) from $F_{active} = 60$ to $F_{active} = 80$.

Phase V:

In the range $0.4 \lesssim \alpha_0 \lesssim 0.45$, the number of passive particles are lower than required for phase II but higher than required for phase III or IV. Therefore, the particles arrange into coexisting domains of phase II and phase III for the lower values of F_{active} and phase II and phase IV for the higher values of F_{active}.

Phase VI and VII:

For $\alpha_0 \gtrsim 0.6$, the number of CAPs exceeds the number of passive particles in the dense phase featuring particle configurations in schematic *v* and *vi* (Fig. 2.3G). Therefore, the probability to surround one or more passive particles entirely by CAPs increases with α_0 (schematic *vi*). This effect is shown in Fig. 2.2A and indicated by a high value of $N_{passive}$ for $\alpha_0 \gtrsim 0.6$ (Fig. 2.3C). Such particle arrangements are

mechanically stable because all the active forces act inward, arresting the kinetics of the passive particles, and in turn limiting the kinetics of the system. This arrangement results in the formation of phases VI and VII, which are characterized by $r_{passive} \geq 0.98$ (Fig. 2.3E). In contrast to our systems, kinetically arrested gels are typically observed for systems with highly adhesive particles [54, 55]. For $\alpha_0 \gtrsim 0.85$, we observe phase VII, where the number of passive particles is too low to sustain a connected dense phase, and therefore the dense phase is broken into many clusters. This behavior is indicated by the drop in c_{max} (see Fig. 2.2C) for $\alpha_0 \gtrsim 0.8$. Additionally, the cluster surface is entirely composed of CAPs as evident by the measurement $\lambda_{CAP} \approx 1$ (Fig. 2.3F), with all the passive particles enclosed within the core. Because CAPs interact with each other via volume exclusion, the clusters rarely merge with each other.

2.4   System dynamics–Travelling density fronts

Apart from the diverse structural behavior, the system also exhibits rich dynamics. Here we focus on one particular dynamical behavior, observed only for $\alpha_0 < 0.35$. We observe steady state traveling fronts of density fluctuations with resemblance to the traveling fronts observed for ABPs+passive particles mixtures [50, 56] and reaction-diffusion systems [57]. To investigate this phenomenon we simulate the system in a rectangular box of $400\sigma \times 150\sigma$, allowing the dense phase to span the y-axis and travel along the x-axis.

Fig. 2.4A shows the time evolution of the traveling front, where the dense-dilute interface recedes at one end and propagates at the other end. This phenomenon results from the spontaneous symmetry breaking of particle flux at the dense-dilute
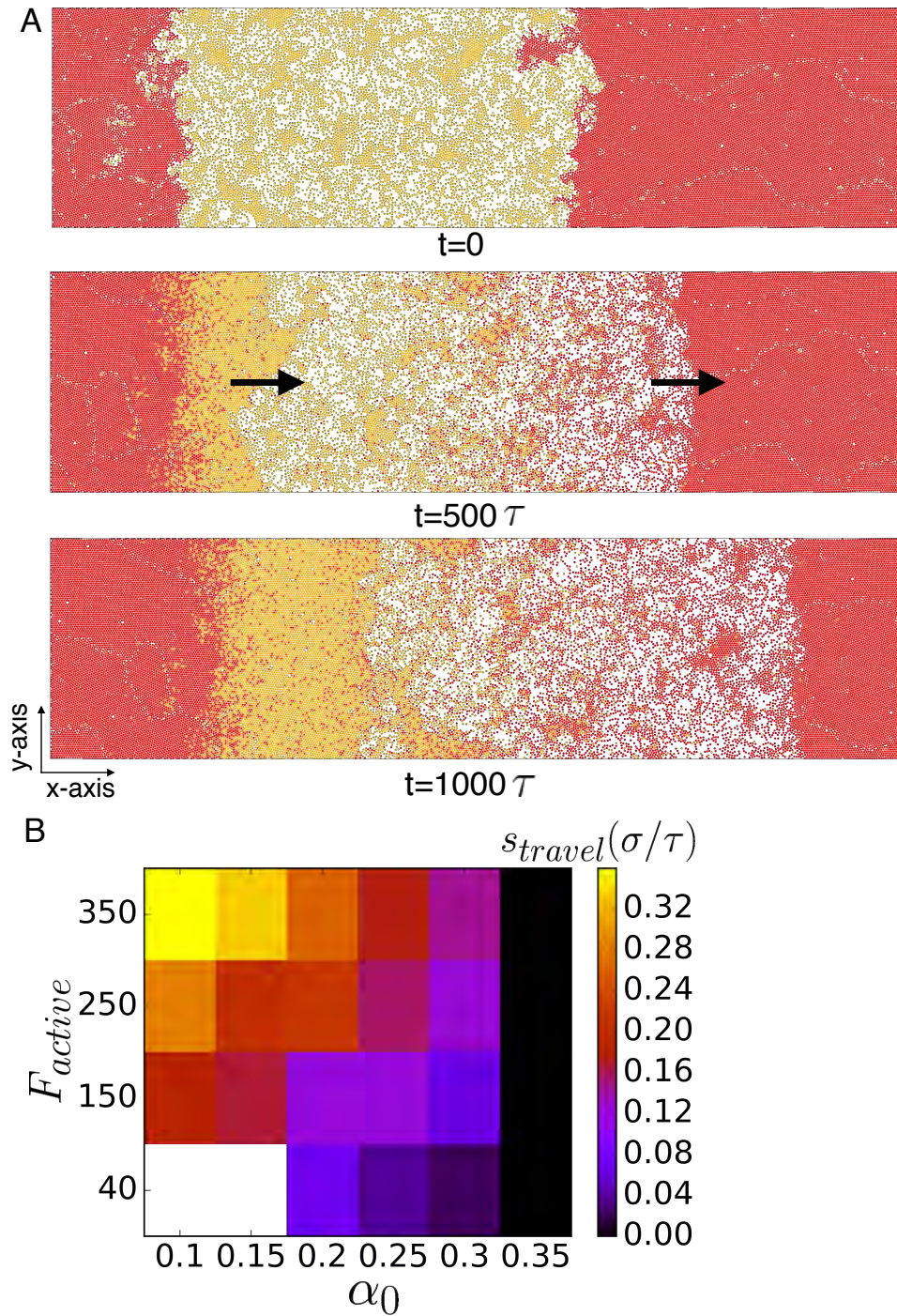
Fig. 2.4: Travelling density front. (A) Time evolution of the steady state system at $\alpha_0 = 0.25$, $F_{active} = 150$, and $\phi = 0.6$. All the particles in the dense phase at $t = 0$ are colored red (dark) and the others are colored yellow (light). The solid arrow indicates the direction of the travel. (B) Heatmap of the front travel speed, s_{travel}, at $\phi = 0.6$, calculated using distance traveled by the dense-dilute interface in 300τ. White region does not phase separate.

interface, such that there is a higher particle in-flux rate at the propagating front and a higher particle out-flux rate at the receding front. These rates determine the travel speed s_{travel} of the dense-dilute interface. To probe the dense-dilute interface, we average the particle density over the y-axis and define the interface to be at a density of $0.8\sigma^{-2}$. We find that s_{travel} increases with F_{active} (see Fig. 2.4B) because F_{active} governs the average particle speed in the dilute phase, the increase of which enhances particle flux at the dense-dilute interface. Alternatively, s_{travel} decreases with α_0 because α_0 governs the average particle density in the dilute phase (indicated in Fig. 2.2C), the increase of which lowers the particle flux at the interface. However, to explain why $s_{travel} = 0$ for $\alpha_0 \gtrsim 0.35$, where the dilute phase density is non-zero, we investigate the degree of symmetry breaking in the system.

By definition, CAPs move towards passive particles. Due to this effect, CAPs drift towards dense regions of passive particles and passive particles drift towards dilute regions of CAPs. As a result, the net particle flux is biased towards the region with the highest ratio of passive particles to CAPs. We measure this ratio in Fig. 2.5A as $\alpha^p(x)/\alpha(x)$, where $\alpha(x)$ is the fraction of CAPs as a function of the x-axis and $\alpha^p(x) = 1 - \alpha(x)$. We calculate $\alpha(x)$ by averaging it over the y-axis, shifting the origin to the dense-dilute interface for each time frame and then further averaging over many frames. We find that the ratio $\alpha^p(x)/\alpha(x)$ is higher near the propagating interface and lower near the receding interface, driving the particle flux in the bulk of the dilute phase towards the propagating front. Also, the gradient of $\alpha^p(x)/\alpha(x)$ declines with α_0, dropping to zero at $\alpha_0 = 0.35$. Thus, the degree of symmetry breaking is governed by the gradient of $\alpha^p(x)/\alpha(x)$ in the dilute phase.

Further insight into the mechanism (schematic shown in Fig. 2.5B) of the symme-
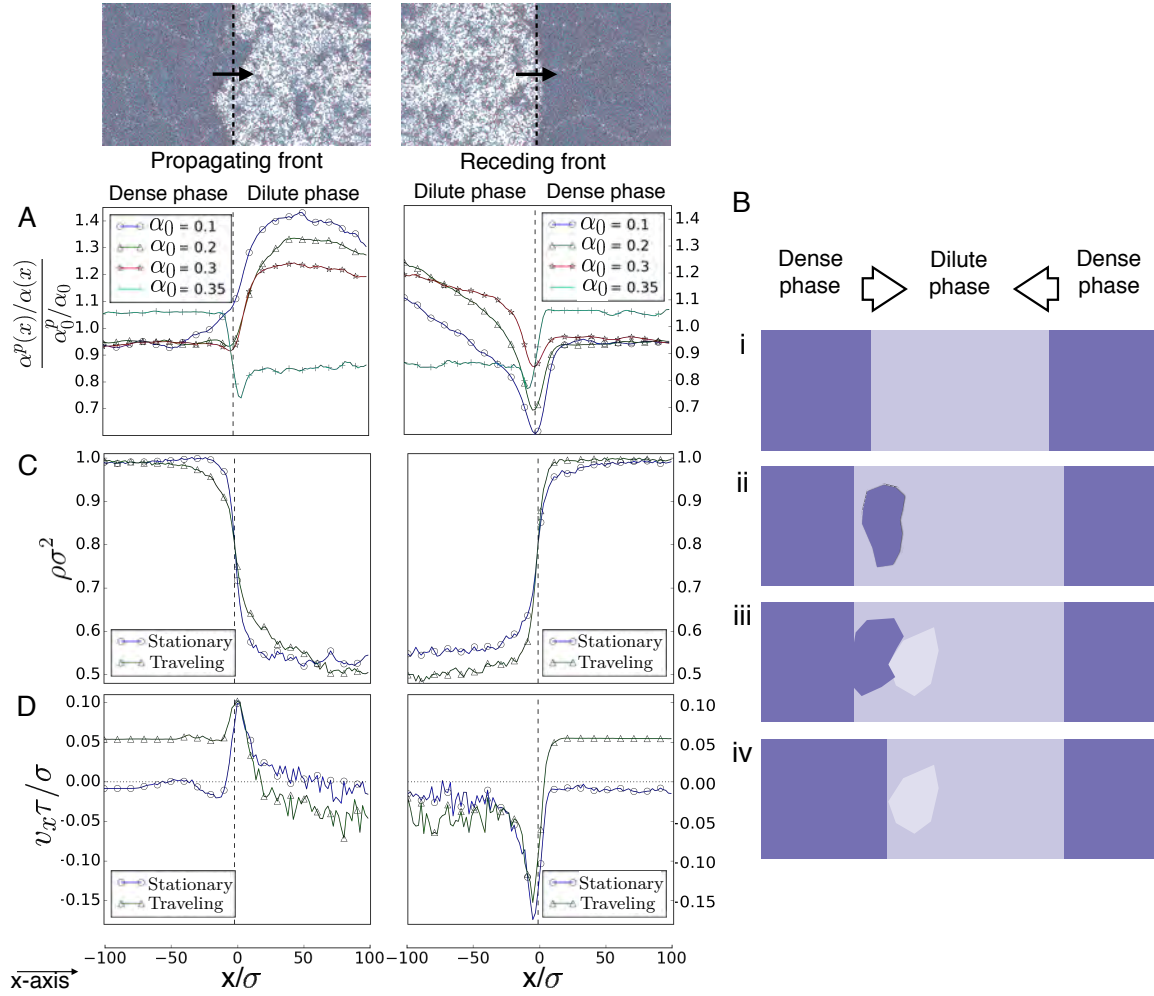
Fig. 2.5: Mechanism of travelling density front. (A) Ratio of passive particles to CAPs as a function of x-axis at $F_{active} = 150$, averaged over 150 frames and normalized by α_0^p/α_0, where $\alpha_0^p = 1 - \alpha_0$. (B) Simplified schematic showing the mechanism of symmetry breaking and travel of density wave. Hollow arrows represent direction of particle flux at the corresponding interfaces for each step. The intensity of color indicate particle density. (i) System after phase separation but before symmetry breaking. (ii) Cluster randomly forming near the left interface due to increased dilute phase pressure caused by the interface particles escaping into the dilute phase. (iii) Merging of the adjacent cluster with the left (closer) interface leaving a region of reduced local density behind. (iv) Complete merger of the cluster causing both the interfaces to shift towards right. This cycle breaks the left-right symmetry because it creates a positive feedback for more cluster formation near the left interface causing it to be the propagating front. (C) Particle density, ρ and (D) particle velocity, v_x, as a function of x-axis, evaluated at $\alpha_0 = 0.25$ and $F_{active} = 150$, averaged over 50 frames. The x-axis is shifted such that the dense-dilute interface is at the origin, which is shown as the dashed line. The solid arrow indicates the direction of travel.

21

try breaking leading to the emergence of a traveling wave is provided in Fig. 2.5A. At both the interfaces, $\alpha^p(x)/\alpha(x)$ is higher in the dilute phase, and therefore the particles on the dense side of the interface constantly escape to the dilute phase. This is because the passive particles at the interface have little to no CAPs pinning them in place. This in turn increases the CAP density on the dense side and passive particle density on the dilute side of the interface. Consequently, the CAPs on the dense side of the interface are also prone to escape into the dilute phase. However, in order to maintain the steady-state, there must be an equal deposition of particles into the dense phase. To investigate how this is achieved, in Fig. 2.5C,D we calculate particle density, ρ, and average particle velocity, v_x, respectively, which are evaluated similar to $\alpha(x)$. Both quantities are calculated during both the steady state with traveling fronts and the non-steady state, where the system is phase separated but the fronts are stationary. In the traveling state, ρ near the propagating front is higher than the receding front, in contrast to the stationary state. Additionally, in the traveling state, the particles in the dilute phase have v_x pointed towards the propagating front, while for the particles close to the propagating front, v_x points away from the propagating front. This behavior also aligns with the reasoning based on the $\alpha^p(x)/\alpha(x)$ gradient. These measurements reveal that in the dilute phase particles converge towards $v_x = 0$ and maximum $\alpha^p(x)/\alpha(x)$, which is near the propagating front. This increases the probability of forming clusters near the propagating front, also evident from higher ρ near the propagating front. The clusters adjacent to the propagating front merge with it, thus creating a region of reduced density causing the formation of more clusters near the propagating front. This in turn provides a positive feedback loop for the traveling front during steady state behavior. For

$\alpha_0 \gtrsim 0.35$, at both interfaces, $\alpha^p(x)/\alpha(x)$ is higher in the dense phase (Fig. 2.5A). This effect decreases the rate of escape of particles into the dilute phase, resulting in zero gradient of $\alpha^p(x)/\alpha(x)$ in the dilute phase, which consequently inhibits the formation of traveling waves.

2.5 Conclusion

We investigated the phase behavior of an active matter system in which the propulsion force is triggered when dissimilar particles are in contact. We showed that mixtures of CAPs and passive particles phase separate into dense and dilute phases. Because activity exhibited by CAPs is by definition always towards passive particles, the phase separation is targeted and efficient. In our system, phase separation was achieved with as few as 10% CAPs at 60% packing or at 45% packing with 40% CAPs. We also showed that by varying the magnitude of the active force and fraction of CAPs, the bulk structure of the dense phase can be tuned to acquire 6-fold or 4-fold crystal order, kinetically arrested gels and cluster phases. We reported propagating density fronts at low fractions of CAPs due to the spontaneous symmetry breaking of particle flux at the dense-dilute interface. The front speed is determined by the average particle speed, average particle density, and the gradient of the ratio of passive particles to CAPs in the dilute phase. These factors in turn are governed by the fraction of CAPs in the system and the strength of the active force. Future development of a theoretical model to describe these results would be interesting but non-trivial because of the binary nature of the system and the contact driven activation of the active force. In 2015, Stenhammar *et al.* presented a theoretical model for ABP+passive particle mixtures[50]. They made two

major observations that allowed them to extend to mixtures the equation of state developed for the system of sole ABPs. First, the propensity to phase separate is directly proportional to both the fraction of ABPs in the system and the strength of the active force. Second, when phase separated, the boundary of the dense phase is composed solely of ABPs. For CAPs+passive mixtures none of these statements are valid, so a different approach may be needed. For a fixed fraction of CAPs, we do observe that the propensity to phase separate is directly proportional to both the packing fraction and the strength of the active force. This particular behavior is similar to what is observed for the system of sole ABPs[48].

We showed that contact-triggered activity adds another dimension to the design toolkit of smart materials, which can be deployed to fabricate reconfigurable materials with tunable structure and dynamics. For example, a CAPs-passive mixture can reversibly transition between a kinetically arrested gel phase and a homogeneous fluid phase by switching on and off the system activity. Similarly, the transition between the 4-fold and 6-fold ordered solids via activity can be used to design cellular materials with embedded CAPs-passive mixtures, which will swell and contract due to the density difference between the two phases. Furthermore, the phenomenon of traveling density fronts can be utilized to create materials with tunable transport properties.

Besides the examples mentioned in the introduction, contact-triggered activity can also occur in electrochemical systems. For instance, we envision that binary mixtures of Pt and Au particles in an electrolyte will form a short-circuited cell when in contact to yield contact-triggered propulsion. This is because it is known that in bipolar electrochemical propulsion, Pt/Au Janus particles form a short-circuited

galvanic cell. The electric field points from Pt to Au, which drives the fluid from Pt to Au, thereby generating particle propulsion with the Pt end forward[58]. Our model can also be extended to study the examples of contact-triggered activity mentioned in the introduction. For droplets and cells, volume exclusion would be modeled using a soft potential, whereas for electro-hydrodynamic colloidal suspensions the active force would be modeled as a continuous and decreasing function of particle separation.

2.6 Materials and Methods

Our system is simulated in two dimensions with periodic boundary conditions using the simulation toolkit HOOMD-blue [59, 60, 61]. The dynamics of particle i is simulated using the Brownian equation of motion[62]

$$\dot{\boldsymbol{r_i}} = \beta D \sum_j \left(-\nabla U_{WCA}(r_{ij}) + f_{active} \frac{\boldsymbol{r_{ij}}}{r_{ij}} \right) + \sqrt{2D}\boldsymbol{\eta}(t), \tag{2.1}$$

where $\boldsymbol{r_i}$ is the position of particle i and index j loops over all other particles. The position of j from i is given by $\boldsymbol{r_{ij}} = \boldsymbol{r_j} - \boldsymbol{r_i}$, with magnitude r_{ij}. Volume exclusion interaction between particles is modeled via the Weeks-Chandler-Andersen potential, $U_{WCA}(r) = 4\epsilon \left[(\sigma/r)^{12} - (\sigma/r)^6 \right] + \epsilon$, for $r < 2^{1/6}\sigma$, and $U_{WCA}(r) = 0$ otherwise [63], where σ is the diameter of the particle and ϵ determines the strength of the repulsion. As a first approximation, the propulsion force is modeled by a constant magnitude external force f_{active} that is applied on a CAP only when it is within a cutoff separation of 1.5σ from a passive particle. The value 1.5σ is a design choice that triggers the active force on close particle-particle contact while still allowing some

tolerance of separation. In the absence of any passive particle within this cutoff distance, a CAP behaves just as a passive Brownian particle. To avoid unphysical effects, the inter-particle penetration depth due to the active force is required to be consistent for all simulations [64]. We achieve this by fixing the ratio $f_{active}\sigma/\epsilon = 20$. D is the translational diffusivity of particles, $\beta = 1/k_B T$ is the inverse thermal energy, and $\boldsymbol{\eta}(t)$ is unit-variance Gaussian white noise. Because the active force points from the center of a CAP towards the center of a neighboring passive particle, rotational noise in the active force direction arise from fluctuations of the particle positions due to translational diffusion.

We fix the simulation box size to be $150\sigma \times 150\sigma$, unless otherwise stated, and vary the system packing fraction $\phi = N\pi\sigma^2/4$ (N being the number of particles in the system), the fraction α_0 of CAPs in the system, and the non-dimensional active force $F_{active} = \beta f_{active}\sigma$, which is analogous to the Peclet number for active Brownian particles (ABPs) [64]. Time is measured in units of $\tau = \sigma^2/D$. All the simulations are initialized from a random distribution of non-overlapping particles and run for at least 1000τ to allow the system to equilibrate before measuring any quantity.

2.7 Supplementary Information
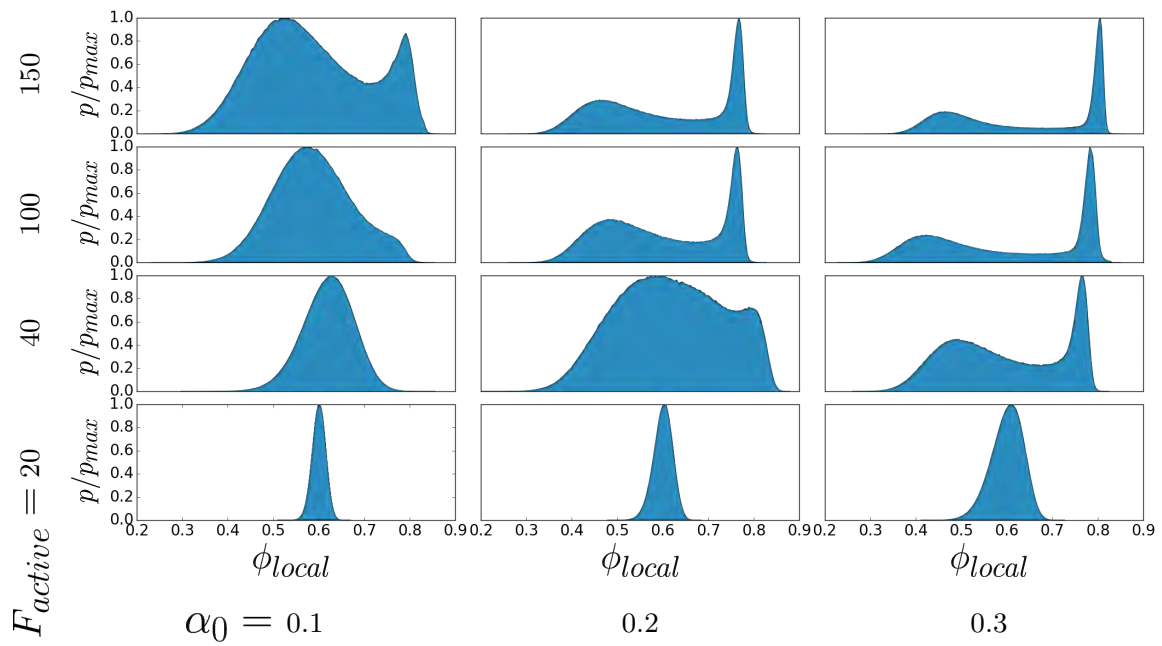
Fig. 2.S1: Local density distribution. The density distribution of the system at $\phi = 0.6$ for varying α_0 and F_{active}. For subplots, the x-axis varies the packing fraction ϕ and the y-axis plots its probability p. The distribution is calculated at the steady state and averaged over 250 frames.
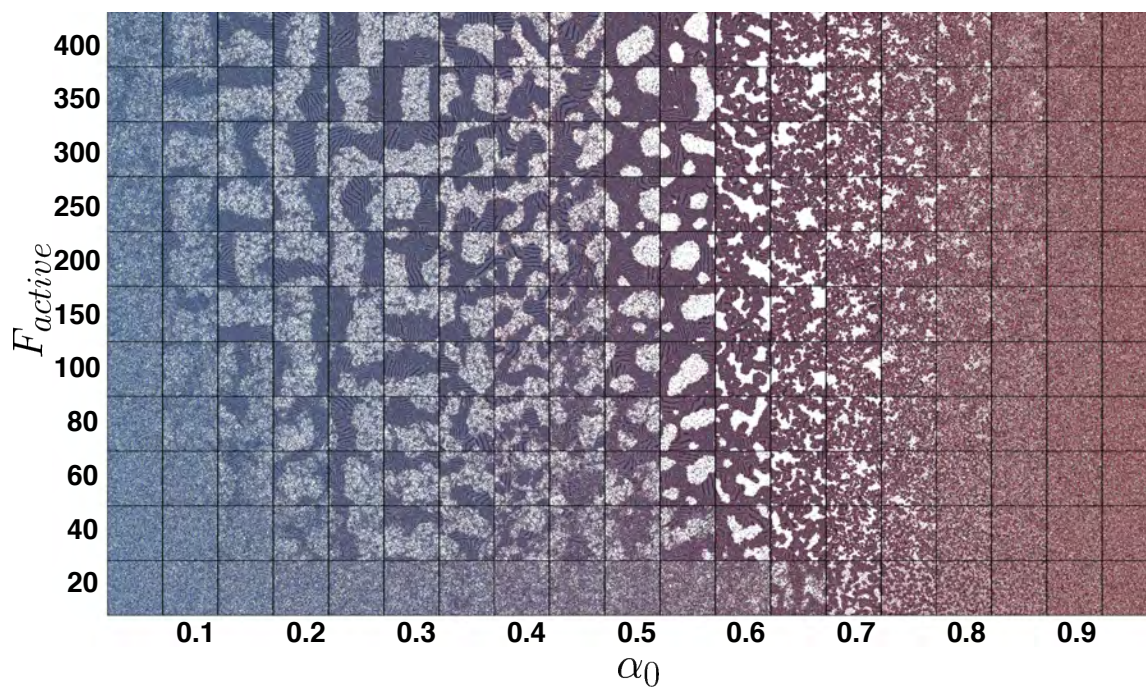
Fig. 2.S2: Snapshots of simulated statepoints. The phase diagram of the system at $\phi = 0.6$. The x-axis varies α_0 and y-axis varies F_{active}. Each grid point is a snapshot of the corresponding statepoint at steady state. The simulation method is described in the model and methods section of the paper.
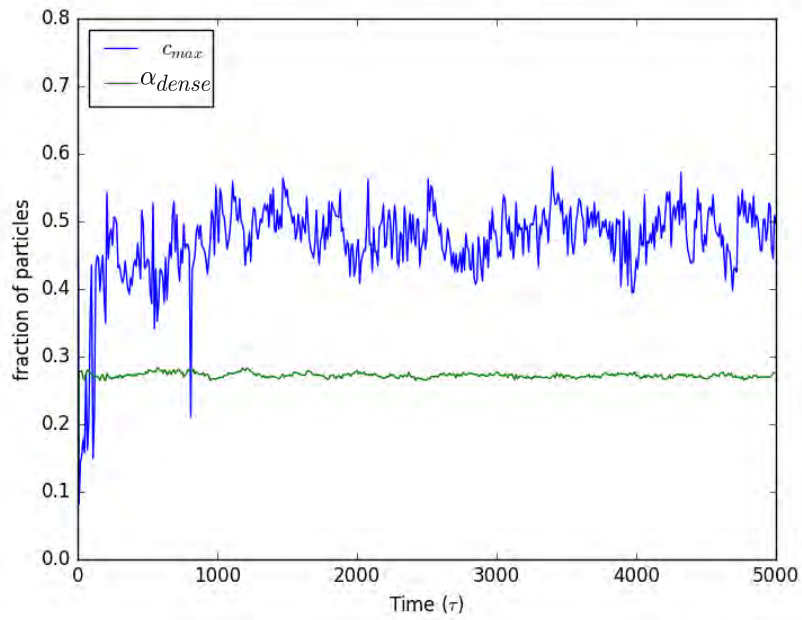
Fig. 2.S3: Time evolution of maximum cluster size. Time evolution of maximum cluster size, c_{max}, and fraction of CAPs, α_{dense}, in the dense phase at $\phi = 0.6$, $F_{active} = 40$, and $\alpha_0 = 0.25$.
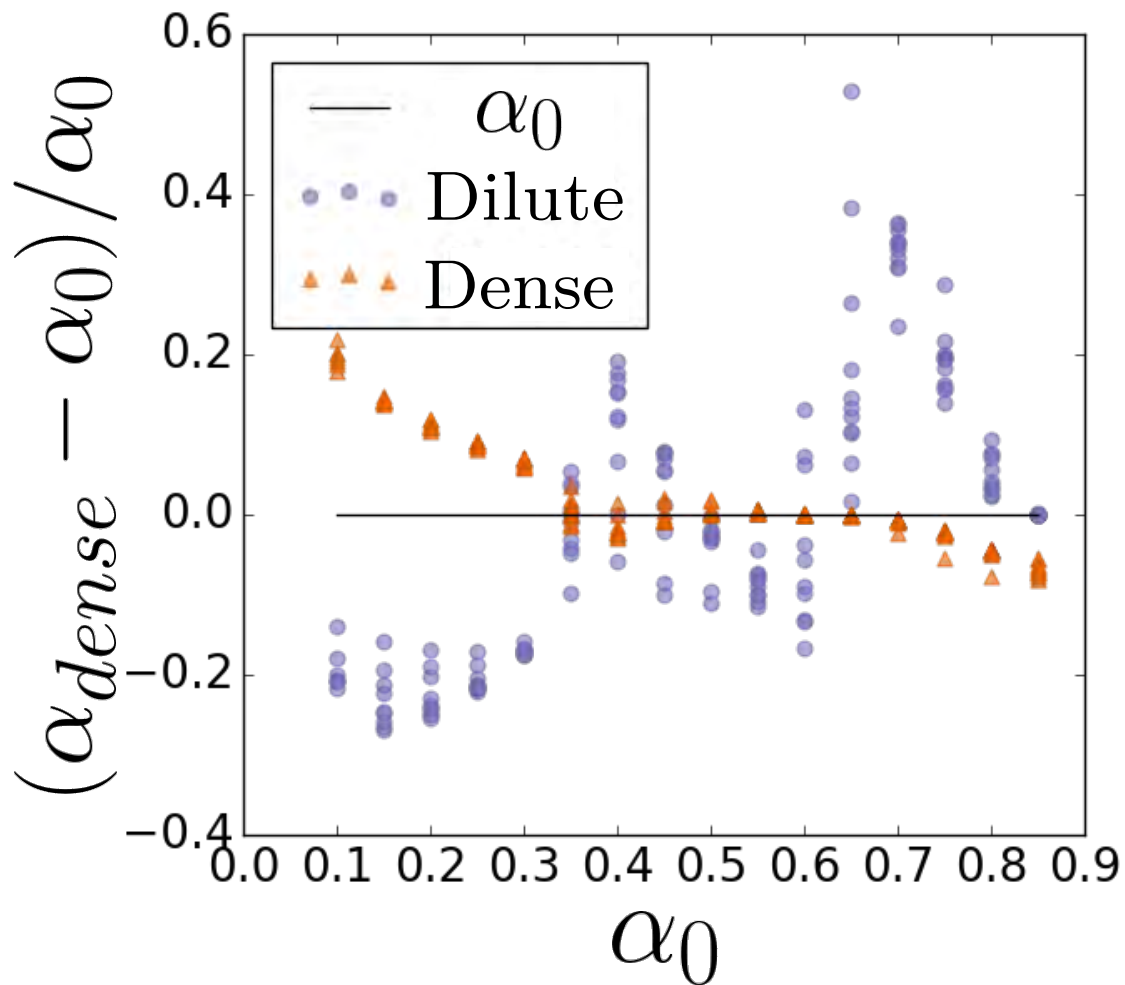
Fig. 2.S4: Fraction of CAPs in the dense and dilute phases. Fraction of CAPs in the dense and dilute phases, α_{dense} and α_{dilute}, relative to α_0 for all the state points (varying F_{active} and α_0) at $\phi = 0.6$ that phase separate and reach steady state.
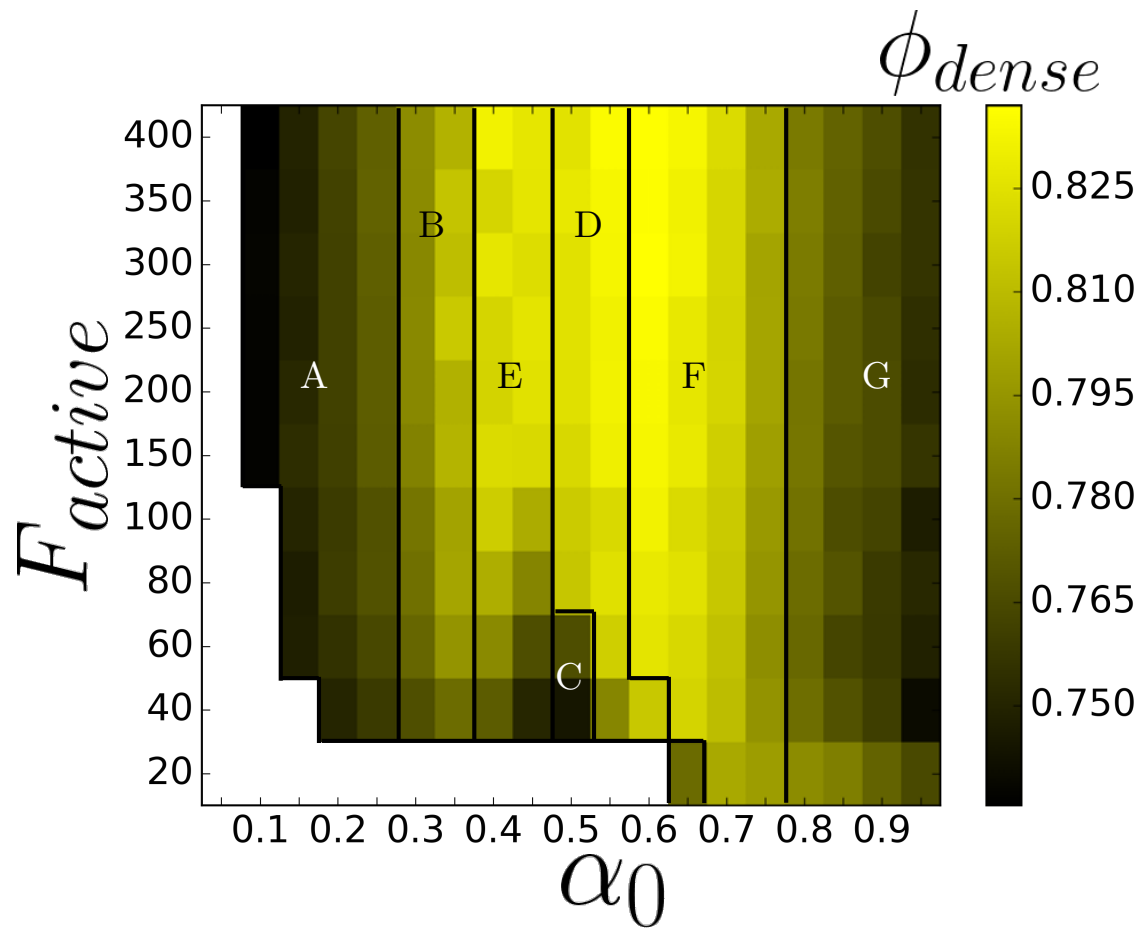
Fig. 2.S5: Heatmap of average local density. Heatmap of average local density, ϕ_{dense}, of the dense phase at $\phi = 0.6$, averaged over 20 frames.
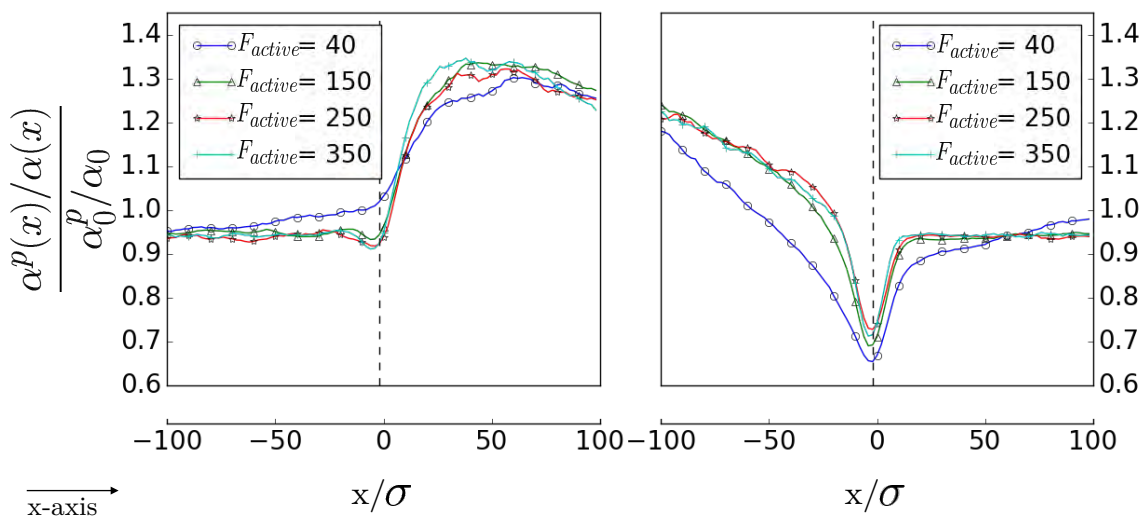
Fig. 2.S6: Ratio of passive particles to CAPs in the rectangular box. Ratio of passive particles to CAPs as a function of x-axis at $\alpha_0 = 0.2$, averaged over 150 frames corresponding to Fig. 2.5

CHAPTER III

Scale-Free, Programmable Design of Morphable Chain Loops of Kilobots and Colloidal Motors

This chapter is adopted from a publication authored by M. Agrawal, and S.C. Glotzer that is currently under review.

3.1 Introduction

Applications for autonomous robotic machines operating on submicron scales are foreseen in healthcare [1], defense[2], manufacturing[3] and programmable matter[4]. A key feature of such machines is their ability to morph into pre-programmed configurations in response to a stimulus. Two major attributes of robotics on any length scale are actuation and control. Conventional robotics uses electromechanical actuation components; this is challenging at small scales due to fabrication limitations, presence of stochastic forces, material constraints or the need for biocompatibility[11, 65, 3]. One approach to achieving actuation on microscopic scales is to exploit physicochemical principles of colloidal science. In this approach, colloidal motors on the order of hundreds of nanometers to several microns – also known as active particles – convert energy in their environment, such as light, chemical fuel, heat, sound, and electric and magnetic fields[5, 6, 7, 8, 9, 10] into a propulsion force[5, 6, 7, 11].

Diversity in material, shape, motion, and method of actuation, combined with the ability of colloidal particles to self-assemble, render active particles ideal motors for sub-micron applications.

Colloidal robotic machines aim to achieve some of the same behaviors as conventional swarm robotics, but in a very different way. In swarm robotics, the distributed control logic of robots (individual motors) is programmed via local interactions between the motors. An excellent example is provided by kilobots, fist-sized motors with their own control logic and memory on board. Rubenstein *et. al.* proposed an algorithm that runs on every kilobot, enabling them to self- organize as a swarm into prescribed shapes[29]. A critical feature of that approach is that each kilobot knows the target shape and, through communication with other kilobots, its location in the shape. Such knowledge would be challenging to imprint on a colloidal particle, and instead we seek a swarm-like approach with non-intelligent particle robots that lack individual identity.

Such an approach was recently introduced by Li *et. al.*[40] on the macroscale with robots that actuate by swelling and contracting, which pushes and pulls neighboring robots. The robots are programmed to actuate out of phase with each other; this phase offset programs the dynamical behavior of the system. These particle robots also require basic computation and clock synchronization. While colloidal particles can be made to swell or contract with an environmental change, such as a change in temperature or solvent pH, achieving programmable actuation with a prescribed phase for each individual, essentially identical particle is still not feasible. Instead, colloidal robotics must rely upon identical interparticle interactions among robots. This was demonstrated recently by Slavkov *et. al.*[66], who programmed

34
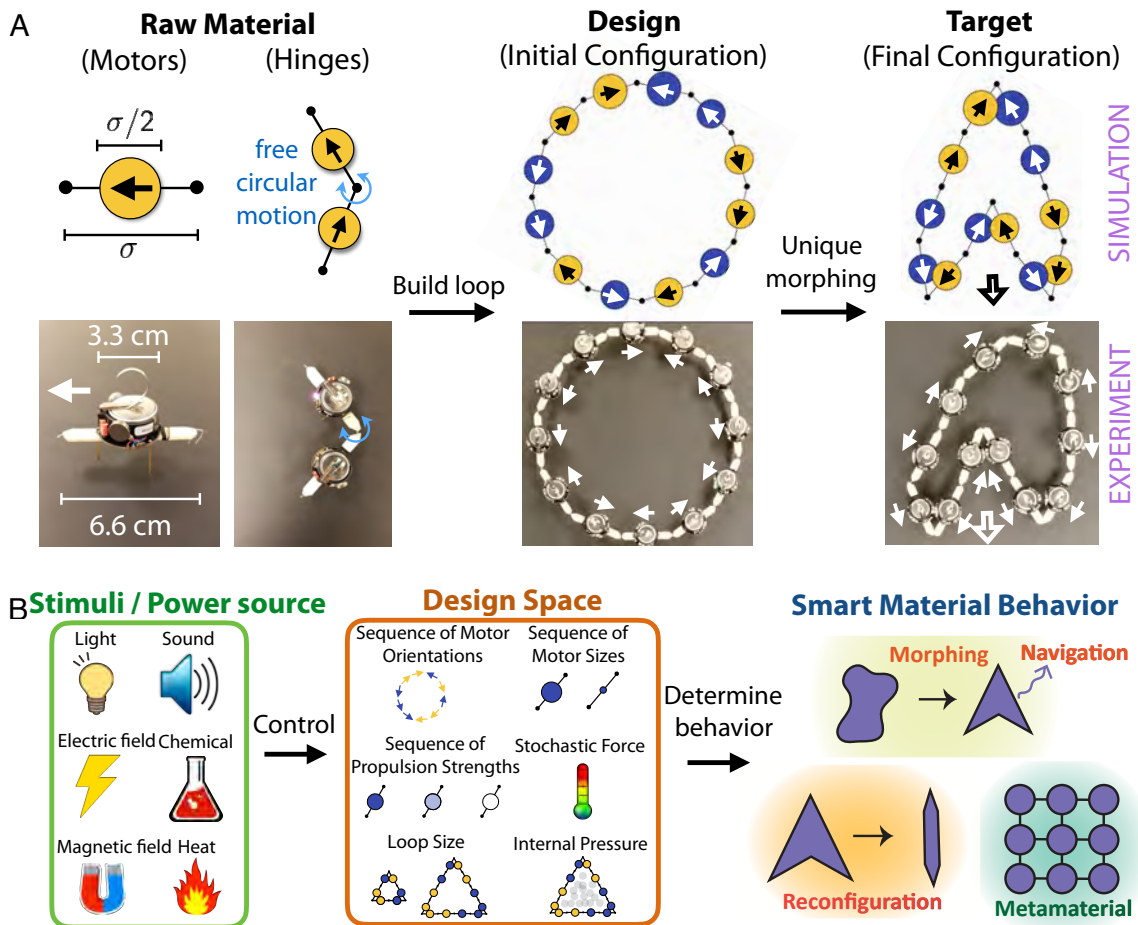
Fig. 3.1: System overview. (A) Constantly propelled motors are sequenced end-to-end in a loop using our design strategy to fold an *arrowhead* shape. Each motor can be arranged to point its propulsion in one of the two directions with respect to the loop (shown using arrows and yellow-blue colors for the simulation, and white arrows for the experiment). Design parameters for the shown loop are: motor orientations as colored; propulsion strength is identical on all motors; for simulation motor widths are $\sigma/2$ except for the two larger motors with width $0.6\,\sigma$ (analogous steric effect is obtained between the corresponding kilobots by shaping popsicle stick ends (Fig. 3.S1), described in Materials and methods); stochastic force is low ($\overline{T} = 0$ for simulation); loop size is 12 motors; and internal pressure is zero. (B) Schematic shows the conceptual robotic behavior. External stimuli powers and controls the shown design parameters of the loops. These design parameters determine the steady state of the loop that can be used to achieve smart behavior.

35

interactions between their robots via chemical signaling to achieve simple shapes with appendages. Their system is robust, but the target shapes lack the variety and precision we seek for submicron-scale robotic applications.

In the growing number of studies of macroscale or colloidal scale robots, the robots are free to move relative to one another, other than a confining boundary so they do not fall off the table or leave the simulation box. However, it is now possible to link together colloidal particles with sizes ranging from a few to a few hundred nanometers with, e.g., polymers[67] or DNA oligonucleotides[68, 69, 22] of nearly arbitrary length and stiffness. Motivated by these developments and the possibility of particle chaining, here we present an alternative design approach, shown in Fig. 3.1A, to program a system of non-intelligent motors (i.e. lacking on-board logic) into precise, preprogrammed behavior. We use motors that mimic active particles through constant forward propulsion. The novelty of our design is to connect the motors end-to-end in a loop such that each robot's propulsion force direction is always tangential to the loop. Each connection between neighboring motors allows motion only in the plane of the loop, constraining the possible behaviors to 2D as in the examples above. The only inter-motor interactions beyond steric interactions is this mechanical constraint, and thus programmability of the steady state loop shape (and subsequent behavior) is dictated by motor self-propulsion subject to these constraints, and the sequencing of motors along the loop. These motors do not employ any other form of communication and computation of the kind used in systems of Rubenstein *et. al.*[29], Li *et. al.*[40] and Slavkov *et. al.*citeSlavkov2018,. We perform experiments with several designs using kilobots to establish proof of concept, and use Brownian dynamics simulations to explore the rich design space and demon-

strate the scale invariance of our approach. We discuss the morphing mechanism as a consequence of three driving forces, which in turn are derived from the force interactions in the loop, and we provide a design procedure to reverse engineer the loop design for a given target shape. Beyond simpler behaviors, we demonstrate complex behavior using examples like *pacman* (dynamic behavior) and the letter *M* (static behavior) by decomposing the designed loop into simpler components and then combining them. To quantify the mechanical stability of the loop configuration, we present an analytical solution of the loop dynamics (see Theory in Materials and Methods), which also allows for quick estimation of forces and velocities on different loop configurations.

Six design parameters govern the force interactions (illustrated in Fig. 3.1B) and allow programmability. These are: 1) motor orientations with respect to the loop; 2) relative strengths of each motor's propulsion force; 3) relative motor sizes; 4) the strength of stochastic forces on the motors; 5) loop size; and 6) internal pressure within the loop. This scheme can achieve the complex emergent behavior schematically drawn in Fig. 3.1B. The external stimuli controlling these design parameters can be used both as the power source and the communication agent for controlling the loops. In this way, multiple responses can be programmed using a single set of design parameters to achieve either autonomous (environment response) or user-operated (external field response) smart behavior.
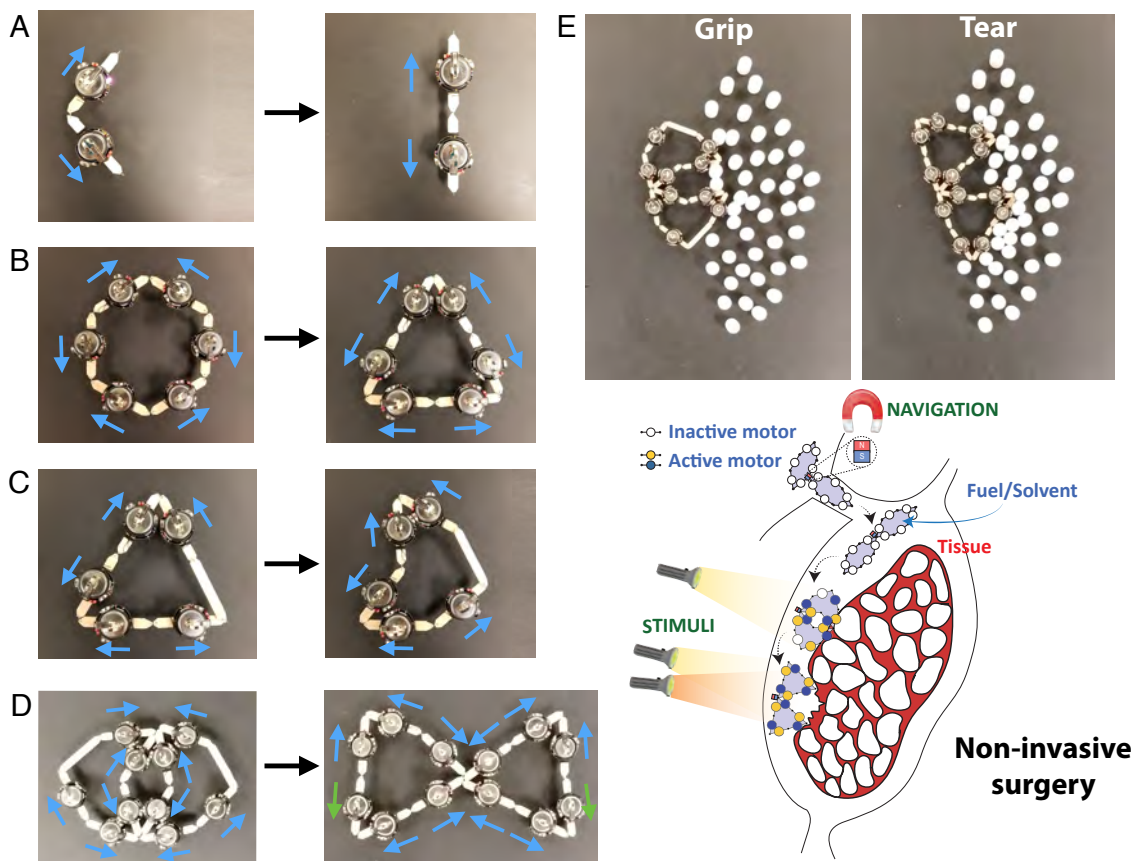
Fig. 3.2: Sequencing of kilobots. (A) Two kilobots with diverging propulsion at their joint straighten. (B) Loop composed of three segments each with the sequence shown in (A) folds into a triangle. (C) Replacing a kilobot of the triangle in (B) with a stick (passive state) generates net force driving the curving and rotation of the triangle. (**A-C**) Left and right images are the initial and final configurations respectively. (D) The *gripper* composite is formed by connecting two of the loop in (B-C). Switching between the active and passive state of the two motors (green arrow) achieves the closed (left) and open (right) states of the gripper. The arrows in (A-D) indicate the corresponding kilobot's direction. (E) Experimental demonstration showing the gripping and tearing operations on foam blocks. Below is the schematic of an envisioned non-invasive surgery at the micron scale. The 2-loop structure is guided by the magnetic field to the tissue. Different lights are used to activate the two configurations that are used to pinch and tear the tissue. Without activation, the loop is floppy and therefore is easily navigated through the narrow channel.

3.2 Kilobot experiments

We describe the basic design strategy by sequencing kilobots to form the *gripper* robotic machine shown in Fig. 3.2. Each kilobot is programmed to constantly propel forward to mimic a colloidal motor. All kilobots possess similar propulsion strengths. A small amount of stochastic force is introduced in the propulsion program (see SI). Loops are created by chaining kilobots together with popsicle sticks. At the simplest level of design, there is one stick between every two kilobots. Additionally, we can replace a kilobot with a popsicle stick (see Experiment in Materials and Methods), so that each motor exists in a ternary state – two states for orientation and a passive state (when the kilobot is replaced by a stick) – and the combinatorial permutations of active and passive kilobots provides programmability. When two kilobots are linked facing in opposite directions with a passive bot between them, their propulsion stretches them into a straight chain (shown in Fig 2A). This property is used to form straight segments of a shape. Fig. 3.2B shows a triangle folded using three such segments. Substituting a kilobot in one of the segments (Fig. 3.2C) with a passive stick introduces a net force on that segment to form a curved triangle with net rotation. To build a gripper two such triangle sequences are fused at a vertex as shown in Fig. 3.2D. Gripping behavior can be achieved by switching between passive and active states of the two corresponding motors. In Fig. 3.2E, we illustrate a noninvasive surgery cartoon as a robotic application where the closed and open gripper states are controlled by two different light sources. We demonstrate operations like gripping and incising (Fig. 3.2E) using kilobots and foam blocks.

In Fig. 3.3, we show several folded shapes achieved by using up to 12 kilobots. The *arrowhead* shape shown in Fig. 3.1B and Fig. 3.3C features a notch. Achieving this notch under low stochasticity requires an additional design parameter: local angle constraints. One way to achieve this is by replacing some kilobots with larger motors, as shown in simulation snapshots (Fig. 3.1B,3.3C), which increases the minimum angle possible between neighboring bots without steric hindrance (the role of this steric hindrance is discussed in the section on folding mechanisms). Because all kilobots are the same size, we tune the minimum angle between kilobots by shaping the ends of the popsicle sticks connected to them (see Experiment in Materials and Methods, Fig. 3.S1). The distorted folding of the arrowhead compared to its simulated counterpart is due to the imprecise nature of the kilobots. These demonstrations using kilobots – a relatively primitive "active particle"– demonstrates the plausibility of our design approach.

A Shapes with straight segments

B Shapes with straight/curved segments

C Shapes with straight / curved segments and zigzag features

D Composites

Pacman

Harmonic Spring

$10\,f_0$ · $25\,f_0$ · $25\,f_0$ · $10\,f_0$

Reversible
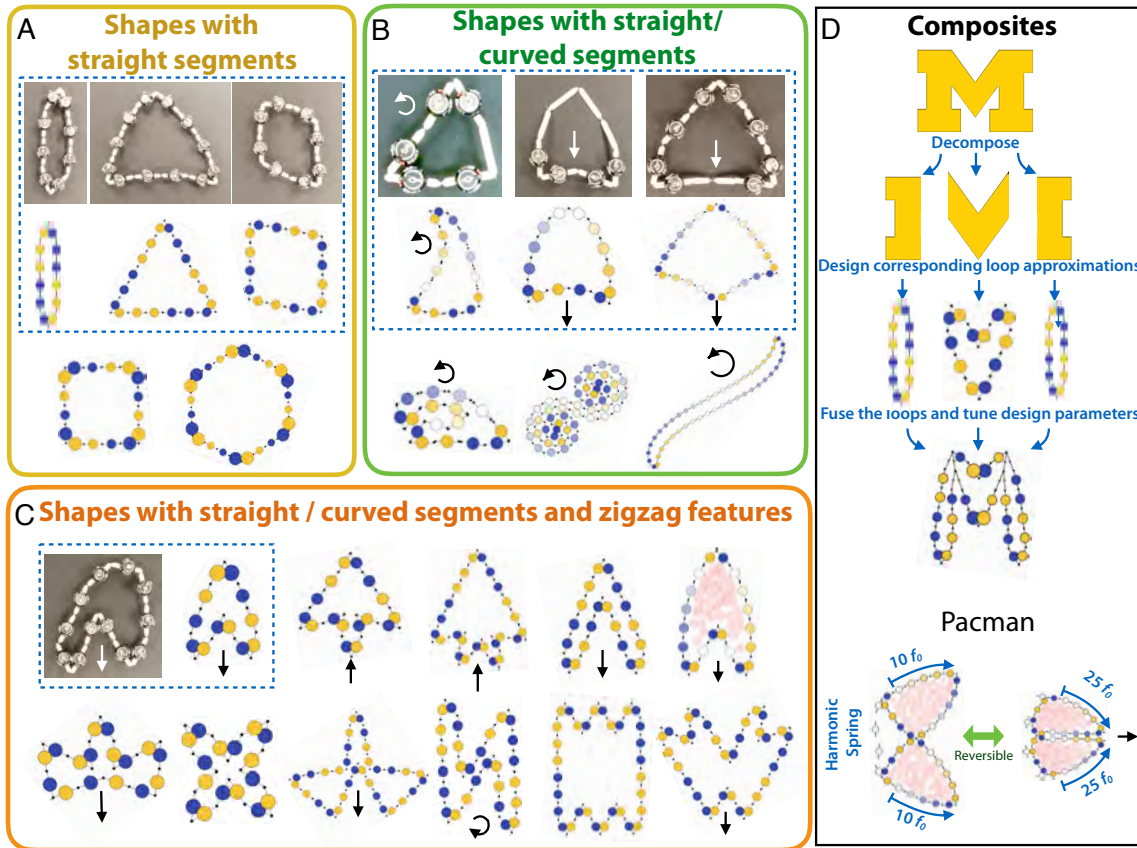
Fig. 3.3: Example range of targets. Our design scheme achieves shapes that can be constructed as straight or moderately curved lines (segments) connected at corners. Panels (A-C) show simulation snapshots of example shapes in increasing complexity. The key morphological features of these shapes are: straight segments, curved segments, zigzag geometry, net motion. The straight or curved arrows indicate the shape's net translation or rotation if present. Dashed blue line encloses simulation and experiment version of shapes. All shapes are stable at ($\overline{T} = 0.1$), though shapes in (A) and those corresponding to experiments do not require stochasticity to fold. The graded color opacity along some sub-segments–sets of similar colored consecutive motors–indicates linearly increasing propulsion magnitude. (D) Composites are multiple loops fused together and can achieve more complex behavior such as the letter *M* (Design procedure is shown, simulation snapshot is shown at the bottom), and *Pacman*. Simulation snapshots of the two states of pacman are achieved reversibly by tuning the net propulsion strength of the two sub-segments as shown. Harmonic spring is a chain of passive (white) motors bonded with harmonic coefficient $0.002\,k_0$. Reversible switching between the two states resembles the Pac-Man behavior. See Fig. 3.S2,3.S3 for the complete design parameters.

3.3   Active particle simulation

Extending the design space to all six parameters using simulations achieves a wider variety of shapes and motions (Fig. 3.3). To demonstrate this, we use Brownian dynamics simulations, a standard technique for studying active colloids that mimics their stochastic Brownian motion in solvent (see Simulation in Materials and Methods). The key morphological and dynamic features of the loop shapes designed and demonstrated in simulation are: (i) straight and curved segments of variable length, (ii) zigzag pattern, and (iii) net translation or rotation. All the shapes in Fig. 3.3 are stable under thermal (Brownian) forces. The target space of loop morphologies and behaviors extends to more complex robotic behavior by fusing multiple loops together into composites. In addition to the *gripper* example discussed above, Fig. 3.3 shows two more examples. The first example is the morphing of the loop into the letter *M*. The second example is a *pacman* shape, which uses two loops similar to the gripper but is more sophisticated. The closed state produces the net forward motion of the loop. Switching repeatedly between small and large propulsion strengths drives the system to reconfigure repeatedly between open and closed states while also propelling the robot forward in a way that resembles the arcade game character Pac-Man.
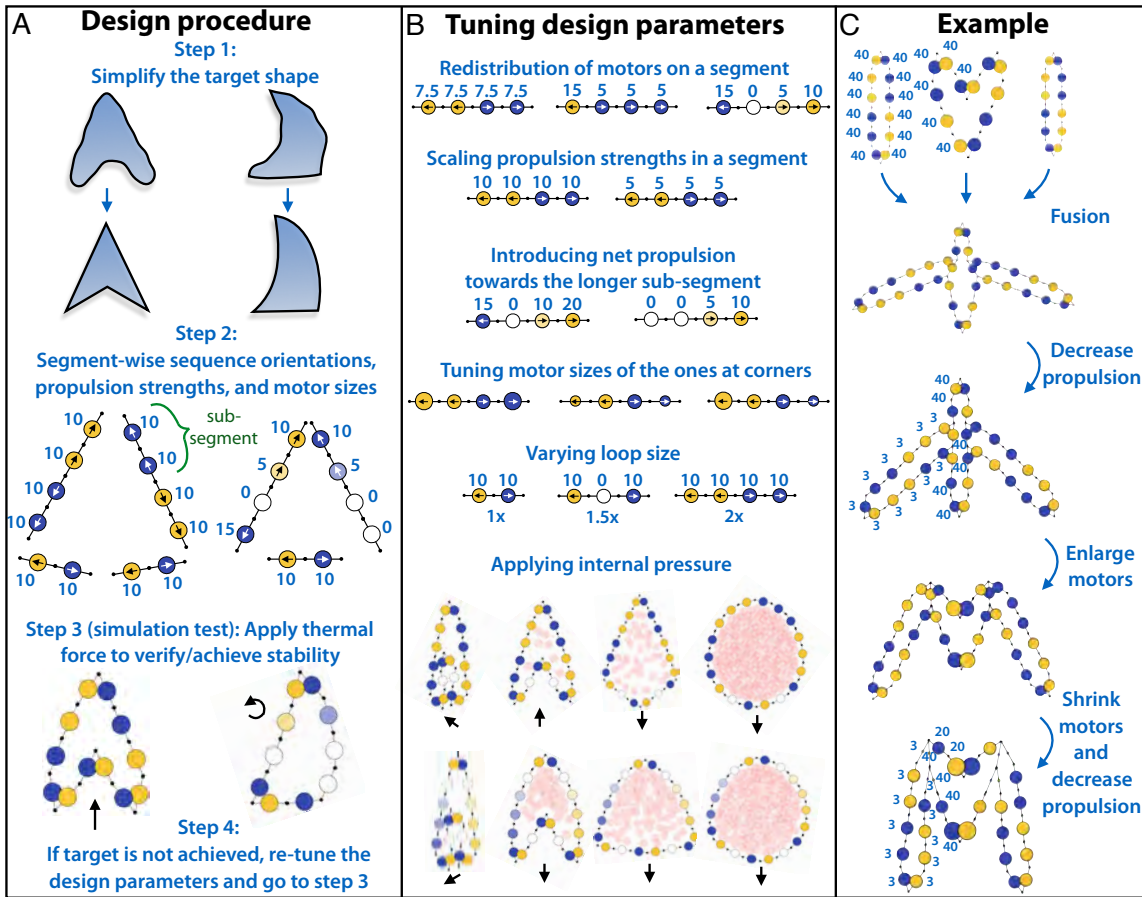
Fig. 3.4: Design procedure. (A) Shown is the general design procedure of identifying and tuning the design parameters given the target shape. Right and left follow the design for the two target shapes. This strategy generates a segmentation of the loop for the given target shape. (B) Illustrates the heuristics for re-tuning of the parameters, which is performed segment-wise. Bottommost rows show simulation snapshots of two loops with different internal pressure (Fig. 3.S4). Internal pressure is induced by adding soft particles inside the loop (see Materials and Methods for details). The numbers and internal arrows if shown for the motors are their propulsion strengths (in units of f_0) and orientations respectively. (C) Parameter tuning for the letter *M* (shown in Fig. 3.3).

3.4 Design procedure

The design procedure we employed to achieve the above results is comprised of four distinct steps (illustrated in Fig. 3.4), which can be used to generate any 2D shape:

Step 1:

The target shape is simplified to a set of straight or curved line segments connected end-to-end at corners. Each line segment corresponds to a loop segment. The number of loop segments is determined by the desired resolution of the morphological features. In Fig. 3.4A, we consider two examples: an arrowhead, with all straight segments, and a curved triangle, with two bends and one straight segment.

Step 2:

The orientations and propulsion strengths are sequenced segment-wise. Straight segments are formed by placing two sets of motors, or sub-segments, facing in opposite directions such that they pull away from each other as shown in Fig. 3.4. We use equal numbers of motors and equal propulsion forces in both sub-segments. If the segment size has an odd number of robots, we use a passive motor in the middle (see example in *Varying loop size* in Fig. 3.4).

To achieve curved segments, the two sub-segments are placed facing in opposite directions. With one of the sub-segments longer than the other, the segment can curve. Then, by linearly increasing the magnitude of the propulsion force along the sub-segment, its optimal stability is achieved when curved (discussed in Folding mechanism). By having a larger propulsion force on the longer sub-segment as compared to the shorter one, the curved segment is propelled forward in the direction of the net force (Fig. 3.4A).

Step 3:

We verified that the target shape folds into the desired shape and is mechanically stable under stochastic forces. For several shapes, thermal forces are apparently required for folding (shown in Fig. 3.3, discussed in Folding mechanism). Fig. 3.4

shows the simulation results of two designed loops in Step 3.

Step 4:

In the event that the target shape does not form, or is unstable, re-tune the design parameters as described in the next section and return to Step 3.

3.5   Tuning design parameters

We found the following heuristics help to navigate the enormous design space (illustrated in Fig. 3.4B). The first five heuristics operate segment-wise. These change the force interactions between the segments, which may vary the folding dynamics and hence the stable, steady-state configurations. When tuning these design parameters for a loop configuration, the analytical solution, developed using rigid body dynamics and given as $\dot{\theta} = f(\theta)$, where vector θ describes motor orientations, can be used to estimate the changes in the loop's folding pathway and to calculate the target shape's mechanical stability. Understanding of the loop folding mechanism provides further intuition for tuning design parameters. In the Fig. 3.S5 we show variations of the arrowhead shape achieved along different dimensions of the design space.

Redistribution of motors on a segment:

The relative number of motors in the sub-segments can be varied while maintaining the net propulsion force of each sub-segment. For a sub-segment, all motors have identical propulsion directions and may have either identical or linearly increasing magnitude.

Scaling propulsion strengths in a segment:

The propulsion strength of each motor in a segment is scaled by a constant factor.

Introducing net propulsion towards the longer sub-segment:

Given the sub-segment is longer than the other one and possesses linearly increasing propulsion strength, it can possess propulsion larger than the other sub-segment. This can be achieved by scaling up or down the propulsion forces on the longer or the shorter sub-segment, respectively.

Tuning motor sizes at corners:

The widths of the motors determine the minimum fold angle. The steric interactions governing the folding dynamics arise from the motors at the shape's corner, i.e. the motors at the ends of each segment. Therefore, the sizes of only these motors need to be tuned. In simulations, we vary the diameter of the central particle in a motor and in experiments, we shape the ends of the kilobot's stick (see Materials and Methods, Fig. 3.S1).

Varying loop size:

While all previous heuristics can be applied independently to a segment, every segment is scaled alike to vary the loop size. Given the scale factor of the loop size, each segment is scaled by maintaining the relative ratio of the number of motors in the sub-segments. If required, a passive motor between sub-segments can be used to maintain this ratio. If that is not possible, the motors can be redistributed using the first heuristic.

Applying internal pressure:

Encapsulating soft particles within the loop provides internal pressure, which additionally stabilizes different morphological features in the same loop. Fig. 3.4B (top and bottom) demonstrates this for two types of loop sequences. Without any internal pressure, the two loops fold into similar arrowhead shapes, although with different

net motion. A slight increase in internal pressure leads to bulkier arrowheads, with a noticeable difference between the two. Further increases in pressure produce polygons, and eventually circles.

Stochastic force:

Stochastic forces drive the loops to explore more of configuration space than is possible with only deterministic forces. The propulsion forces maintaining the loop in its steady-state shape restrain this exploration. The higher the temperature relative to the propulsion strength, the larger the amount of configuration space explored, which can assist in folding the target shape, switching between different shapes, and destabilizing the shape (discussed in Folding mechanism).

Composites:

Complex shapes, such as the letter *M*, demands many segments and more time to fold, and may possess multiple mechanically stable configurations resulting in a non-unique steady state. Some complex behaviors, such as the *gripper* and *pacman* examples, may not be feasible using a single loop. These complications can be avoided by using composites, where multiple loops are fused together, each sharing some part of their loop with the other (Fig. 3.3). The procedure to design composite loops is illustrated in Fig. 3.3 using the example of the letter *M*. First, the *M* is decomposed into simpler shapes. The number of these shapes depends on the desired resolution of the target, which is three for this example. The loops for these shapes are identified using the design procedure. Here, we need two rod-like loop shapes and an arrowhead loop shape. Finally, the loops are fused and the design parameters are re-tuned to achieve the target.

Fig. 3.4C shows the tuning of parameters for the letter *M*. Starting from the

47

composite of the sequences of two rod-shaped loops and an arrowhead loop, each motor was assigned a constant propulsion speed of $40\ f_0$. We observed that with this value, the rod-shaped loops form fast but spread wide. We then decreased the propulsion strengths on the rods to $3\ f_0$. We also increased the size of certain specific motors (as shown), which helped form the arrowhead (V-shaped) loop in the center of the letter. Further fine-tuning of specific motor sizes and propulsion strengths achieved the target letter shape. For the *pacman* (Fig. 3.3D), the lobes were filled with passive bots to provide internal pressure, sustaining the rounded morphology and increasing stability in the closed state. Harmonic springs were used to produce the open state. See Fig. 3.S3 for the complete design parameters of the three composites.

Navigation:

The motion of the folded shapes results from the loop sequence of the motors and thus the net propulsion force on the loop, which can be calculated *a posteriori* in simulations or *a priori* using the analytical solution. Naturally, any net motion will be along the asymmetric axis (see Fig. 3.3). There are (at least) three ways in which a loop can be navigated (shown in Fig. 3.5). The first way is by tuning the design parameters. For instance, enlarging motors of the arrowhead loop in Fig. 3.3A reverses the motion (Fig. 3.5 (left)). The second way is by assigning to each motor an additional propulsion force biased in the desired direction (Fig. 3.5(center)). A third way is to attach an external navigator to the loop, such as a magnetic navigator controlled via an external magnetic field (Fig. 3.5(right)).
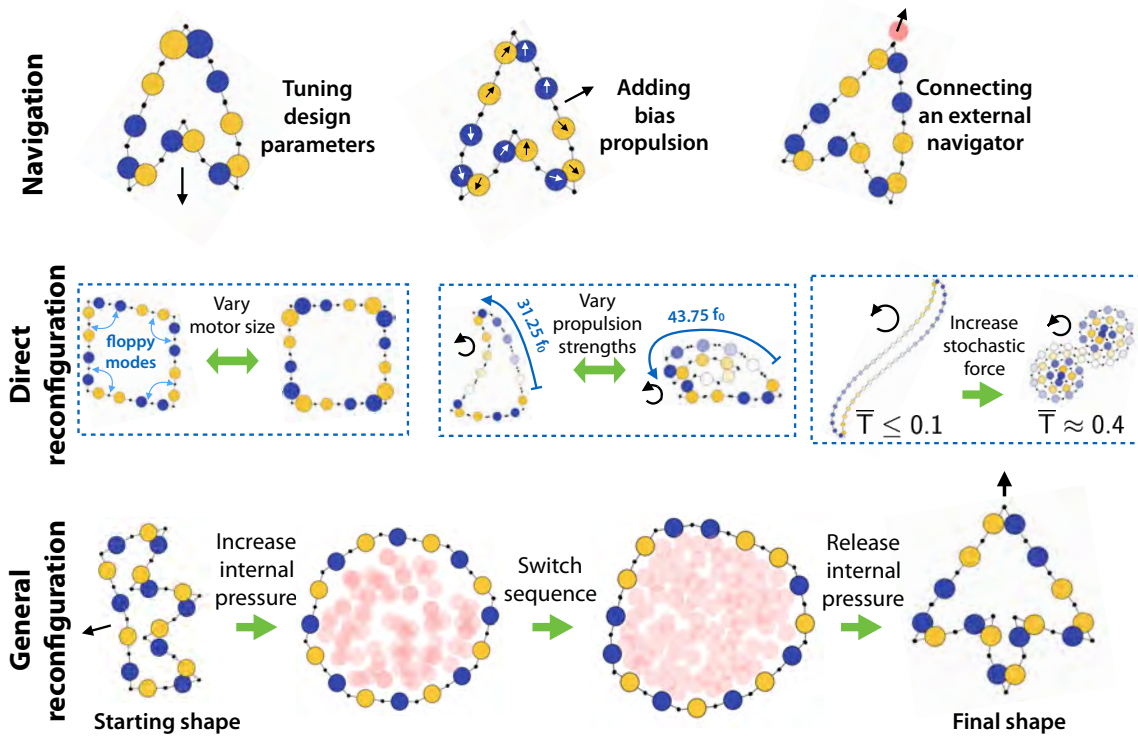
Fig. 3.5: Navigation and reconfiguration. Top row shows the simulation snapshots of examples describing three methods for directing the motion of the folded states. Middle-bottom rows are the two methods of reconfiguration between folded states are shown. In direct reconfiguration, tuning specific design parameters can directly reconfigure one state to other. The examples are: (left) floppy mode of the configuration removed by increasing selective motor sizes; (middle) two folded states reversibly reconfigured by tuning the propulsion strength of the shown sub-segment; and (right) the irreversible reconfiguration from the stretched to the coiled folded state achieved by increasing the temperature. In general reconfiguration, reconfiguration between arbitrary folded states can be accomplished by the procedure illustrated using an example.

3.6 Reconfiguring between different folded states

Reconfiguration between folded shapes proceeds by switching between the respective design parameters of each shape. In some cases, switching the parameters of one folded shape can directly reconfigure it into the second folded shape. We refer to these as direct reconfigurations (Fig. 3.5). In general, however, loop folding depends on the starting configuration and thus direct reconfiguring from one arbitrary configuration to another may not be possible or may lead to a mechanically trapped state.

Fig. 3.5 shows one method to achieve this general reconfiguration through an example. Starting from an arbitrary folded shape, the internal pressure is increased to inflate the loop into the highest symmetry shape possible. Then the design parameters are switched. For the example in Fig. 3.5, only the sequence of motor orientations is switched. The internal pressure maintains the inflated morphology. Subsequently, the internal pressure is reduced resulting in the new target shape. At the colloidal scale, such pressure variation can be actualized by using stimuli-responsive polymers that shrink in response to, for instance, solvent pH or salt concentration[17, 11]. Alternatively, inflation of the loop may be achieved by increasing electrostatic repulsion between motors or introducing elasticity between motors.

Driving Forces

A — Straightening Force / Curving Force / Notching Force

B

C — $n = 4$, 1.4σ, τ_{net}

D

E — $n = 4$, $n = 2$, Non-unique folding, $\overline{T} \lesssim 0.01$, $\overline{T} \lesssim 0.001$, $\overline{T} \approx 0.01$, $\overline{T} \gtrsim 0.1$

F — f_{tension}, x, $x = 0.52\sigma$, f_{net}, $n = 2$
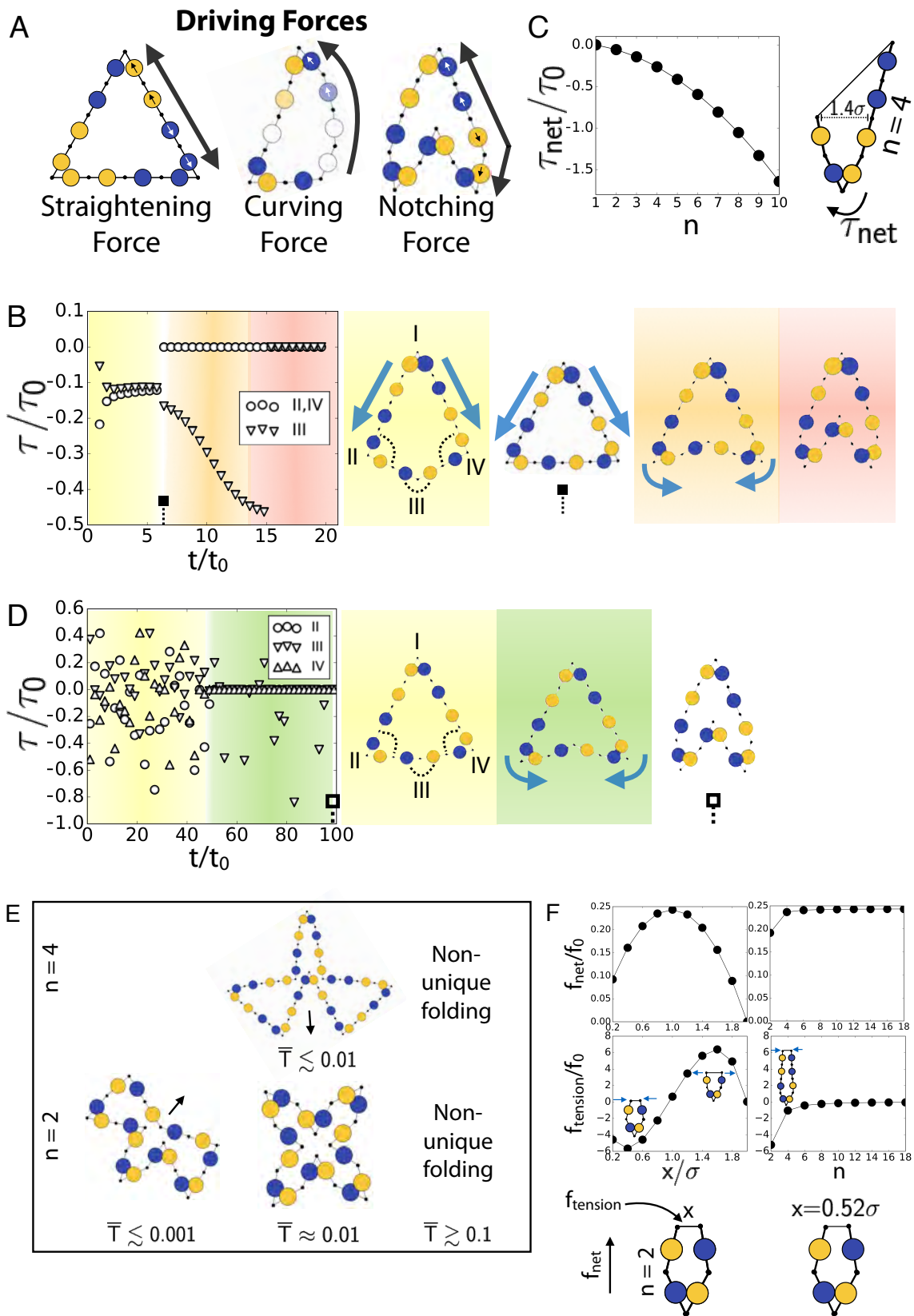
Fig. 3.6: Folding mechanism. (A) The three driving forces that drive the folding are indicated via arrows over one of the segments for each shape. (B) Plot of torque on the angles II, III and IV for the shown loop's simulation. The representative loop configurations at separate times are shown with their *notching force* (blue arrows). Negative torque decreases the angle. The shown loop is simulated at $\overline{T} = 0$ with propulsion strengths $10\ f_0$ for all motors. The two larger motors are of size $0.6\ \sigma$. The torque is calculated as $\gamma\,\Delta\dot{\theta}$, where $\Delta\dot{\theta}$ is the difference between rotational velocities of the two corresponding motors. Rotational velocities are calculated using the analytical solution $\dot{\boldsymbol{\theta}} = f(\boldsymbol{\theta})$, where $\boldsymbol{\theta}$ is obtained from the simulation. (C) Shown schematic is a pair of segments with ends tied by a harmonic bond of coefficient $0.01\ k_0$. Net torque, τ_{net} (γ_r times the net rotation measured in simulations), is plotted with respect to one of the segment sizes, n. Each simulation is initialized with straight segments at angle $\pi/3$ and folded at $\overline{T} = 0$ by tightening the harmonic bond until separated by distance 1.4σ. (D) Similar to (B) but the loop is simulated at $\overline{T} = 0.1$ and all motors are of size $\sigma/2$. (E) Phase diagram of an example with respect to $\overline{T}$ and n, the number of particles in each segment. The propulsion strength of all motors is $4\ f_0$. (F) Shown schematic is a pair of segments with ends tied by a harmonic bond of equilibrium length x and coefficient $0.01\ k_0$. Tension. $f_{tension}$, on this bond and net force, f_{net}, on the pair is plotted against x (fixing $n = 2$) and n (fixing $x = 0.25\ \sigma$). Forces are measured in simulations. Motors in (C), (F) possess unit propulsion strength.

3.7   Folding mechanism

The three major shape features–straight segments, curved segments, and zigzags–and their arrangement in a loop to achieve a desired shape are achieved via three respective driving forces shown in Fig. 3.6A. These driving forces in turn are governed by the loop's design, as described below using the *arrowhead* example.

Straightening force:

Connected sub-segments of motors acting in opposite directions stretch to form a straight geometry that is stable to mechanical perturbations. This opposing force is typically the strongest and, therefore, folding starts by straightening of all the segments. The size ratio of the two sub-segments does not affect the straightening, though it will affect the *notching force*. The propulsion force magnitudes along a sub-segment are either identical or monotonically increasing in the direction of the force. Both choices achieve straight segments within a shape, but each choice has implications for the other two folding forces. We find that a random distribution of force magnitudes over a sub-segment leads to unstable folding behavior.

Curving force:

This is the net force produced along a segment when the net propulsion force of its sub-segments do not cancel each other out, instead creating a curve. The degree of curvature increases with this net force (shown in Fig. 3.S6A for an example). For curved sub-segments, we use linearly increasing magnitudes of the propulsion forces. Under high curvature, sub-segments with identical magnitudes of propulsion forces on the motors are unstable to mechanical perturbations. In general, stabilizing higher curvatures require higher gradients of variation in the magnitude

of propulsion forces along a segment (see Fig. 3.S6B for results exploring different gradients).

Notching force:

When neighboring segments attempt to fold beyond what is permissible by steric hindrance, they bend at a corner as shown in Fig. 3.6A (third image). This bending generates a net force on the pair of corner segments, which we refer to as the notching force. In Fig. 3.6, we show how this driving force folds the arrowhead shape.

The loop in Fig. 3.6B is folded at $\overline{T} = 0$. The figure plots torques generated at angles II, III and IV as the folding proceeds in time. Negative torque acts to reduce the angle. Folding starts by straightening the segments. Complete straightening of the segments $I - II$ and $I - IV$ is prevented by the larger steric hindrance between the motors at corner I. This generates a net notching force on segments $I - II$ and $I - IV$, pulling them downward. This motion in turn reduces angles II and IV. When these angles decrease below $\pi/3$, steric hindrance prevents further folding at these angles as indicated by $\tau = 0$ for $t \leq 6$ t_0 (Fig. 3.6B). Consequently, neighboring segments bend at corners II and IV, generating net torques on segment pairs $I - II$ and $II - III$, and $I - IV$ and $III - IV$ (see the third snapshot in Fig. 3.6B). These net torques are such that they further enforce the folding at angle III until blocked by steric hindrance for $t \leq 15$ t_0. We measure the net torques on pairs of segments with different lengths in Fig. 3.6C by folding such pairs in simulations, connecting the ends via a harmonic bond (see Materials and Methods). The plot shows that such a pair always rotates from the longer to shorter segment with a net torque proportional to their length ratio. This property explains the formation and

stabilization of the arrowhead.

Although the folded state of this arrowhead is stable under stochastic (thermal) forces, it does not *require* the stochastic forces for folding. In Fig. 3.6D, we fold a similar loop that does not use larger motors as used above, but instead requires thermal noise. Fig. 3.6D plots torques on the shown angles of this loop similar to Fig. 3.6B. Starting from the circular configuration, all segments of this loop straighten (see first snapshot of Fig. 3.6D). No unbalanced forces are yet present in this configuration. Thermal forces cause the loop to fluctuate in configuration space around an average shape. Since the shape stiffness is minimum at the corners, the fluctuations are maximum there. The plot in Fig. 3.6D shows that angles II, III and IV fluctuate randomly until $50\ t_0$, when the system finds the configuration containing the *notching force*. These torques, shown in the second snapshot of Fig. 3.6D, fold angle III inwards, as indicated by negative τ_{angle} for $50\ t_0 < t < 100\ t_0$. Beyond $100\ t_0$, the arrowhead is stabilized and any residual torques are due to thermal fluctuations. Thus, the role of thermal forces in this example is to explore configuration space, which is useful for folding complex shapes.

Since thermal forces control the exploration of shapes around the optimum shape in configuration space, loops at different temperature may fold into different shapes. This behavior is shown in Fig. 3.6E(bottom row) for a loop with eight segments, each containing n particles. To gain insight into this behavior, we folded a pair of segments as in Fig. 3.6C and measured the net force, f_{net}, on the pair and tension, $f_{tension}$, on the bond, with length x, between end points (Fig. 3.6F). This pair corresponds to pairs of segments in Fig. 3.6E(bottom row). Higher temperature causes increased bending of the segments, corresponding to lower x. The two regions with $\overline{T} = 0.001$

and 0.01 in Fig. 3.6E (bottom row) correspond to $x \gtrsim 1$ and $x < 1$, respectively. Fig. 3.6F shows $f_{tension}$ moves from positive to negative values as x moves from > 1 to < 1. Thus, the loop fluctuating under larger thermal forces forms pairs of segments under negative tension, whereas loops under smaller thermal forces fold differently. When $x \approx 1$, f_{net} is maximum. At $\overline{T} = 0.001$, $x \approx 1$ for only one pair of arms and that drives the net motion of the shape. At $\overline{T} = 0.01$, every pair of arms pushes towards the center of the shape, canceling out the net motion and increasing the shape's stability. Large thermal forces result in unstable folding behavior and do not produce a unique steady state shape (shown in Fig. 3.6E). Fig. 3.6F shows that $f_{tension}$ rapidly decreases in magnitude as n increases from 2 to 4, which corresponds to Fig. 3.6E(middle column). This is because the tension on the pair at $n = 4$ is not sufficient to stabilize a similar shape formed at $n = 2$. Also, $f_{tension}$ saturates for $n > 4$ as it does for the shape in Fig. 3.6E, corroborating the influence of the notching force on the folded state.

3.8 Quantifying stability of the folded state

For non-zero thermal force, different shapes exhibit different shape fluctuations in steady state. To estimate these fluctuations, we apply linear stability analysis[70] on the rotational degrees of freedom of the loop. The analytical solution $\dot{\boldsymbol{\theta}} = f(\boldsymbol{\theta})$ is approximated in the linear limit to obtain $\delta\dot{\boldsymbol{\theta}} = F \, \delta\boldsymbol{\theta}$, where vector $\boldsymbol{\theta}$ contain particle orientation and F is the Jacobian matrix calculated for the steady state (at $\overline{T} = 0$) loop shape (see Theory in Materials and Methods). Fig. 3.7A plots the eigenvalues of F for different shapes. For comparison purposes, the average magnitude of the propulsion force on motors within a shape is fixed. All the eigenvalues are non-
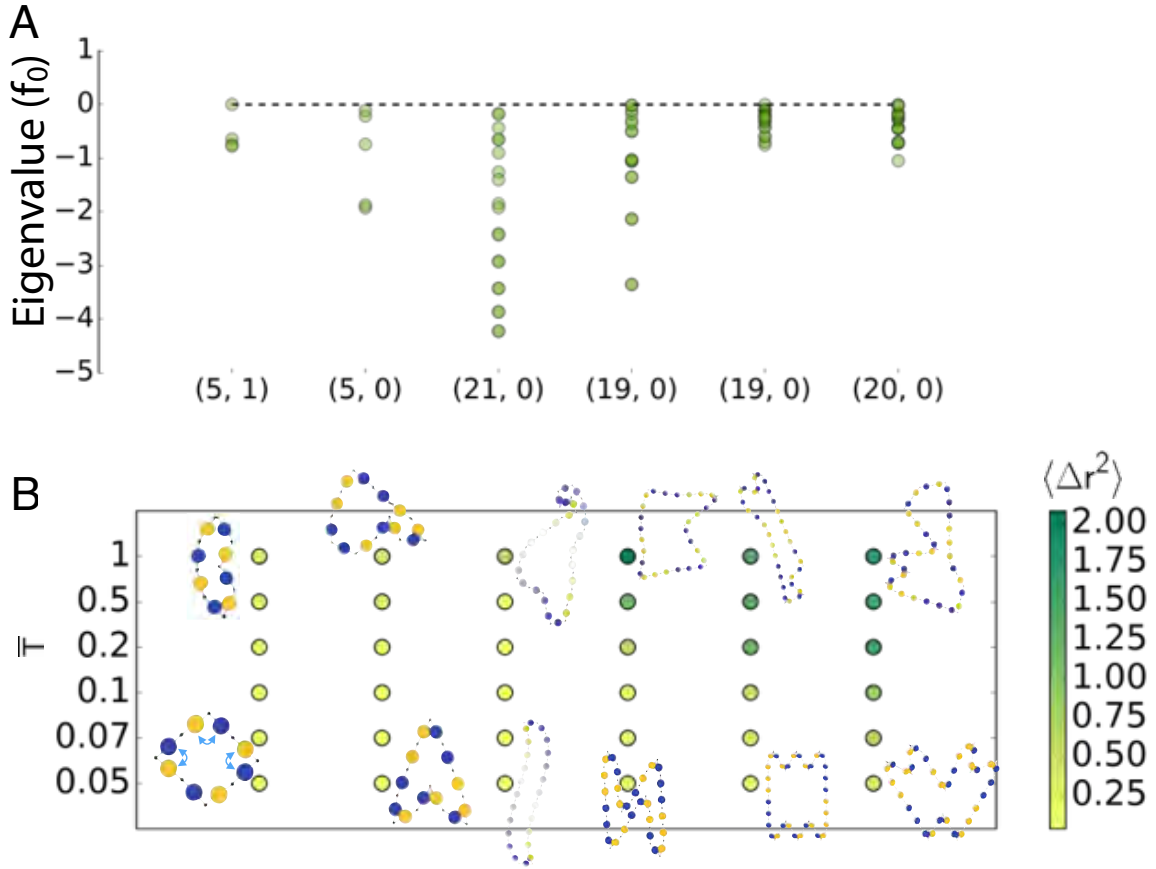
Fig. 3.7: Stability analysis. (A) Eigenvalues corresponding to the folding modes of different loop configurations are plotted. Only the first configuration–*square*–possesses a floppy mode. Calculated are the eigenvalues of F from the analytical solution $\delta\dot{\boldsymbol{\theta}} = F\delta\boldsymbol{\theta}$. The mean propulsion force of each loop is set to unity for comparison purpose. Only those eigenvalues are plotted whose eigenvectors have more than 98 percent projection into the kinematic space (see Materials and Methods for details). The values inside the brackets along the x-axis are the number of folding modes and number of floppy modes. The dotted line marks the eigenvalue zero. $\boldsymbol{\theta}$ corresponds to the equilibrium state. (B) Heatmap of average fluctuation, $\langle \Delta r^2 \rangle$, of the steady states of loops at different $\overline{T}$. $\langle \Delta r^2 \rangle$ is the difference of the distance of a motor from the shape's center-of-mass calculated between the thermal steady-state and the equilibrium state, and averaged over all motors and 1000 simulation frames. The mean propulsion of each simulated loop is set to $6\ f_0$. Equilibrium state is achieved by folding the shape at $\overline{T} = 0.05$ and then cooling down to $\overline{T} = 0$. Representative simulation snapshots at lower and higher $\overline{T}$ are shown. See Fig. 3.S7 for the complete sequence of propulsion forces.

positive, which indicates that the folding modes are either stable or neutral. Only the first shape has a neutral/floppy mode corresponding to the eigenvalue zero. Moving left to right, the number of modes with higher eigenvalues increases, suggesting reduced stability, which is also evident by the increase in fluctuations observed in simulations and plotted in Fig. 3.7B.

3.9 Conclusion

3.9.1 Summary

We described a design strategy to build robotic machines by using constantly propelled particles, referred to as motors. By design, these motors lack on-board computation, individual identity and memory, hence mimicking active colloids – the intended raw material for our machines. Our strategy is to hinge these motors end-to-end in a closed loop. Hinging techniques for colloidal particles largely use polymers[67] and DNA[68, 69, 22]. Communication between motors is only via steric interaction and hinge constraint, due to which the system is material and environment agnostic. The loop folds into a prescribed shape and motion as encoded via six design parameters, including the sequences of motor orientations and propulsion strengths, motor size, magnitude of the stochastic forces, loop size and internal loop pressure. These design parameters are to be regulated via external stimuli (Fig. 3.1B) to build desired robotic machines. We investigated the design space in experiments using centimeter scale *kilobots*[33] to demonstrate the simplest designs requiring the fewest robots, and in colloidal scale Brownian dynamics simulations to validate scale invariance and explore complex loop designs. By fusing multiple loops, complex shapes such as the (letter *M*) and complex dynamic

behavior as demonstrated in the (*gripper* and *pacman*) loops can be achieved. We described how to reverse engineer the loop design for a given shape and provided ways to control its navigation and reconfiguration. Using simulations and analytical theory–developed using rigid body dynamics–we described the folding mechanism and quantified the stability of loop configurations.

3.9.2 Applications

Our loops can conceivably be refined in the future for non-invasive medical surgery where the shape of the loops can be manipulated via external fields (Fig. 3.2E). Since these loops are malleable, they should easily squish through delicate tissues and activated on demand using ultrasound or lasers to perform targeted diagnostics and drug delivery. Materials researchers can employ ensembles of loops to self-organize novel structures or manipulate micron-sized machine parts for bottom-up fabrication. Smart textiles can be fabricated as a metamaterial comprising a network of loop composites. Fig. 3.8 illustrates several envisioned, far-future applications of our system as autonomous and user-controlled reconfigurable machines.

A **Contaminant Capture**
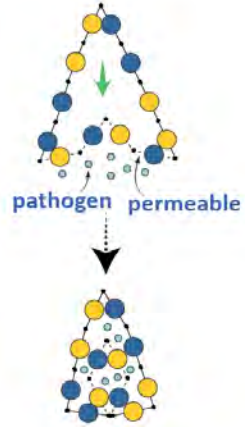
B **Lab-on-a-chip**
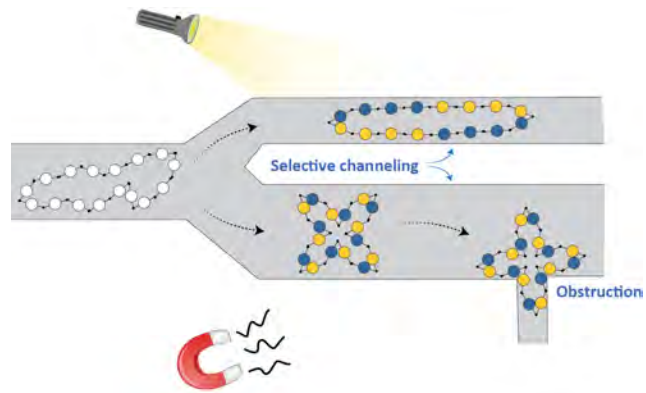
C **Micro-manufacturing**
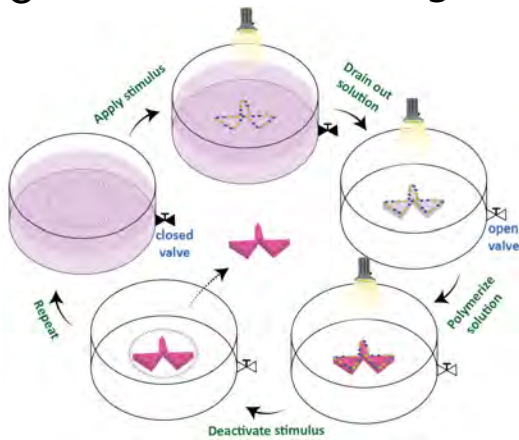
D **Controlled Drug Release**
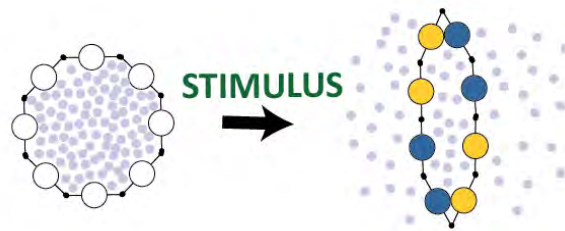
E **Vibration sensor**

F **Metamaterial with tunable mechanical/optical property**
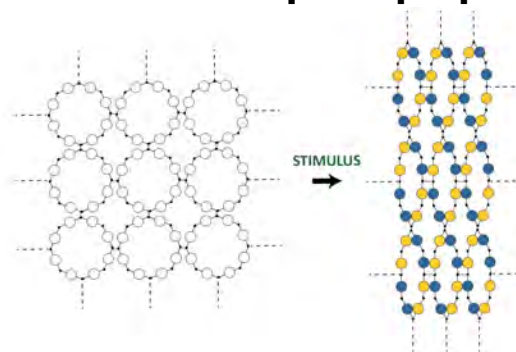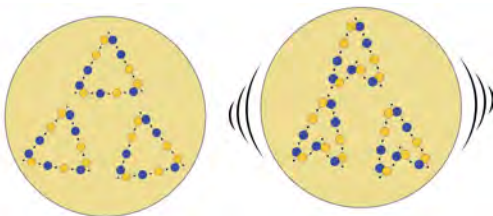
Fig. 3.8: Applications. (A) The actuated loop moves exposing the bottom boundary that is permeable to contaminant. Sufficient contaminant triggers the loop to close the bottom boundary and entrap the contaminant. In practice, such contaminants can be spilled oil in the oceans, impurities in chemical products, pathogens in body. (B) The loop travelling through a microfluidic channel is actuated using different stimuli to selectively channel loops based of shape and/or create obstruction. (C) Fast and clean bulk manufacturing of micron scale shapes shown via a single enlarged loop. The loops act as reusable molds. (D) Embedded drugs release from the semi-permeable boundary due to pressure applied when the loops are actuated. (E) Vibration sensor formed by the system of loops that reconfigure in the presence of stochasticity. The change in electronic, mechanical or optical property of the system can be measured to detect vibrations. The shaded part of the sensor can be fuel or support material. (F) Material formed by connecting loops into a square lattice. The material's phase changes when the loops are actuated, thus, changing its mechanical and optical properties.

3.9.3 Future directions

Future studies might explore numerous other variations of our design scheme. Examples include removing the constraint that all propulsion forces on robots be tangential to the loop, or tethering loops rather than having them be freely floating. The experimental, simulation and analytical models we provided can be easily extended for such generalized cases. Theory and simulations can find ways to improve the robustness and stability of complex loops. Breaking the planar positioning of motors is another prospect that will generate 3D loop structures. Experiments can focus on how to synthesize composites to enable complex designs and how to efficiently regulate the design space via external stimuli in order to program multiple configuration states into a single system. Another interesting anticipated experimental idea would be the synthesis of hybrid systems comprising electronics as well as nanoparticles into loops. Other interesting areas to investigate include the effects of particle-particle interactions such as attraction, repulsion, dipolar interactions and hydrodynamics on the system.

3.10 Materials and Methods

3.10.1 Experiment

For experimental demonstration of our design, we use kilobots[33], bought from RoadNarrow Robotics along with a charging unit and an overhead controller. Each kilobot is 33mm in diameter and moves using left and right motors. Each kilobot is attached at the center of a 66mm popsicle stick. The kilobots face along the length of their popsicle sticks so that any motion of a kilobot will be always tangential to the loop at that kilobot's location. The left and right motors rotate a kilobot towards left

and right respectively with a turn radius. This effect is exploited to propel the bots forward by alternatively actuating left and right motors (see SI for the microcontroller code programmed into the kilobots). The motors are manually calibrated to match the left and right rotational speeds to $\pi/5\ s^{-1}$. To introduce stochasticity, the duration of the motor actuation is randomly chosen within 200ms. The ends of the popsicle sticks are drilled with tiny holes with cut corners (Fig. 3.S1). A pair of bots are connected to each other by inserting a bent pin in the corresponding holes, which allows for the folding degree of freedom. The minimum fold angle is determined by the angle of the cuts at the corners (Fig. 3.S1). Large variations in the propulsion force is difficult for kilobots, therefore, all motors are calibrated to exert the same force. In cases where a bot with zero propulsion is required in a loop, a popsicle stick of equal length is used in its place. Importantly, we did not use the intercommunication feature of the kilobots. Thus, the kilobots do not interact with each other other than through the mechanical forces conveyed by the popsicle sticks, and by steric constraints. All experiments were performed on a single flat surface, on which motors were calibrated and start from a circular initial configuration. Slight deviations of some shapes observed in experiments as compared to simulations are possibly due to imprecise motor calibration and approximation of the sequence.

3.10.2   Simulation

Each motor in a loop is modeled as a disk of diameter $\sigma/2$ with two diametrically opposite hinge ends at $\sigma/2$ distance from the center of the disk. Volume exclusion between adjacent motors determines the minimum angle of the fold possible between them, which in our case is $\pi/3$. The loops are simulated in two dimensions

with periodic boundary conditions using the simulation toolkit HOOMD-blue (v2.2.1) [59, 60, 61, 71, 72]. The dynamics of motor i is simulated using the Brownian equation of motion[62].

$$\dot{\boldsymbol{r}}_i = \frac{1}{\gamma}(\boldsymbol{F}_i + f_i^a\,\hat{\boldsymbol{e}}_i) + \sqrt{2\frac{kT}{\gamma}}\,\boldsymbol{\eta}(t) \tag{3.1}$$

$$\dot{\theta}_i = \tau_i/\gamma_r, \tag{3.2}$$

where $\boldsymbol{r}_i$ and θ_i are the position and orientation of motor i respectively. $\boldsymbol{F}_i$ and τ_i are the net force and torque on i due to volume exclusion interactions and harmonic bonds. Volume exclusion is applied between disks of motors. To prevent self-intersection of loop, volume exclusion similar to that of disks is applied between the hinges. Other than preventing the unphysical self-intersection, this force do not influence the folding dynamics. Volume exclusion interactions between centers at r distance apart is modeled via the Weeks-Chandler-Andersen potential, $U_{WCA}(r) = 4\epsilon\left[(\sigma'/r)^{12} - (\sigma'/r)^6)\right] + \epsilon$, for $r < \sigma/2$, and $U_{WCA}(r) = 0$ otherwise [63], where $\sigma' = \sigma/\left(2 \times 2^{1/6}\right)$ and ϵ determines the strength of the potential. We set $\epsilon = 10^{-4}k_0\,\sigma$ for our system. A hinge is modeled via harmonic bond between adjacent motors with strength k_0 and equilibrium length set to zero. The propulsion force, f_i^a, acts along $\hat{\boldsymbol{e}}_i$, which is a unit vector along the axial direction of the motor i. Hence, each f_i^a acts tangentially to the loop and will point either along the clockwise or anticlockwise direction relative to the loop. The forces and torques are nondimensionalized using $f_0 = 10^{-3}k_0\,\sigma$ and $\tau_0 = 10^{-3}k_0\,\sigma^2$ respectively. Nondimensional thermal energy $\overline{T} = kT/10^{-3}k_0\,\sigma^2$ and is set to 0.1 unless specified otherwise, and $\boldsymbol{\eta}(t)$ is unit-variance Gaussian white noise. γ_r is the rotational drag coefficient and

is set equal to the translational drag coefficient, γ. The rotational noise in a motor orientation arises from the translational diffusion of the adjacent motors bonded to it. Time is measured in units of $t_0 = \gamma/(10^{-3}k_0)$. All the simulations are initialized from the circular configuration unless otherwise stated and equilibrated for at least $500\ t_0$ before measuring any quantity. Precision of folding is validated *via* 20 replicas each.

3.10.3 Theory

We use rigid body dynamics to develop the analytical solution for the loops [73]. Each motor is treated as a rigid body. The joint between neighboring motors possesses rotational degree of freedom. The objective is to calculate the angular velocity vector as a function of orientation vector, $\dot{\boldsymbol{\theta}} = f(\boldsymbol{\theta})$, where $\dot{\boldsymbol{\theta}}$ and $\boldsymbol{\theta}$ contain angular velocities and orientations, respectively, of the motors in the loop. Each rigid body in 2D possesses two translational and one rotational degrees of freedom. The force balance for the loop along each degree of freedom can be written as

$$A\boldsymbol{f_x^J} + \sum_m^M f_m^{ex}\boldsymbol{k_x^m} + \boldsymbol{f_x^a} = \Gamma\boldsymbol{v_x} \tag{3.3}$$

$$A\boldsymbol{f_y^J} + \sum_m^M f_m^{ex}\boldsymbol{k_y^m} + \boldsymbol{f_y^a} = \Gamma\boldsymbol{v_y} \tag{3.4}$$

$$S\left(\boldsymbol{f_x^J} + f_x^J\boldsymbol{1}\right) - C\left(\boldsymbol{f_y^J} + f_y^J\boldsymbol{1}\right) = \Gamma_r\dot{\boldsymbol{\theta}}, \tag{3.5}$$

where each row corresponds to the force balance on a motor in a loop. $\boldsymbol{f_x^J}$ and $\boldsymbol{f_y^J}$ are joint forces in x and y directions. Scalar variables f_x^J and f_y^J are added to their corresponding vectors to ensure kinematic constraints. $\boldsymbol{v_x}$ and $\boldsymbol{v_y}$ are translational

velocity vectors. $\boldsymbol{f_x^a}$ and $\boldsymbol{f_y^a}$ are propulsion forces in x and y axis. The magnitude of volume exclusion forces between the mth pair of overlapping motors is f_m^{ex}. $\boldsymbol{k_x^m}$ and $\boldsymbol{k_y^m}$ contain contributions per unit of f_m^{ex} in x and y directions on each motor, where this contribution is non-zero only for the motors in the mth pair and is a function of their orientations. M is the total number of overlapping pairs. The matrices A, S, C, Γ and Γ_r are square matrices of size N, which is the number of motors in the loop.

$$
A = \begin{bmatrix}
1 & -1 & 0 & \cdots & 0 & 0 \\
0 & 1 & -1 & \cdots & 0 & 0 \\
\vdots & \vdots & \vdots & \ddots & 0 & 0 \\
0 & 0 & 0 & \cdots & -1 & 0 \\
0 & 0 & 0 & \cdots & 1 & -1 \\
-1 & 0 & 0 & \cdots & 0 & 1
\end{bmatrix}, \ S = \begin{bmatrix}
\sin\theta_0 & \sin\theta_0 & 0 & \cdots & 0 & 0 \\
0 & \sin\theta_1 & \sin\theta_1 & \cdots & 0 & 0 \\
\vdots & \vdots & \vdots & \ddots & 0 & 0 \\
0 & 0 & 0 & \cdots & \sin\theta_{N-3} & 0 \\
0 & 0 & 0 & \cdots & \sin\theta_{N-2} & \sin\theta_{N-2} \\
\sin\theta_{N-1} & 0 & 0 & \cdots & 0 & \sin\theta_{N-1}
\end{bmatrix}.
$$

C is equivalent to S but with cosine of θs. Γ is the diagonal matrix containing drag coefficients, γs, of the corresponding motors. The kinematic constraints ensuring loop connectivity during motion are given by

$$
B\boldsymbol{v_x} = H_x\dot{\boldsymbol{\theta}} \tag{3.6}
$$

$$
B\boldsymbol{v_y} = H_y\dot{\boldsymbol{\theta}}, \tag{3.7}
$$

where

66

$$B = \begin{bmatrix} 1 & 0 & 0 & \cdots & 0 & -1 \\ -1 & 1 & 0 & \cdots & 0 & 0 \\ 0 & -1 & 1 & \cdots & 0 & 0 \\ \vdots & \vdots & \vdots & \ddots & 0 & 0 \\ 0 & 0 & 0 & \cdots & 1 & 0 \\ 0 & 0 & 0 & \cdots & -1 & 1 \end{bmatrix}, \; H_x = -\frac{\sigma}{2} \begin{bmatrix} \sin\theta_0 & 0 & 0 & \cdots & 0 & \sin\theta_{N-1} \\ \sin\theta_0 & \sin\theta_1 & 0 & \cdots & 0 & 0 \\ 0 & \sin\theta_1 & \sin\theta_2 & \cdots & 0 & 0 \\ \vdots & \vdots & \vdots & \ddots & 0 & 0 \\ 0 & 0 & 0 & \cdots & \sin\theta_{N-2} & 0 \\ 0 & 0 & 0 & \cdots & \sin\theta_{N-2} & \sin\theta_{N-1} \end{bmatrix}.$$

H_y is equivalent to H_x but with cosines of θs and the prefactor of $+\sigma/2$. Substituting vector variables v_x and v_y from Eq. 6, 7 into Eq. 3, 4 and subsequently substituting f_x^J and f_y^J into Eq. 5 yields

$$Z\,\dot{\boldsymbol{\theta}} = \sum_m^M f_m^{ex}\boldsymbol{a_m} + f_x^J\boldsymbol{b} - f_y^J\boldsymbol{c} + \boldsymbol{d}, \tag{3.8}$$

where $\boldsymbol{a_m} = CA^{\dagger}\boldsymbol{k_y^m} - SA^{\dagger}\boldsymbol{k_x^m}$, $\boldsymbol{b} = S\mathbf{1}$, $\boldsymbol{c} = C\mathbf{1}$, $\boldsymbol{d} = -SA^{\dagger}\boldsymbol{f_x^a} + CA^{\dagger}\boldsymbol{f_y^a}$ and $Z = \Gamma_r - SA^{\dagger}\Gamma B^{\dagger}H_x + CA^{\dagger}\Gamma B^{\dagger}H_y$. Superscript $\dagger$ represents the pseudo-inverse. In the rigid body formulation, there is no explicit volume exclusion potential. Wherever a pair of motors overlap, their centers are connected by a rigid rod and the motors are assumed to be pinned to each other, and rotated with the same velocity. Generally, the placement of this rigid rod is shape dependent. To incorporate this, we substitute $\boldsymbol{\theta} = D\boldsymbol{\theta'}$, where $\boldsymbol{\theta'}$ contains $N - M$ non-redundant orientations and D is a $N \times N_M$ matrix that duplicates the required entries of $\boldsymbol{\theta'}$. Consequently, the singular value decomposition (SVD) of ZD will have a null space of size M. Reference [74] explains the usage of SVD for evaluating kinematic and dynamic information of a network system. Let $\beta_m s$ be left-singular vectors corresponding to this null space. In order to satisfy Eq. 8, the projection of the right hand side on each of β_m must be

zero, which gives us M additional constraints,

$$\beta_m^T \left(\sum_m^M f_m^{ex} \boldsymbol{a_m} + f_x^J \boldsymbol{b} - f_y^J \boldsymbol{c} + \boldsymbol{d} \right) = 0, \text{ where } m = 0 \text{ to } M - 1. \tag{3.9}$$

Similarly, to satisfy kinematic constraints (Eqs. 6, 7), $H_x \dot{\boldsymbol{\theta}}$ and $H_y \dot{\boldsymbol{\theta}}$ must have zero projection on the left-singular vector corresponding to the null space of B, which is $\mathbf{1}$ generating two additional constraints,

$$\mathbf{1}^T H_x \dot{\boldsymbol{\theta}} = 0 \tag{3.10}$$

$$\mathbf{1}^T H_y \dot{\boldsymbol{\theta}} = 0. \tag{3.11}$$

Finally, $\dot{\boldsymbol{\theta}}$ is calculated using Eqs. 8-11.

To measure stability of a loop shape around its steady state value, we use linear stability analysis[70], where Eqs. 3-7 are approximated in the linear limit. Overlapping particles are assumed to fluctuate together in the linear limit. By applying similar derivation as above, $\delta \dot{\boldsymbol{\theta}}' = F \delta \boldsymbol{\theta}'$ is evaluated, where F is the Jacobian matrix and $\delta \boldsymbol{\theta}'$ contains $N - M$ non-redundant entries. To remove any global rotation, we fix the first motor to be stationary by substituting $\boldsymbol{\theta}' = \begin{bmatrix} \mathbf{0_{N-1}}^T \\ I_{N-1} \end{bmatrix} \boldsymbol{\theta}''$, where $\boldsymbol{\theta}''$ contains orientations 1 to $N - M - 1$, resulting in $\delta \dot{\boldsymbol{\theta}}'' = F' \delta \boldsymbol{\theta}''$. The eigenvalue decomposition of F' yields stable, unstable and neutral (floppy) folding modes corresponding to negative, positive and zero eigenvalues. However, the motion defined by an eigenvector of F' may be geometrically forbidden. Therefore, to identify feasible eigenvectors, we calculate the kinematic space of a loop, which is of rank $N - M - 2$ (which includes the global rotation mode). The kinematic matrix is given by $V_{kinematic} = V \mathcal{N}$, where column vectors are the basis vectors. V contains the right-singular vectors

of $\begin{bmatrix} B & 0_N \\ 0_N & B \end{bmatrix} \begin{bmatrix} H_x D \\ H_y D \end{bmatrix}$ excluding its null space and $\mathcal{N}$ is the null space of SVD of

$$\begin{bmatrix} 1_N{}^T & 0_N{}^T \\ 0_N{}^T & 1_N{}^T \end{bmatrix} \begin{bmatrix} H_x D \\ H_y D \end{bmatrix} V.$$

3.11 Supplementary information

3.11.1 Kilobot algorithm

Algorithm: Loop method of the kilobot microcontroller

```
void spinup_motors_custom(){

    set_motors(255, 255);

    delay(d);
}

void loop(){

    double noise = 200;

    spinup_motors_custom(8);

    double l = rand_soft()*noise/255;

    set_motors(kilo_turn_left, 0);

    delay(l);

    spinup_motors_custom(8);

    double r = rand_soft()* noise/255;

    set_motors(0, kilo_turn_right);

    delay(r);
}
```

Linking kilobots

Smaller steric effect (Narrow taper)

Larger steric effect (Wide taper)
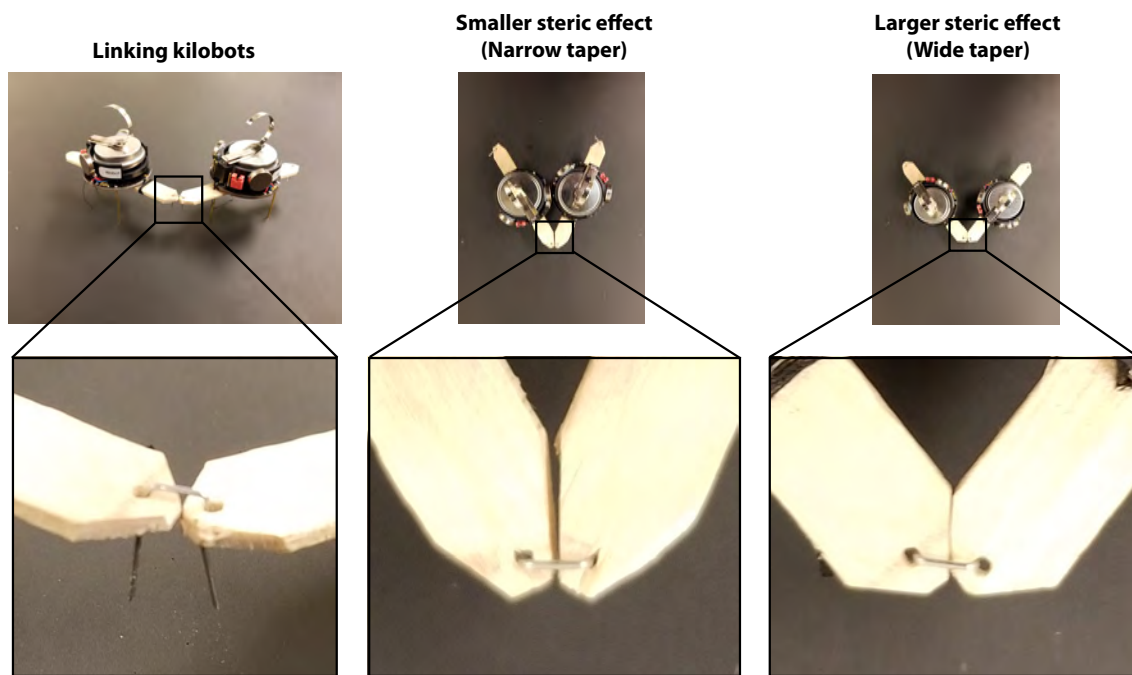
Fig. 3.S1: Kilobot motor design. Left image shows two kilobots, each attached with a popsicle stick, linked using a metal pin forming a hinge. Center and right images show tuning steric hindrance between adjacent motors by tapering the ends. Wider the taper, larger is the minimum fold angle between the motors.

Fig. 3.S2: Design parameters of loops. Complete design parameters of simulated shapes in shown in Fig. 3.3. All shapes are simulated at $\overline{T} = 0.1$ except for the one shown at $\overline{T} = 0.4$. The force unit is f_0 as mentioned in the Materials and methods. The arrows with along a sub-segment indicate and mention the total propulsion force on that sub-segment. The rising color opacity indicates linearly increasing magnitude of propulsion along the direction of the force. The loops contained in a dotted box have identical design parameters except the one mentioned for both the loops.

Fig. 3.S3: Design parameters of composites. Complete design parameters of the three composites–letter *M*, gripper, and pacman.
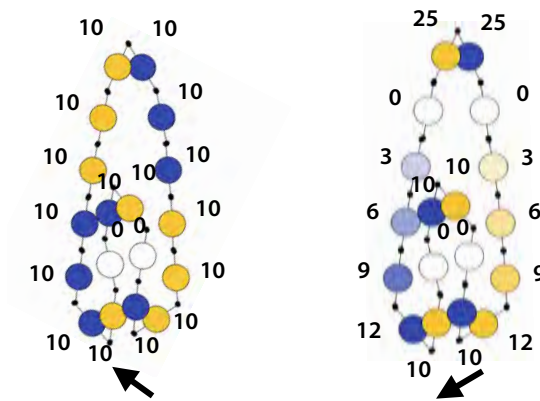
Fig. 3.S4: Design parameters of loops in Fig. 3.4.
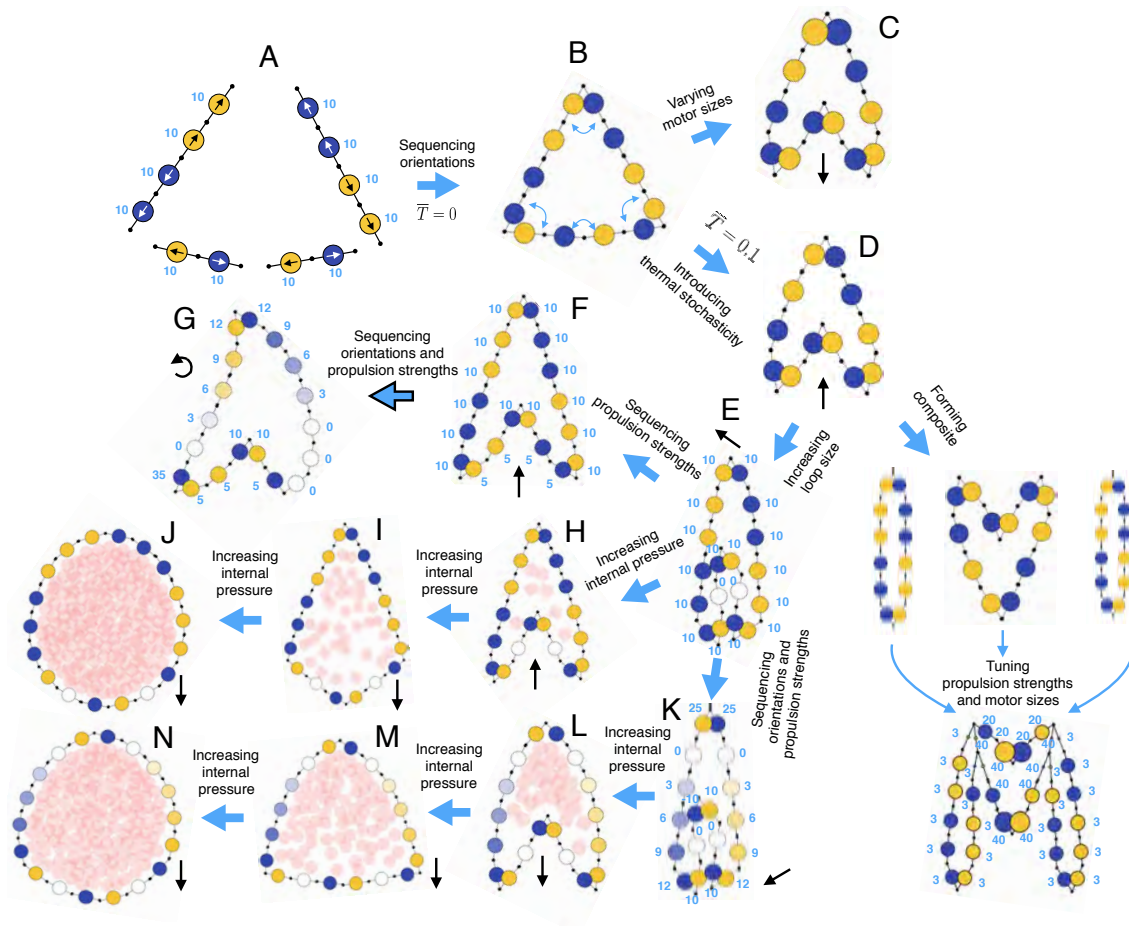
Fig. 3.S5: Tuning of the arrowhead shape using the design space. Shown is how parameter tuning of the loop tunes the folded arrowhead shape.
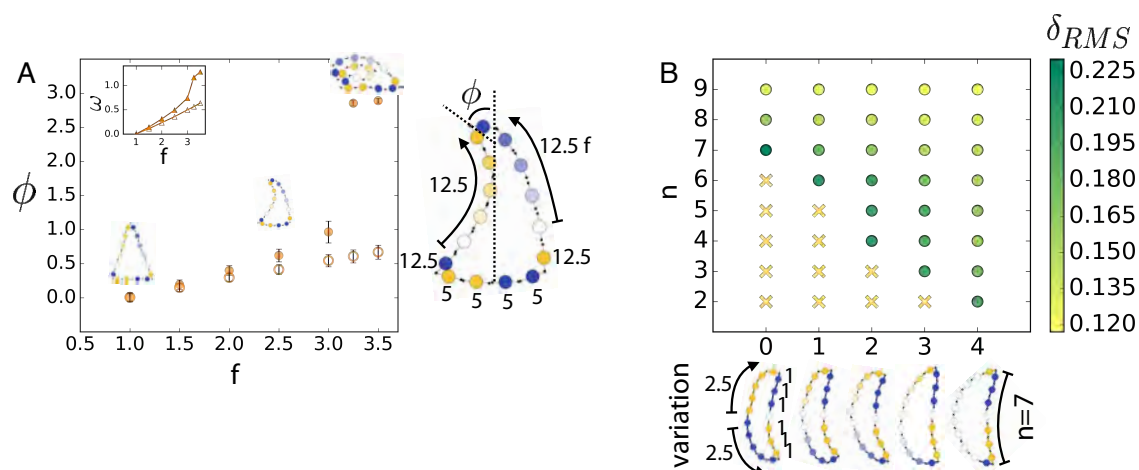
Fig. 3.S6: Plots studying curving of example shapes. (A) Plot showing how curving (measured using ϕ) of the triangle shape increases with the sub-segment force, measured in multiple of 12.5 using f. Filled and empty markers correspond to simulations with steric hindrance turned on and off respectively between the motors. The difference between the two cases for higher values of f demonstrate significance of steric hindrance. The inset shows plot of rotation ω vs f for the same set of simulations. (B) Heatmap of fluctuations, δ_{RMS}, for different curvature of the segment and different variation of propulsion magnitude along the force direction. The are two segments in the loop. The length of the right (shorter) segment determines the curvature of the left (longer) segment. The net propulsion on the sub-segments of the left segment is set to $2.5\ f_0$, while the propulsion magnitude along them increases according to five variations: 0 (1, 1, 1, 1, 1); 1 (0, 0.75, 1.5, 1.75, 2); 2 (0.0, 0.5, 1, 1.5, 2); 3 (0.0, 0.25, 0.5, 1.25, 2); and 4 (0, 0, 0, 0, 1). The crosses mark statepoints that folds into mechanically trapped states due to high fluctuations. The plot shows that stability of curved sub-segments increases with propulsion variations of higher gradient. The variation used in the main text is number 2.
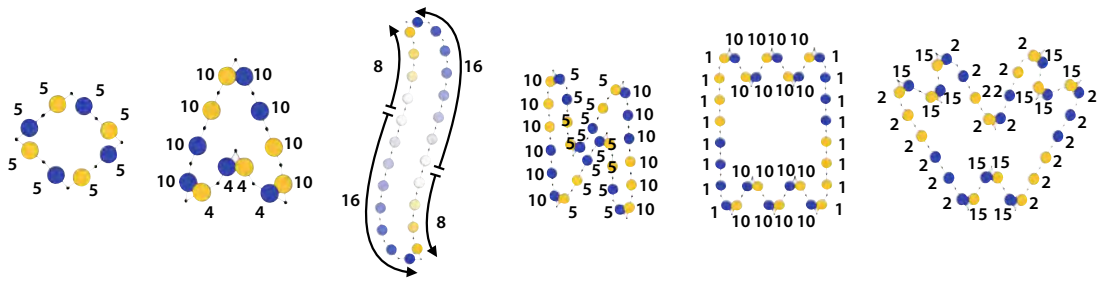
Fig. 3.S7: Design parameters of loops in Fig. 3.7. The shown forces are normalized to set the mean at $6\ f_0$.
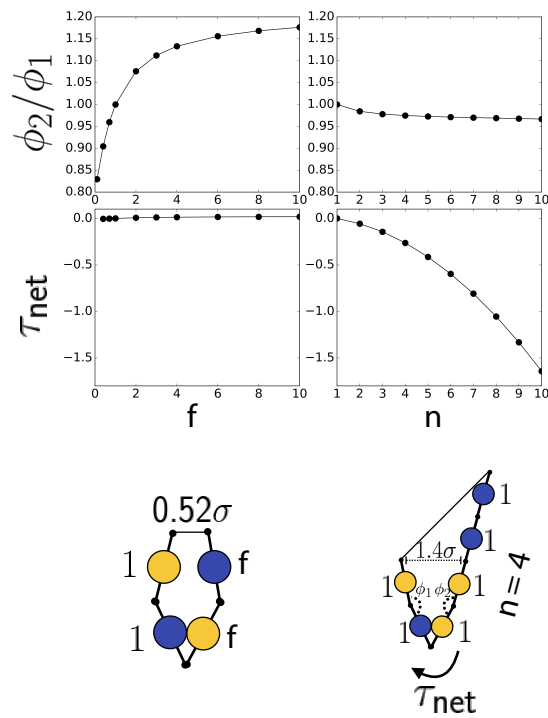
Fig. 3.S8: Additional plots for the two-segment system. Similar to plots in Fig. 3.6F but measuring net torque, τ_{net}, and ratio of angles, ϕ_2/ϕ_1, for different motor propulsion force, f, and length, n, of the segment as shown.

CHAPTER IV

Muscle-Inspired Flexible Mechanical Logic Architecture for Miniature Robotics

This chapter is adopted from a publication authored by M. Agrawal, and S.C. Glotzer that is currently under preparation.

4.1 Introduction

Colloidal scale (10nm-100μ) robots programmed to morph into different configurations dictated by its environment or external user can impact industries like healthcare[1], energy[4], defense[2] and consumer products[3]. Such robots will respond to multiple stimuli such as heat, light, sound, chemical environment, electric and magnetic fields. However, constraints on materials that can be used, need for biocompatibility in case of biomedical applications, and presence of stochastic forces make it difficult to build such robots using conventional electronic batteries, sensors and actuators[11, 65, 3]. An alternate approach is to use stimuli responsive polymers (SRPs)–materials that expand or contract in response to the stimuli–that behave like *artificial muscles*[17, 18, 19]. The advantage is that SRPs act both as the sensor and the actuator for stimuli that themselves act as the power source and the communication agent, thus integrating the electronic counterparts. There

76

are plethora of different varieties and designs developed for SRPs motivating their application[17, 18, 20, 19]. Currently, the robots made using these materials lack logic and therefore, are limited to simple functions[17, 18, 19]. Further, we also want to be able to integrate multiple kinds of SRPs into a single robot design. Implementing this while avoiding issues relating to materials constraints and ensuring integration with muscles requires a material agnostic approach. Such an approach is mechanical computing. It uses mechanical structures that owing to their geometric constraints perform logic operations analogous to digital logic gates. Incorporating logic within a robotic system allows to actuate 2^N arbitrary robot configurations by transducing combinations of N number of muscles. This property is of significant importance for colloidal scale robots that are controlled using handful number of triggers (stimuli).

Existing designs of mechanical logic[75, 24, 76] are focused primarily on the computation aspect and therefore, they use translation motion for signaling instead of muscle-like actuation, relevant for the colloidal robots. Their applicability at colloidal scale is further limited due to either cumbersome design[75, 24]; use of sliding and colliding parts[18]; or dependence on bi-stable mechanism[24], which scales the actuation energy barrier of the logic circuit as it increases in complexity. To solve these challenges, here we present a logic architecture consisting of compact gate mechanisms that use muscle actuation as input-output signals and are free from bi-stable, sliding and colliding parts. Besides logic gates, we also provide a connector design, which is a floppy chain that transmits mechanical signal between gates. As a result, our mechanical circuits are flexible. Further motivation of developing such mechanical architectures are advancements in self-assembly[21, 22], 3D printing[24, 19] and

MEMS fabrication techniques[25, 26] providing ways to manufacture precise structures at colloidal scale. Table 4.1 provides existing technologies for fabricating and actuating complex miniature structures and corresponding quantities.

4.2 Gate design

Our gate is a 3D structure using link and hinge mechanism. The links are 2D rigid bars with either edge or vertex hinges among them. The input are muscles that expand or contract under stimulus but are stiff otherwise. Fig. 4.1A shows the schematic of the universal logic gate (NAND gate). Here, the two input muscles (blue and yellow) contract when actuated defining the binary states 0 (rest) and 1 (contracted). There are eight hinges in total in any gate structure excluding the ones required to attach inputs and output. The motion of our gates is continuous and in principle there is no potential energy barrier to move between the states. In Fig. 4.1B, we demonstrate a simple 3D printed robot with a single degree of freedom that flaps its tail using the NAND gate as its brain. The input states are set to 0 or 1 using locks as shown. The angle of the tail element with respect to the front element decreases when the gate input is (1,1). Hence, the tail flapping occurs only when one of the inputs is set to 1 while the other is switched between 0 and 1. The gate design uses three lever mechanisms, two at the input ends and one at the output end (see Fig. 4.1A). The lever mechanism is used to transmit signal between different rest lengths of input and output, amplify or reduce signal, and invert the signal from contraction to expansion and vice versa. These signal conversions also allow implementing NOT gate and integrating it directly within other gates, as in the case of our NAND gate.

78
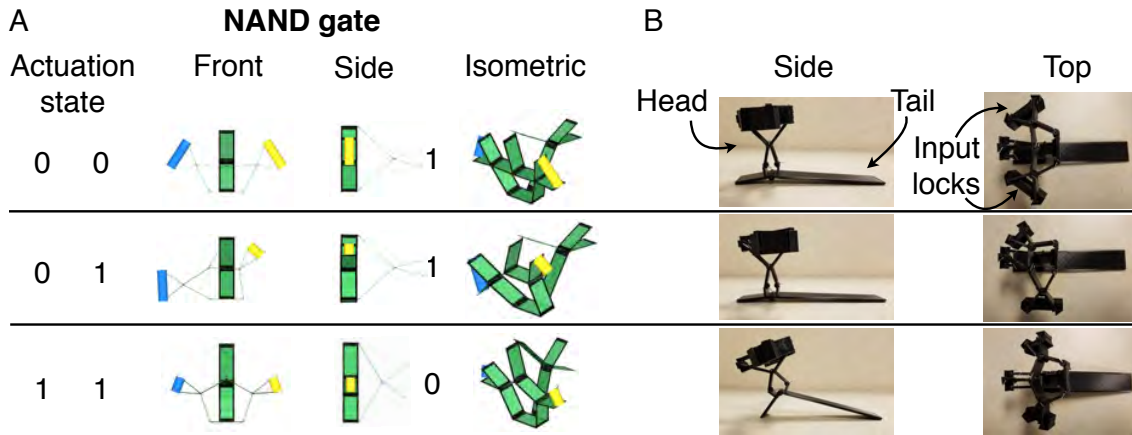
Fig. 4.1: NAND gate design and robot demonstration. (A) NAND gate configuration for different inputs. The expanded (σ) and contracted ($\sigma/2$) states of the muscles (red,blue) define the 0-1 input states of the gate. (B) Centimeter scale 3D printed model of the NAND gate. The input lock is used to set the input state of the model. (C) A rudimentary robot demonstration, where the NAND gate act as head that manipulates the tail configuration based on the given input.

Table 4.1: Available technology to enable muscle-inspired transduction

| Muscle length scale | Structure fabrication | Muscle | | | | Hinge | | |
		Type	Muscle strength	Actuation stimuli	Actuation time scale	Type	Hinge strength	*Thermal energy over hinge strength ($k_BT/k\sigma^2$)
10nm	DNA linking[23]	DNA[14]	Force to pull apart dsDNA $\sim$15pN[14]	ssDNA[14]	$\sim$13s[14]	ssDNA[14]	$\sim$15pN	10^{-2}
1μm	Self-assembly[77], Lithography[78], Non-contact 3D printing[28]	Stimuli-responsiv polymer[1 79, 80]	Modulus 100kPa-200MPa[17]	Temperature, pH, electricity, light, and chemicals[81, 17, 80, 79]	Seconds to hours depending on the scale and material[79, 81]	multiple ssDNA[82, 83]	Binding energy per DNA bond 6k_BT[83]	10^{-4}
100μm	Lithography[78], 3D printing[84]					Polymer flexure[24]	–	–
		Shape-memory alloy[85]	Modulus of metals >1GPa	Temperature[85], magnetic field[17]	$\sim$10s[85]	Rotary hinge[86]	Modulus for steel >1GPa	10^{-16}

*Materials and Methods provide estimation details.

Fig. 4.2A shows the schematic of two lever designs. Similarly, colored elements are in the same rigid body. Therefore, by design, the lever on the left inverts the sign of the signal whereas the one of the left does not. These two designs are represented by *open circle* and *crossed circle* hinges as shown. The design variables for a lever are θ_1, θ_2, l_1 and l_2. These variables can be calculated using Eq. 1-5 given the following parameters (shown in Fig. 4.1A): (l_{in}, l_{out}), the rest lengths of input and output; $(\Delta l_{in}, \Delta l_{out})$, the input and output signals; and l, distance between the input and output in the rest state.

$$l_1 \sin \theta_1 - l_{in} = 0 \tag{4.1}$$

$$l_2 \sin \theta_2 - l_{out} = 0 \tag{4.2}$$

$$l_1 \sin(\theta_1 + \Delta\theta) - (l_{in} + \Delta l_{in})/2 = 0 \tag{4.3}$$

$$l_2 \sin(\theta_2 + sign\ \Delta\theta) - (l_{out} + \Delta l_{out})/2 = 0 \tag{4.4}$$

$$l_1 \cos \theta_1 + l_2 \cos \theta_2 - l = 0, \tag{4.5}$$

where $sign$ is -1 for the open circle lever and 1 for the crossed circle lever. Using these equations levers can be designed for any rest lengths of input and output without losing the gate functionality. This feature is important when connecting different gates to form a circuit. Since the lever mechanisms are only used for signal conversion, the logic is implemented via the *logic core*. The logic core consists of a horizontal (ab) and a vertical (de) element as shown in Fig. 4.2B for the NAND gate. The workings of this logic core can be understood by studying its geometry. Sides ad and bd are the inputs and ce is the output of the logic core. These inputs and output actuate by extending their lengths. The constraints on the logic core are

that ab and ce moves in the same plane and point e moves along the perpendicular bisector of ab. These constraints are satisfied by the input and output levers respectively. In Fig. 4.2C, expanding muscles are used as inputs of the logic core. The three diagrams show configurations of the logic core for input states (0,0), (0,1) and (1,1). The output state is 1 only for input (1,1), hence, implementing the AND logic. In Fig. 4.2C, when the yellow muscle expands, ad and de rotate to a new location for d such that e remains at the same location. Only when the blue muscle is also expanded that e moves up to a new location resulting in the actuated state (state 1) of the logic core output. The structure of the core logic is determined by lengths σ and x, and angle ϕ. Given the values of σ, x, and Δ_{in}, ϕ and auxiliary variables γs and ζ (shown in Fig. 4.2C) can be calculated using Eq. 6-11.

$$\sin\phi - \cos\gamma_1 - (x/\sigma)\sin\gamma_3 = 0 \qquad (4.6)$$

$$\sin\gamma_1 + (x/\sigma)\cos\gamma_3 - x/\sigma - \cos\phi = 0 \qquad (4.7)$$

$$\cos\gamma_1 + (1 + \Delta_{in}/\sigma)\cos\gamma_2 - 2\sin\phi = 0 \qquad (4.8)$$

$$\sin\gamma_1 - (1 + \Delta_{in}/\sigma)\sin\gamma_2 = 0 \qquad (4.9)$$

$$x/\sigma + (1 + \Delta_{in}/\sigma)\cos(\zeta/2) - \cos\phi - x/\sigma - \Delta_{out} = 0 \qquad (4.10)$$

$$1 - 2\sin^2\phi/(1 + \Delta_{in}/\sigma)^2 - \cos\zeta = 0. \qquad (4.11)$$

Different gates may use the same logic core because the gate function is decided by the input-output lever designs. Fig. 4.2D shows examples of such gates (in rest states). When a gate input uses contracting muscle (For instance, NAND in Fig. 4.2B and AND in Fig. 4.2D), the open circle lever is used to map the contracted state (state 1) of the muscle to the expanded state (state 1) of the logic core. Naturally, the rest states of the muscle and the logic core also map to each other. Here, this

lever inverts the signal without inverting the state. Similarly, for the input that uses expanding muscle (AND-2 in Fig. 4.2D), crossed circle lever is used to map 0 to 0 and 1 to 1 states of the muscle and the logic core. The output lever type depends on how the states are defined. Here, we consistently define contracted state as state 1 unless otherwise specified. Hence, the open circle levers are used for the output of the AND gates (Fig. 4.2D) converting the signal so as to map 0 to 0 and 1 to 1 states of the logic core output and the gate output and to map the corresponding rest lengths. The NAND gate (Fig. 4.2B) uses the crossed circle lever for the output. This lever maps state (0,1) of the logic core output to state (1,0) of the gate output and hence, act as a NOT gate by performing state inversion. The OR Gate (Fig. 4.2D) is formed by integrating the NOT gate in both input and output levers of the AND gate while the NOR gate integrates the NOT gate only in inputs.

4.3 Analysis

To test the stability and response at colloidal scale we simulate the gates using Brownian dynamics (see Materials and Methods). The simulation analysis of the robot in Fig. 4.1B is presented in Fig. 4.3. Fig. 4.3A plots the root-mean-square fluctuation, $\Delta\alpha$, of the angle, α, between head and tail of the robot at input state (1,1) of the NAND gate with respect to the ratio of k_BT over k_0. The steady rise of $\Delta\alpha$ suggests mechanical stability of the configuration, which is also evident in the simulations. Fig. 4.3B plots the temporal variation of α for three different frequencies determined by the parameter f. The root-mean-square deviation of the α response (solid line) from ideal response (dotted line) is 3.6%, 4.5% and 17% for $f = 1$, 10 and 100 respectively.
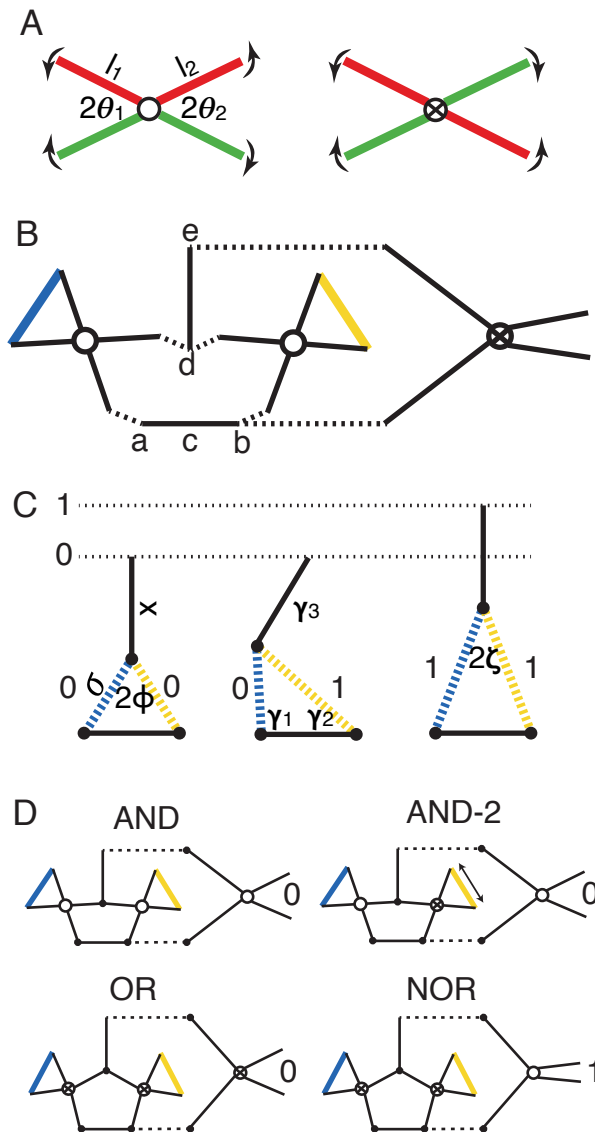
Fig. 4.2: Gate geometry and building different gates. (A) Types of lever designs and their representations for signal transmission (open circle hinge) and inversion (crossed circle hinge). The red and green colors represent lines in the same rigid body. (B) The three levers of the NAND gate are detached to reveal the *logic core* or *transistor* (consists of lines ab and de). The dotted black lines draw connections between the levers and the transistor. For visualization, the output lever is rotated to lie the plane. The NAND muscles contract to actuate. (C) Configurations of the transistor for different actuation states of its two inputs. Dashed blue and yellow lines represent expanding muscles of the transistor (D) Different logic gates formed by combining the transistor with levers at inputs and output. Muscles contract to actuate except the yellow muscle of the gate AND-2 that expands as shown by the arrow. Black solid circles are circular hinges. The lines are drawn to scale.
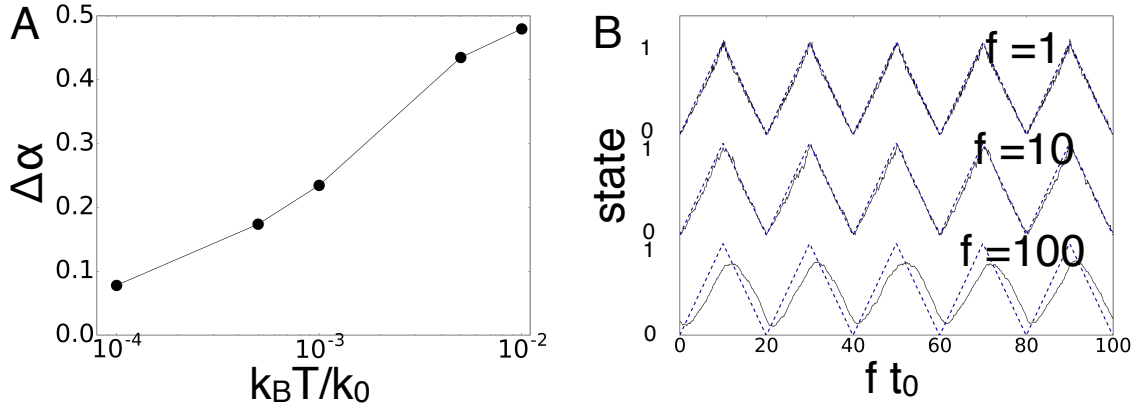
Fig. 4.3: Stochasticity and relaxation. (A) Plot of fluctuation, $\Delta\alpha$, calculated as the standard deviation of α, where α is the angle between the head and tail slabs of the robot in Fig. 4.1B measured in simulations. Calculation is performed using 4000 frames over the duration of $400\ t_0$. (B) Time response (solid line) of α varying between states 0 and 1 for the input states (0,0) and (1,1) for the robot for different frequencies of the actuation cycle of the input (dotted line). $k_B T$ is set to $10^{-4} k_0\ \sigma^2$.

4.4 Building mechanical circuits

Since the input-output signals and their rest lengths of different gates are compatible, output of one gate can be directly connected to the input of the other. However, signal transmission and split may be required for building complex circuits. Therefore, we propose a connector design that is a flexible chain that besides allowing signal transmission and split, can also rotate the signal axis. A unit of the connector chain is shown in Fig. 4.4. It consists of two half units with four slabs each. The half unit rotates the input signal to its perpendicular axis and invert the signal. The full unit transmits the signal but has a floppy mode in this perpendicular axis resulting in a flexible connection. Signals can be split by branching connector chains.

We demonstrate building a complex circuit and using it for robotics (Fig. 4.5) by
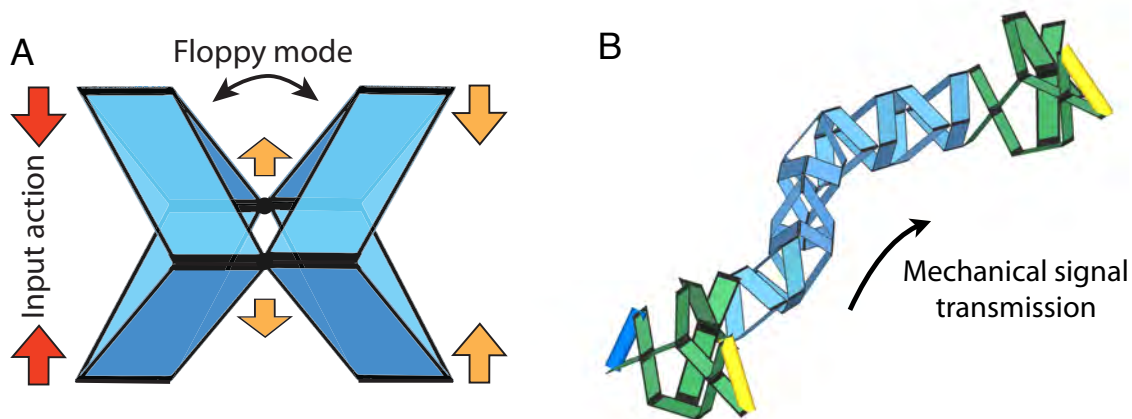
Fig. 4.4: Connector design. (A) A connector unit that transfers the signal to the same axis with a floppy mode in the middle. Half unit of the connector, consisting of four bars, inverts the actuation signal and rotates it to its perpendicular axis. The broader black lines are hinges. (B) Simulation snapshot showing transmission of mechanical signal from the output of the first AND gate to the input of the second. The blue and yellow muscles expand to actuate.

simulating morphing of a skeleton chain into four Tetris shapes using two muscle types. Since the Tetris shapes require 2D folding, we use the unit in Fig. 4.5A to make a skeleton chain. The mechanical circuit connects to the skeleton unit to bend it up or down. In principle, any robot skeleton is compatible with our architecture. In Fig. 4.S.., we provide a skeleton chain unit that can also twist besides bending. To achieve the Tetris shapes, we use the circuit shown in Fig. 4.5B using digital logic gate symbols. Fig. 4.5C shows folded Tetris shapes for different input states and a complete configuration for input state (0,1).

4.5 Discussion

Research in mechanical logic is traditionally motivated by either the importance in fundamental understanding of the relation between logic and physical structure[87, 41, 42] or due to their potential in building computing systems resilient to extreme
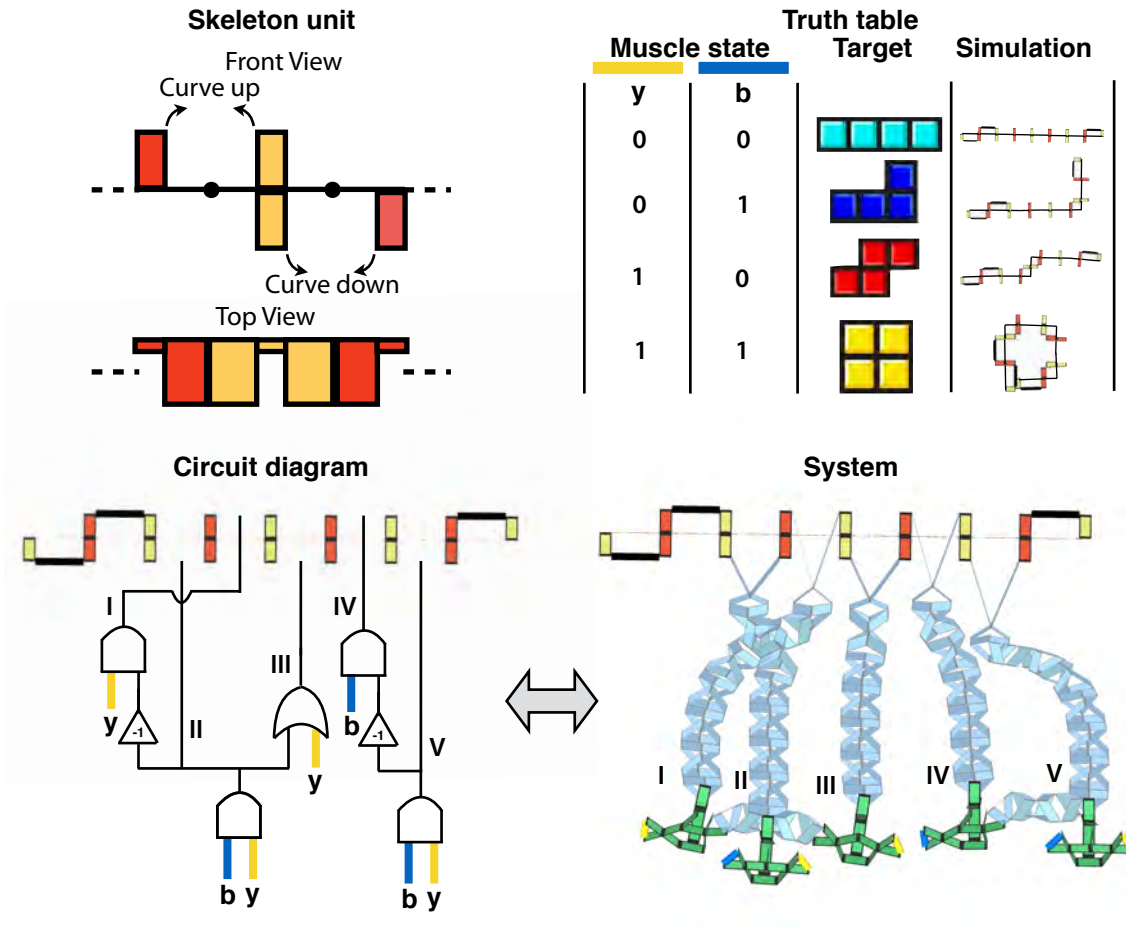
Fig. 4.5: Transduction of Tetris shapes. Top-left is the skeleton unit of the robot skeleton contains the degrees of freedom to bend upward and downward. Top-right is the truth table with snapshots of 4 Tetris shapes folded in simulations for different actuation inputs of yellow (y) and blue (b) muscles. Bottom is the logic circuit (digital representation on the left) connected to the skeleton comprised of four units. Bottom-right is the corresponding (C) (Top) (Bottom) Snapshot of the simulation at equilibrium for the input (0,1). For simulations of Tetris shapes, $k_B T = 10^{-5} k_0 \ \sigma^2$.

conditions of heat, pressure and radiation. We foresee employing mechanical logic in miniature scale robotics because of three reasons:

1) Mechanical logic is inherently material agnostic and hence, the design can be translated to any application context. 2) Development of materials like SRPs that actuate in response to variety of stimuli. These materials provide transduction route alternative to electronics at colloidal scale. 3) Development of fabrication techniques that can make complex structure at small scales. For example, RNA strands can attach specific blocks while allowing hinge motion between them[22]. MEMS fabrication technique can make rotary hinges between specific blocks with great precision[25]. 3D printing can continuously print blocks and the flexure mechanism between them under 100 microns[24, 88].

The architecture we designed to perform combinatorial logic consists mechanical gates to perform binary logic computation and connectors to transmit mechanical signals. The architecture uses only link (rigid bars) and hinge mechanisms and is free from sliding or colliding parts. The gate mechanism continuously transition between configurations to set the two output states in a single mode and hence, do not possess any transition energy barrier. The architecture is stable under stochastic forces relevant for the colloidal scales. The particular novelties we implemented are: signal transmission uses muscle like linear actuation; gate design is compact, uses 8 bars and 8 hinges for any gate, resulting in no requirement of a separate NOT gate; the optional connector mechanism possesses floppy modes that makes the connector flexible.

The major criticisms of mechanical computers are that they are slow and prone to wear and tear. However, they also equip conventional robotics with alternative

approaches to incorporate smartness. Using our approach, organic and biomorphic robots can be built. Material agnosticism allows usage of biocompatible raw materials. Our mechanical circuit can be embedded in a polymer matrix yielding a soft computer. Our mechanical logic is advantageous for building robotic systems that require lower complexity relative to electronic logic circuits but have constraints over raw material and activation environment. Additionally, use of flexure hinge mechanism and careful incorporation of bi-stable elements can enhance precision, response rate and lifetime of these structures. These properties can be further improved by design optimization for the application in context.

Following are some of the envisioned applications that can use our design: 1) *Smart medicine:* Nanoscale robotic carriers morph in response to chemical signatures of damaged tissues to release drugs and repair the site.

2) *Smart textile:* Fabric embedding network of tiny mechanical actuators and computers that change its microstructure tuning optical, electronic, and mechanical properties in response to the environment.

3) *Space rovers:* Mechanical computers can survive extreme conditions and actuation can directly be powered by its environment and hence, can be used in robots for planetary exploration.

4) *Non-invasive surgical robots:* Mechanical circuit mounted on tentacle in the order of 100 microns can be injected in human body. Magnetic field can navigate and orient the tentacle and lasers can be used to activate specific input muscles. This in-turn will actuate the specific configuration of the tentacle to perform surgical operations.

5) *Contaminant capture:* Swarm of sub-micron scale robots can detect contami-

nants with certain chemical signatures and then morph in response to contain and remove those. Such mechanism can be used in chemical plants, preventive drugs, oil spills, and pipelines.

4.6 Conclusion

We proposed a design architecture to compute combinatorial logic for colloidal scale robotics. The architecture consists mechanical logic gates that use linear actuation (expansion-contraction) as input and output signals. The signal can be transmitted between the gates using flexible connectors. A simple 3D printed robot consisting a NAND gate controlling a single degree-of-freedom is demonstrated. We analyze the geometry of the gate mechanism and discuss building various gates. We verify the stability and response of the gate mechanism at colloidal scale using Brownian dynamics simulation. Finally, a complete robot consisting a mechanical circuit connected to a skeleton chain is simulated to demonstrate the applicability of our design for robotics. The skeleton of this robot is folded into four different Tetris shapes using two input muscle types.

4.7 Materials and Methods

4.7.1 Design parameters

The design parameter σ is defined as the length of the input core. For our gate designs, the length of all input muscles is set to σ and the width of all the bars is 0.5σ. The parameter values that the decide input lever dimensions (via Eq. 1-5) are $(\Delta_{in}, \Delta_{out})=(\pm 0.5\sigma, 0.5\sigma)$ and $l = 1.5\sigma$, and that decide the output lever dimensions are $(\Delta l_{in}, \Delta l_{out})=(\Delta_{out}, \pm 0.5\sigma)$ and $l = 2\sigma$. The negative or positive sign depends

on the gate and the signal type–expansion or contraction. The parameters for the logic core are $x/\sigma = 2$ and $\Delta_{in} = 0.5\sigma$.

4.7.2 Estimation of $k_B T/k\sigma^2$ in Table 4.1

For 10nm: k_BT=4.1pN·nm. Applying force of 15pN for a couple of nanometers to break the DNA bond is equivalent to the energy of 15pN·nm. Assuming ~10 number of bonds on the 10nm wide hinge, $k_B T/k\sigma^2 \approx 4.1/15 \cdot 10 \sim 10^{-2}$.

For 1μm: Assuming ~10^3 number of DNA bonds on a micron wide hinge gives the net binding energy of ~$6 \cdot 10^3$ k_BT. Thus, $k_B T/k\sigma^2 \approx 1/6000 \sim 10^{-4}$.

For 100μm: Assuming hinge metal has strength of ~1GPa. Energy required to pull apart a hinge of area $(\sim 100\mu m)^2$ for a micron distance is $\sim 10^9 N/m^2 \cdot 10^{-8} m^2 \cdot 10^{-6} m = 10^{-5} N \cdot m$. Thus, $k_B T/k\sigma^2 \approx 4.1 \cdot 10^{-21} N \cdot m/10^{-5} N \cdot m \sim 10^{-16}$.

4.7.3 Experiment

Physical parts are 3D printed using Monoprice Maker Ultimate. Rotary joint design is used for hinges. Selective bars are trimmed to permit rotation at these hinges. Approximately 0.2mm clearance is left between consecutive knuckles.

4.7.4 Simulation

The width and thickness of all bars is 0.5σ and 0.01σ respectively. These are simulated in three dimensions using the simulation toolkit HOOMD-blue (v2.6) [59, 60, 61, 71, 72]. The dynamics of each bar i is simulated using the Brownian equation of motion[62].

$$\dot{\boldsymbol{r}}_i = \frac{1}{\gamma}\boldsymbol{F}_i + \sqrt{2\frac{k_B T}{\gamma}}\,\boldsymbol{\eta}(t) \tag{4.12}$$

$$\dot{\theta}_i = \tau_i/\gamma_r, \tag{4.13}$$

where $\boldsymbol{r}_i$ and θ_i are the position and orientation of bar i respectively. $\boldsymbol{F}_i$ and τ_i are the net force and torque on i due to volume exclusion interactions and harmonic bonds. The edge-edge hinge is modeled by two harmonic bonds at either ends with harmonic coefficient k_0 and equilibrium length zero. Since the mechanical computation does not require particle collision, volume exclusion is only required to prevent large structural overlaps. Hence, we apply isotropic volume exclusion between the centers of the bars via the Weeks-Chandler-Andersen potential, $U_{WCA}(r) = 4\epsilon \left[(2r_0/r)^{12} - (2r_0/r)^6) \right] + \epsilon$, for $r < 2r_0$, and $U_{WCA}(r) = 0$ otherwise[63], where r is the distance between the centers of the bars and $r_0 = 0.1\sigma$. Parameter ϵ determines the strength of the potential and is set as $\epsilon = 10^{-4}k_0\,\sigma$ for our system. The muscles are modeled as harmonic bonds with strength k_0 and are actuated by varying their equilibrium lengths. Thermal energy $k_B T = 10^{-5}k_0\,\sigma^2$ unless specified otherwise, and $\boldsymbol{\eta}(t)$ is unit-variance Gaussian white noise. γ_r is the rotational drag coefficient and is set equal to the translational drag coefficient, γ. The rotational noise in a particle orientation arises from the translational diffusion of the particles bonded to it. Time is measured in units of $t_0 = \gamma/(10^{-3}k_0)$. The translation of the gates in the circuit for the Tetris shapes is intentionally restricted in simulation to prevent them from diffusing away.

CHAPTER V

Conclusion and Outlook

5.1 Conclusion

The colloidal swarms encode information in the interaction of its agents. The agents are all identical or are of a finite number of types. The interaction can be as complex as possible. Therefore, the colloidal swarms are best to tune the mechanical and transport properties of materials through emergence. The property change is triggered using external stimuli which changes the interaction protocol of the agents. System 1 presented here demonstrates this idea using a simple system where propulsion force on one kind of colloids is switched on when and as long as they are in contact with the other kind of colloids. Tuning the composition and propulsion strength changes the material phase among crystals, gel, and clusters, and varies the density fluctuation property.

In morphological control, the output function is encoded in the structure of the system, which is a connected structure of similar or different objects. Here, we present such a system using only active particles. The particles are chained end-to-end in a loop such that their propulsion is tangential to the loop. The particles can be arranged to direct propulsion either clockwise or anticlockwise along the loop.

The sequence of propulsion directions along with their strengths and other system parameters encodes the folding of the loop into a unique shape and its subsequent motion. The morphologically controlled systems allow creating finite colloidal machines using active particles. The reconfiguration and navigation of these systems will be controlled by external stimuli.

Morphological computation refers to performing logic operations and information storage. We developed a mechanical architecture for logic operations in context to colloidal robotics. Specifically, our architecture uses SRPs as input signals and also as actuators to power manipulation of end-effectors.

5.2 Outlook

The computational systems presented here are devoid of any external forces or biases that will be present in experimental systems. Further investigation in these areas will be required to fully realize applications of these systems. Below are the mentions of different aspects of each project that are interesting and useful for future studies.

System 1: Contact-triggered active particles (CAPs)

This work assumes the simplest model for triggering activity, i.e., propulsion force is triggered as soon as CAPs come in a certain distance range of the passive particles. However, for experimental systems, the activation may be more gradual and will depend on the particular physical chemistry. Further, attractive or repulsive interactions between CAPs and between passives might also be present. These factors may affect the location or presence of the observed phases.

Chapter 2 conclusion mentions directions for developing the theoretical model for

CAPs. The potential goal of theoretical models can be to understand the coupling and competition between entropy and active force in the mixture of CAPs and passives. This is tricky for the CAPs system because the amount of activity depends on the number of CAP-passive contacts. Hence, theory models will provide insights into thermodynamic factors behind the formation of different phases.

The propulsion of particles will result in solvent hydrodynamics which will incorporate long-range particle interactions and inertial effects into the system. The contribution of hydrodynamics will depend on the scale of the particles and the strength of their propulsion forces relative to the solvent viscosity. Since the system is 2D, it may also be possible to deviate the reaction force of propulsion in the 3rd dimension.

One of the practical implementations is to embed CAPs into a 2D sheet/membrane. The surface of the sheet can be a gateway for the energy source–light, heat, chemical fuel. The sheet will change its mechanical properties depending on the phase. The phase is governed primarily by the system composition. It will be interesting to find practical ways to tune this composition on-the-fly. For instance, particles harnessing different frequencies of light can be used. The composition will be determined by the number of frequencies used. Since the sheet can fold and bend, topological effects on the phase formation are also important. Switching between different phases will also require investigation. For instance, switching from cluster phase to crystal is easier than vice-versa because the cluster phase is kinetically arrested and is probably achieved only when starting from a homogeneous fluid state.

The presence of grain boundaries and vibrant dynamics may limit the system's usage for photonic applications. However, the widely varying system dynamics can

be potentially used to tune transport properties on-the-fly. Experimental studies will be required to demonstrate and map this idea for tuning viscosity, diffusivity, and thermal coefficients.

The practical systems may contain external mechanical factors such as walls, baffles, obstructions, and internal factors such as polydispersity. It is found that self-propelling particles tend to accumulate near the walls[7]. However, CAPs do not necessarily follow this trend. Experiments and simulations can focus on investigating and exploiting such external and internal factors.

System 2: Chain loops of active particles

Using polymers or DNA to chain the particles may introduce bending energy and hinge tolerance, which is not investigated in this work. Non-zero bending energy may limit the formation of high curvature regions, thereby, increasing the formation of smooth contours. It may also reduce the mechanical trapping during folding by preventing large deformations of the loops. Hinge tolerance includes floppy modes reducing the shape integrity. The experiments using kilobots contain hinge tolerance. Their success does provide some evidence that the design strategy is sufficiently robust but more comprehensive studies on this front are required.

It will be useful to carry out comprehensive investigations on the effects of internal factors such as noise and bias in the propulsion direction, and external factors such as folding of the loop while being latched, robustness to collisions with walls and other loops. The disruptive effects of these factors will depend on the loop complexity and hence, better strategies will be required for tuning the design space.

Current work provides a heuristic approach for the inverse design of the loops. However, a dynamical continuum model will be more useful for rational inverse de-

sign. In the current design, loops are sensitive to the initial configuration and show decreasing stability as the loop complexity increases. The theoretical model provided in this work is able to quantify the loop's stability. In the future, it can be extended to identify novel loop designs or optimize the loops designed using the given heuristics.

It will be interesting to extend the 2D nature of loops into 3D. There are two ways this can be done. The first and the relatively easier approach is when the loop topology is retained in 2D but the loop's plane exists in 3D. This means that the normal vectors of the circular hinges are free to point in any direction. This will introduce a new sequence parameter in the design space to optimize. Experimental realization of such circular hinges will be tricky and may require novel fabrication methods. The second approach is to connect active particles to form a sphere rather than a loop. This is a harder design problem because there are more options for connections between particles and their propulsion directions. The practical advantage of using this approach over the first one is also not apparent.

System 3: Mechanical logic architecture.

The hinge tolerance of the gates and the connector cause a decline in the signal strength that limits its practical utility. This tolerance can be improved by using live hinges, or tighter joints in the first place. The signal transmission can be maintained by using bistable elements, allowing to pin the signal to one of the binary states as it is propagating through the structure.

The relaxation time scale of a simple two gate system at microscale is in the order of the relaxation of stimuli-responsive polymers. For larger architectures, faster relaxation is required. In general, a response can be accelerated by reducing environ-

mental drag (for instance, using air in place of liquid environment), and by increasing the energy density of the actuating polymers.

The 3D structures presented are relatively complex to fabricate at small length scales. However, the mechanical transistor works in 2D. It may be possible to embed and connect these transistors in a 2D sheet/membrane, allowing the sheet to compute and morph.

As a proof-of-concept, the work shows manipulation of a skeleton chain using a mechanical computer architecture that is actuated using muscle-like inputs. The architecture itself occupies a large space of the system. In practice, context-dependent designs optimization will be required to pack this architecture. One of the future works that are important to this end is the realization of signal storage and amplification. This will allow the signal to travel longer distances and then being amplified as required. Thinking about spatially integrating and compacting the system should also be useful for such optimization.

While project-specific future goals can be found in the respective chapters and the above mentions, some overall future directions are the following. Identifying context and specific problem statements is very important to establish the objectives and the constraints for these systems in the practical setting. For colloidal swarm systems, it will be interesting to investigate the agent policy given the colloidal abilities, agent being a single colloid or a connected bunch. Further, experimental techniques are to be developed to fabricate those policies into the colloidal agents. The greatest challenge for morphological systems is the fabrication of their exact structure. Whether it is the chain loops of active particles or mechanical logic gates, robust and precise synthesis of these structures at the colloidal scale is still a challenge. Further

developments in DNA fabrication, 3D printing, and lithography techniques will allow

scalable and economical manufacturing of these structures.

BIBLIOGRAPHY

[1] Bradley J. Nelson, Ioannis K. Kaliakatsos, and Jake J. Abbott. Microrobots for Minimally Invasive Medicine. *Annual Review of Biomedical Engineering*, 12(1):55–85, jul 2010.

[2] Erol Şahin. Swarm Robotics: From Sources of Inspiration to Domains of Application. In *Swarm Robotics*, pages 10–20. Springer, Berlin, Heidelberg, 2005.

[3] Eric Diller and Metin Sitti. Micro-Scale Mobile Robotics. *Foundations and Trends in Robotics*, 2(3):143–259, 2011.

[4] S.C. Goldstein, J.D. Campbell, and T.C. Mowry. Programmable matter. *Computer*, 38(6):99–101, may 2005.

[5] Maria Guix, Carmen C. Mayorga-Martinez, and Arben Merkoçi. Nano/Micromotors in (Bio)chemical Science Applications. *Chemical Reviews*, 114(12):6285–6322, jun 2014.

[6] Clemens Bechinger, Roberto Di Leonardo, Hartmut Löwen, Charles Reichhardt, Giorgio Volpe, and Giovanni Volpe. Active Particles in Complex and Crowded Environments. *Reviews of Modern Physics*, 88(4):045006, nov 2016.

[7] M. C. Marchetti, J. F. Joanny, S. Ramaswamy, T. B. Liverpool, J. Prost, Madan Rao, and R. Aditi Simha. Hydrodynamics of soft active matter. *Reviews of Modern Physics*, 85(3):1143–1189, jul 2013.

[8] Syeda Sabrina, Mykola Tasinkevych, Suzanne Ahmed, Allan M. Brooks, Monica Olvera de la Cruz, Thomas E. Mallouk, and Kyle J. M. Bishop. Shape-Directed Microspinners Powered by Ultrasound. *ACS Nano*, 12(3):2939–2947, mar 2018.

[9] Alexander M. Maier, Cornelius Weig, Peter Oswald, Erwin Frey, Peer Fischer, and Tim Liedl. Magnetic Propulsion of Microswimmers with DNA-Based Flagellar Bundles. *Nano Letters*, 16(2):906–910, feb 2016.

[10] Debora Walker, Benjamin T. Käsdorf, Hyeon-Ho Jeong, Oliver Lieleg, and Peer Fischer. Enzymatically active biomimetic micropropellers for the penetration of mucin gels. *Science Advances*, 1(11):e1500501, dec 2015.

[11] Stefano Palagi and Peer Fischer. Bioinspired microrobots. *Nature Reviews Materials*, 3(6):113–124, jun 2018.

[12] Jeremie Palacci, Stefano Sacanna, Asher Preska Steinberg, David J Pine, and Paul M Chaikin. Living crystals of light-activated colloidal surfers. *Science (New York, N.Y.)*, 339(6122):936–40, 2013.

[13] Ben L. Feringa. The Art of Building Small: From Molecular Switches to Motors (Nobel Lecture). *Angewandte Chemie International Edition*, 56(37):11060–11078, sep 2017.

[14] Bernard Yurke, Andrew J. Turberfield, Allen P. Mills, Friedrich C. Simmel, and Jennifer L. Neumann. A DNA-fuelled molecular machine made of DNA. *Nature*, 406(6796):605–608, aug 2000.

[15] Tingting Yu, Prabha Chuphal, Snigdha Thakur, Shang Yik Reigh, Dhruv P. Singh, and Peer Fischer. Chemical micromotors self-assemble and self-propel by spontaneous symmetry breaking. *Chemical Communications*, 54(84):11933–11936, oct 2018.

[16] Mayank Agrawal, Isaac R. Bruss, and Sharon C. Glotzer. Tunable emergent structures and traveling waves in mixtures of passive and contact-triggered-active particles. *Soft Matter*, 13(37):6332–6339, sep 2017.

[17] Arijit Ghosh, ChangKyu Yoon, Federico Ongaro, Stefano Scheggi, Florin M. Selaru, Sarthak Misra, and David H. Gracias. Stimuli-Responsive Soft Untethered Grippers for Drug Delivery and Robotic Surgery. *Frontiers in Mechanical Engineering*, 3:7, jul 2017.

[18] Xuan Zhang and Siowling Soh. Performing Logical Operations with Stimuli-Responsive Building Blocks. *Advanced Materials*, 29(18):1606483, may 2017.

[19] Yiqi Mao, Zhen Ding, Chao Yuan, Shigang Ai, Michael Isakov, Jiangtao Wu, Tiejun Wang, Martin L. Dunn, and H. Jerry Qi. 3D Printed Reversible Shape Changing Components with Stimuli Responsive Materials. *Scientific Reports*, 6(1):24761, apr 2016.

[20] Yajuan Sun, Linfeng Chen, Yan Jiang, Xuan Zhang, Xiukai Yao, and Siowling Soh. Soft stimuli-responsive grippers and machines with high load-to-weight ratios. *Materials Horizons*, 6(1):160–168, jan 2019.

[21] Marek Grzelczak, Jan Vermant, Eric M Furst, and Luis M Liz-Marzá. Directed Self-Assembly of Nanoparticles. 4, 2010.

[22] W. Benjamin Rogers, William M. Shih, and Vinothan N. Manoharan. Using DNA to program the self-assembly of colloidal nanoparticles and microparticles. *Nature Reviews Materials*, 1(3):16008, mar 2016.

[23] Shawn M. Douglas, Hendrik Dietz, Tim Liedl, Björn Högberg, Franziska Graf, and William M. Shih. Self-assembly of DNA into nanoscale three-dimensional shapes. *Nature*, 459(7245):414–418, may 2009.

[24] Yuanping Song, Robert M. Panas, Samira Chizari, Lucas A. Shaw, Julie A. Jackson, Jonathan B. Hopkins, and Andrew J. Pascall. Additively manufacturable micro-mechanical logic gates. *Nature Communications*, 10(1):882, dec 2019.

[25] Matteo Verotti, Rocco Crescenzi, Marco Balucani, and Nicola P. Belfiore. MEMS-Based Conjugate Surfaces Flexure Hinge. *Journal of Mechanical Design*, 137(1):012301, jan 2015.

[26] Volodymyr B. Koman, Pingwei Liu, Daichi Kozawa, Albert Tianxiang Liu, Anton L. Cottrill, Youngwoo Son, Jose A. Lebron, and Michael S. Strano. Colloidal nanoelectronic state machines based on 2D materials for aerosolizable electronics. *Nature Nanotechnology*, 13(9):819–827, sep 2018.

[27] Sharon C. Glotzer and Michael J. Solomon. Anisotropy of building blocks and their assembly into complex structures. *Nature Materials*, 6(8):557–562, aug 2007.

[28] Changhai Ru, Jun Luo, Shaorong Xie, and Yu Sun. A review of non-contact micro- and nano-printing technologies, 2014.

[29] Michael Rubenstein, Alejandro Cornejo, and Radhika Nagpal. Robotics. Programmable self-assembly in a thousand-robot swarm. *Science (New York, N.Y.)*, 345(6198):795–9, aug 2014.

[30] J. William Boley, Wim M. van Rees, Charles Lissandrello, Mark N. Horenstein, Ryan L. Truby, Arda Kotikian, Jennifer A. Lewis, and L. Mahadevan. Shape-shifting structured lattices via multimaterial 4D printing. *Proceedings of the National Academy of Sciences*, 2019.

[31] Wenjing Wang, Craig P. Wildes, Tanyaporn Pattarabanjird, Mateo I. Sanchez, Gordon F. Glober, Gillian A. Matthews, Kay M. Tye, and Alice Y. Ting. A light- A nd calcium-gated transcription factor for imaging and manipulating activated neurons. *Nature Biotechnology*, 2017.

[32] Scott Camazine, Jean-Louis Deneubourg, Nigel R Franks, James Sneyd, Guy Theraulaz, and Eric Bonabeau. *Self-Organization in Biological Systems*. 2001.

[33] Michael Rubenstein, Christian Ahler, and Radhika Nagpal. Kilobot: A low cost scalable robot system for collective behaviors. In *2012 IEEE International Conference on Robotics and Automation*, pages 3293–3298. IEEE, may 2012.

[34] Shiyong Sun, Mei Li, Faqin Dong, Shengjie Wang, Liangfei Tian, and Stephen Mann. Chemical Signaling and Functional Activation in Colloidosome-Based Protocells. *Small*, 2016.

[35] Serge Kernbach. *Handbook of collective robotics - fundamentals and challenges*. 2013.

[36] Eric Theveneau, Benjamin Steventon, Elena Scarpa, Simon Garcia, Xavier Trepat, Andrea Streit, and Roberto Mayor. Chase-and-run between adjacent cell populations promotes directional collective migration. *Nature Cell Biology*, 15(7):763–772, 2013.

[37] N J Cira, A Benusiglio, and M Prakash. Vapour-mediated sensing and motility in two-component droplets. *Nature*, 519(7544):446–450, 2015.

[38] Laura D. Colon-Melendez. *Anisotropic Colloidal Assembly: Kinetics, Shape Complementarity, and Field-mediated Propulsion.* PhD thesis, University of Michigan, 2016.

[39] Fuduo Ma, Xingfu Yang, Hui Zhao, and Ning Wu. Inducing Propulsion of Colloidal Dimers by Breaking the Symmetry in Electrohydrodynamic Flow. *Physical Review Letters*, 115(20):208302, 2015.

[40] Shuguang Li, Richa Batra, David Brown, Hyun-Dong Chang, Nikhil Ranganathan, Chuck Hoberman, Daniela Rus, and Hod Lipson. Particle robotics based on statistical mechanics of loosely coupled components. *Nature*, 567(7748):361–365, mar 2019.

[41] Johann Elbaz, Oleg Lioubashevski, Fuan Wang, Françoise Remacle, Raphael D. Levine, and Itamar Willner. DNA computing circuits using libraries of DNAzyme subunits. *Nature Nanotechnology*, 5(6):417–422, jun 2010.

[42] Francis G. Woodhouse and Jörn Dunkel. Active matter logic for autonomous microfluidics. *Nature Communications*, 8(1):15169, apr 2017.

[43] Tamás Vicsek, András Czirók, Eshel Ben-Jacob, Inon Cohen, and Ofer Shochet. Novel Type of Phase Transition in a System of Self-Driven Particles. *Physical Review Letters*, 75(6):1226–1229, aug 1995.

[44] Yaouen Fily and M. Cristina Marchetti. Athermal Phase Separation of Self-Propelled Particles with No Alignment. *Physical Review Letters*, 108(23):235702, jun 2012.

[45] Sriram Ramaswamy. The mechanics and statistics of active matter. *Annual Review of Condensed Matter Physics*, 1(1):323–345, 2010.

[46] M. A. McEvoy and N. Correll. Materials that couple sensing, actuation, computation, and communication. *Science*, 347(6228):1261689–1261689, 2015.

[47] O. Berk Usta, Alexander Alexeev, Guangdong Zhu, and Anna C. Balazs. Modeling microcapsules that communicate through nanoparticles to undergo self-propelled motion. *ACS Nano*, 2(3):471–476, 2008.

[48] Gabriel S. Redner, Michael F. Hagan, and Aparna Baskaran. Structure and dynamics of a phase-separating active colloidal fluid. *Physical Review Letters*, 110(5):055701, 2013.

[49] Michael E. Cates and Julien Tailleur. Motility-Induced Phase Separation. *Annual Review of Condensed Matter Physics*, 6(1):219–244, 2015.

[50] Joakim Stenhammar, Raphael Wittkowski, Davide Marenduzzo, and Michael E. Cates. Activity-induced phase separation and self-assembly in mixtures of active and passive particles. *Physical Review Letters*, 114(1):018301, 2015.

[51] Nguyen H.P. Nguyen, Daphne Klotsa, Michael Engel, and Sharon C. Glotzer. Emergent Collective Phenomena in a Mixture of Hard Shapes through Active Rotation. *Physical Review Letters*, 112(7):075701, feb 2014.

[52] Matthew Spellings, Michael Engel, Daphne Klotsa, Syeda Sabrina, Aaron M Drews, Nguyen H P Nguyen, Kyle J M Bishop, and Sharon C Glotzer. Shape control and compartmentalization in active colloidal cells. *Proceedings of the National Academy of Sciences of the United States of America*, 112(34):E4642–50, aug 2015.

[53] Michael Engel, Joshua A. Anderson, Sharon C. Glotzer, Masaharu Isobe, Etienne P. Bernard, and Werner Krauth. Hard-disk equation of state: First-order liquid-hexatic transition in two dimensions with three simulation methods. *Physical Review E*, 87(4):042134, apr 2013.

[54] Peter J. Lu () and David A Weitz. Colloidal Particles: Crystals, Glasses, and Gels. *Annual Review of Condensed Matter Physics*, 4(1):217–233, 2013.

[55] Gabriel S. Redner, Aparna Baskaran, and Michael F. Hagan. Reentrant phase behavior in active colloids with attraction. *Physical Review E*, 88(1):012305, 2013.

[56] Adam Wysocki, Roland G. Winkler, and Gerhard Gompper. Traveling fronts in active-passive particle mixtures. *arXiv preprint arXiv:1601.00850*, page 2016, jan.

[57] John J. Tyson and James P. Keener. Singular perturbation theory of traveling waves in excitable media (a review). *Physica D: Nonlinear Phenomena*, 32(3):327–361, 1988.

[58] Walter F. Paxton, Kevin C. Kistler, Christine C. Olmeda, Ayusman Sen, Sarah K. St. Angelo, Yanyan Cao, Thomas E. Mallouk, Paul E. Lammert, and Vincent H. Crespi. Catalytic nanomotors: Autonomous movement of striped nanorods. *Journal of the American Chemical Society*, 126(41):13424–13431, 2004.

[59] HOOMD-blue. HOOMD-blue.

[60] Joshua A. Anderson, Chris D. Lorenz, and A. Travesset. General purpose molecular dynamics simulations fully implemented on graphics processing units. *Journal of Computational Physics*, 227(10):5342–5359, 2008.

[61] Jens Glaser, Trung Dac Nguyen, Joshua A. Anderson, Pak Lui, Filippo Spiga, Jaime A. Millan, David C. Morse, and Sharon C. Glotzer. Strong scaling of general-purpose molecular dynamics simulations on GPUs. *Computer Physics Communications*, 192:97–107, 2015.

[62] M. P. Allen and D. J. Tildesley. *Computer Simulation of Liquids*. Oxford University Press, 1989.

[63] D Chandler, J D Weeks, and H C Andersen. Van der waals picture of liquids, solids, and phase transformations. *Science (New York, N.Y.)*, 220(4599):787–94, 1983.

[64] Joakim Stenhammar, Davide Marenduzzo, Rosalind J Allen, and Michael E Cates. Phase behaviour of active Brownian particles: the role of dimensionality. *Soft matter*, 10(10):1489–99, 2014.

[65] Guang-Zhong Yang, Jim Bellingham, Pierre E. Dupont, Peer Fischer, Luciano Floridi, Robert Full, Neil Jacobstein, Vijay Kumar, Marcia McNutt, Robert Merrifield, Bradley J. Nelson, Brian Scassellati, Mariarosaria Taddeo, Russell Taylor, Manuela Veloso, Zhong Lin Wang, and Robert Wood. The grand challenges of <i>Science Robotics</i>. *Science Robotics*, 3(14):eaar7650, jan 2018.

[66] I. Slavkov, D. Carrillo-Zapata, N. Carranza, X. Diego, F. Jansson, J. Kaandorp, S. Hauert, and J. Sharpe. Morphogenesis in robot swarms. *Science Robotics*, 3(25):eaau9178, dec 2018.

[67] Gretchen A Devries, Markus Brunnbauer, Ying Hu, Alicia M Jackson, Brenda Long, Brian T Neltner, Oktay Uzun, Benjamin H Wunsch, and Francesco Stellacci. Divalent metal nanoparticles. *Science (New York, N.Y.)*, 315(5810):358–61, jan 2007.

[68] Dmytro Nykypanchuk, Mathew M. Maye, Daniel van der Lelie, and Oleg Gang. DNA-guided crystallization of colloidal nanoparticles. *Nature*, 451(7178):549–552, jan 2008.

[69] Chuan Zhang, Robert J. Macfarlane, Kaylie L. Young, Chung Hang J. Choi, Liangliang Hao, Evelyn Auyeung, Guoliang Liu, Xiaozhu Zhou, and Chad A. Mirkin. A general approach to DNA-programmable atom equivalents. *Nature Materials*, 12(8):741–746, aug 2013.

[70] Robert Morgan. Linearization and Stability Analysis of Nonlinear Problems. *Rose-Hulman Undergraduate Mathematics Journal*, 16(2), jan 2017.

[71] Trung Dac Nguyen, Carolyn L. Phillips, Joshua A. Anderson, and Sharon C. Glotzer. Rigid body constraints realized in massively-parallel molecular dynamics on graphics processing units. *Computer Physics Communications*, 182(11):2307–2313, nov 2011.

[72] Carolyn L. Phillips, Joshua A. Anderson, and Sharon C. Glotzer. Pseudo-random number generation for Brownian Dynamics and Dissipative Particle Dynamics simulations on GPU devices. *Journal of Computational Physics*, 230(19):7191–7201, aug 2011.

[73] R. Featherstone and D. Orin. Robot dynamics: equations and algorithms. In *Proceedings 2000 ICRA. Millennium Conference. IEEE International Conference on Robotics and Automation. Symposia Proceedings (Cat. No.00CH37065)*, volume 1, pages 826–834. IEEE.

[74] S. Pellegrino. Structural computations with the singular value decomposition of the equilibrium matrix. *International Journal of Solids and Structures*, 30(21):3025–3035, jan 1993.

[75] Ralph C. Merkle, Robert A. Freitas, Tad Hogg, Thomas E. Moore, Matthew S. Moses, and James Ryley. Mechanical Computing Systems Using Only Links and Rotary Joints. *Journal of Mechanisms and Robotics*, 10(6):061006, sep 2018.

[76] Jordan R Raney, Neel Nadkarni, Chiara Daraio, Dennis M Kochmann, Jennifer A Lewis, and Katia Bertoldi. Stable propagation of mechanical signals in soft media using stored elastic energy. *Proceedings of the National Academy of Sciences of the United States of America*, 113(35):9722–7, aug 2016.

[77] Elizabeth Elacqua, Xiaolong Zheng, Cicely Shillingford, Mingzhu Liu, and Marcus Weck. Molecular Recognition in the Colloidal World. *Accounts of Chemical Research*, 50(11):2756–2766, nov 2017.

[78] Timothy J. Merkel, Kevin P. Herlihy, Janine Nunes, Ryan M. Orgel, Jason P. Rolland, and Joseph M. Desimone. Scalable, shape-specific, top-down fabrication methods for the synthesis of engineered colloidal particles. *Langmuir*, 2010.

[79] Liang Hu, Qiang Zhang, Xue Li, and Michael J. Serpe. Stimuli-responsive polymers for sensing and actuation. *Materials Horizons*, 2019.

[80] Thorsten Hugel, Nolan B. Holland, Anna Cattani, Luis Moroder, Markus Seitz, and Hermann E. Gaub. Single-molecule optomechanical cycle. *Science*, 2002.

[81] Martien A.Cohen Stuart, Wilhelm T.S. Huck, Jan Genzer, Marcus Müller, Christopher Ober, Manfred Stamm, Gleb B. Sukhorukov, Igal Szleifer, Vladimir V. Tsukruk, Marek Urban, Françoise Winnik, Stefan Zauscher, Igor Luzinov, and Sergiy Minko. Emerging applications of stimuli-responsive polymer materials, 2010.

[82] Alexander E. Marras, Lifeng Zhou, Hai Jun Su, and Carlos E. Castro. Programmable motion of DNA origami mechanisms. *Proceedings of the National Academy of Sciences of the United States of America*, 2015.

[83] W Benjamin Rogers and John C Crocker. Direct measurements of DNA-mediated colloidal interactions and their quantitative modeling. *Proceedings of the National Academy of Sciences of the United States of America*, 108(38):15687–92, sep 2011.

[84] Mohammad Vaezi, Hermann Seitz, and Shoufeng Yang. A review on 3D micro-additive manufacturing technologies, 2013.

[85] Sangbae Kim, Elliot Hawkes, Kyujin Cho, Matthew Jolda, Joe Foley, and Robert Wood. Micro artificial muscle fiber using NiTi spring for soft robotics. In *2009 IEEE/RSJ International Conference on Intelligent Robots and Systems, IROS 2009*, 2009.

[86] K. S.J. Pister, M. W. Judy, S. R. Burgett, and R. S. Fearing. Microfabricated hinges. *Sensors and Actuators: A. Physical*, 1992.

[87] Manu Prakash and Neil Gershenfeld. Microfluidic bubble logic. *Science (New York, N.Y.)*, 315(5813):832–5, feb 2007.

[88] Rahim Mutlu, Gursel Alici, Marc in het Panhuis, and Geoffrey M. Spinks. 3D Printed Flexure Hinges for Soft Monolithic Prosthetic Fingers. *Soft Robotics*, 3(3):120–133, sep 2016.